GOLD NANOCAGES AND RELATED NANOSTRUCTURES FOR PLASMONIC AND BIOMEDICAL APPLICATIONS

A Dissertation
Presented to
The Academic Faculty

by

Miaoxin Yang

In Partial Fulfillment
of the Requirements for the Degree
of Doctor of Philosophy in the
School of Chemistry and Biochemistry

Georgia Institute of Technology
August, 2017

GOLD NANOCAGES AND RELATED NANOSTRUCTURES FOR PLASMONIC AND BIOMEDICAL APPLICATIONS

Approved by:

Dr. Younan Xia, Advisor
Department of Biomedical Engineering
Georgia Institute of Technology

Dr. Ronghu Wu
School of Chemistry and Biochemistry
Georgia Institute of Technology

Dr. Z. John Zhang
School of Chemistry and Biochemistry
Georgia Institute of Technology

Dr. Mostafa A. El-Sayed
School of Chemistry and Biochemistry
Georgia Institute of Technology

Dr. Zhiqun Lin
School of Materials Science and Engineering
Georgia Institute of Technology

Date Approved: May 3, 2017

Dedicated to my parents, for their love, endless support, and encouragement.

ACKNOWLEDGEMENTS

First of all, I would like express my deepest gratitude and appreciation to my advisor, Professor Younan Xia, for his many years of guidance and support. His knowledge and enthusiasm on science is truly inspirational, which helps me accomplish my research. I have certainly learned a lot from this experience. I would like to express my appreciation to Prof. Dong Qin, for her advice and support, not only on research, but on life as well. I also would like to extend my gratitude to Professors Mostafa El-Sayed, John Zhang, Ronghu Wu, and Zhiqun Lin for serving on my dissertation committee. Thank you for all of your support and advice.

I greatly appreciate Professor Jingyi Chen and Dr. Claire Cobley, who generously shared their time and experience when I was new to the group. I would like to thank Professor Yongjian Liu at Washington University in St. Louis, for his help in radiolabeling and PET imaging. I would like to make a special thanks to Dr. Kyle D. Gilroy and Zachary Hood, who helped me with DDA simulations and performed HRTEM imaging for some of my projects. I am thankful for the support provided by many people at Georgia Tech: Dr. Xiaohu, Xia, Dr. Wenying Liu, Dr. Yiqun Zheng, Dr. Jinho Park, Dr. Bo Pang, Dr. Xuan Yang, Dr. Lei Zhang, Dr. Guangda Niu, Dr. Hsin-Chieh Peng, Dr. Chunlei Zhu, Dr. Da Huo, Shan Zhou, Zachary Hood, Aleksey Ruditskiy, Madeline Vara, Legna Figueroa-Cosme, and many other current and former members of the Xia group, who have helped me tremendously during my dissertation study.

My sincerest thanks to my parents, Shijun Yang and Guilan Wang for their endless love and support. At last, I would like to thank me wife, Yuan He, and my son, Jerry, for their support throughout these years.

TABLE OF CONTENTS

Page

ACKNOWLEDGEMENTS iv

LIST OF TABLES viii

LIST OF FIGURES ix

LIST OF SYMBOLS AND ABBREVIATIONS xiv

SUMMARY xvii

CHAPTER

1 Introduction 1

1.1 Overview of Gold Nanomaterials 1

1.2 Gold Nanocages and Related Nanostructures 6

1.3 Scope of This Work 10

1.4 Notes to Chapter 1 12

1.5 References 12

2 Radioactive Gold Nanocages for Positron Emission Tomography 17

2.1 Introduction 17

2.2 Results and Discussion 19

2.3 Conclusion 30

2.4 Experimental Section 31

2.5 Notes to Chapter 2 34

2.6 References 34

3 Controlling the Deposition of Palladium on Gold Nanocages: Outer Surface Only *Versus* Both Outer and Inner Surfaces 38

3.1 Introduction 38

3.2 Results and Discussion 40

3.3 Conclusion 53

3.4 Experimental Section 53

3.5 Notes to Chapter 3 56

3.6 References 56

4 Synthesis of Bi- and Tri-metallic Nanorattles with Compact Sizes 59

4.1 Introduction 59

4.2 Results and Discussion 60

4.3 Conclusion 78

4.4 Experimental Section 78

4.5 Notes to Chapter 4 84

4.6 References 84

5 Coating Silver Nanowires with Ultrathin Sheaths of Gold to Improve Their Stability against Oxidation 86

5.1 Introduction 86

5.2 Results and Discussion 87

5.3 Conclusion 101

5.4 Experimental Section 101

5.5 Notes to Chapter 5 103

5.6 References 104

6 Conclusions and Future Directions 106

6.1 Conclusions 106

6.2 Future Directions 108

6.3 References 110

LIST OF TABLES

Page

Table 5.1 Gold contents in Ag@Au core-sheath nanowires prepared by adding different volumes of $Au(OH)_4^-$ solution calculated from ICP-MS data. 92

LIST OF FIGURES

Page

Figure 1.1 Illustration showing the collective oscillation of free electrons in a Au nanosphere and the LSPR spectra calculated for a 50-nm Au nanosphere. 2

Figure 1.2 Illustration showing a self-assembled monolayer of alkanethiolate formed on the surface of a Au substrate. 5

Figure 1.3 Illustration showing morphological changes involved in the galvanic replacement reaction between aqueous $HAuCl_4$ and a Ag nanocube. 7

Figure 1.4 Electron micrographs of Au nanocages with different sizes and shapes. 9

Figure 2.1 Illustration showing the synthesis of Cu-doped Au nanocages through co-deposition of Au and Cu atoms onto Au nanocages. 19

Figure 2.2 TEM images of pristine and Cu-doped Au nanocages with different shell thicknesses. 21

Figure 2.3 UV-vis spectra of pristine and Cu-doped Au nanocages with different shell thicknesses. 24

Figure 2.4 Extinction spectra calculated using the DDA method for pristine and Cu-doped Au nanocages with different shell thicknesses. 26

Figure 2.5 Correlation between the radioactivity of the $^{64}CuCl_2$ precursor used in a synthesis and the resultant ^{64}Cu-doped Au nanocages. 27

Figure 2.6 Transverse PET/CT images of the PEGylated ^{64}Cu-doped Au nanocages in mouse4T1 and PDX tumor models at 24 h post injection and their corresponding quantification of tumor uptake. 29

Figure 2.7 In vivo distribution profiles of the PEGylated ^{64}Cu-doped Au nanocages in both 4T1 and PDX tumor models at 24 h post injection. 30

Figure 3.1 Illustration showing two different scenarios for the deposition of Pd on the surfaces of Au nanocages with openings at the corners. 41

Figure 3.2 Schematic illustration showing the calculation method for the thicknesses of Pd shells on the outer and inner surface of a Au nanocage. 42

Figure 3.3 TEM images of Pd@Au double-shell nanocages prepared by titrating aqueous Na_2PdCl_4 with various volumes and a comparison of the thickness of Pd shells on the inner and outer surfaces of the Au nanocages. 44

Figure 3.4 TEM images of Pd@Au@Pd triple-shell nanocages prepared by titrating aqueous Na_2PdBr_4 with various volumes and a comparison of the thickness of Pd shells on the inner and outer surfaces of the Au nanocages. 46

Figure 3.5 HR-TEM and HAADF-STEM images of Au@Pd double-shell and Pd@Au@Pd triple-shell nanocages. 47

Figure 3.6 UV-vis spectra of Au@Pd double-shell and Pd@Au@Pd triple-shell nanocages. 49

Figure 3.7 TEM images of Au-Pd nanocages prepared by one-shot injecting Na_2PdBr_4, and Na_2PdCl_4 with different volumes and a comparison of the thicknesses of Pd layers deposited on the inner and outer surfaces of Au nanocages in the final products. 52

Figure 4.1 Schematic illustration showing the changes involved in the formation of M@Au/Ag nanorattles. 61

Figure 4.2 TEM images of the Au@Ag core-shell nanocubes and the corresponding double-shell nanocubes after the deposition of Au shells with different thicknesses. 63

Figure 4.3 TEM images of the Au@Ag nanocubes and the corresponding structures after the titration of different volumes of aqueous $HAuCl_4$ without introducing NaOH solution to maintain the alkaline pH value. 65

Figure 4.4 Plots of pH value as a function of the volume of aqueous $HAuCl_4$ added during the Au deposition and the galvanic replacement steps. 66

Figure 4.5 TEM images of the Au@Au/Ag nanorattles synthesized by reacting $Au@Ag@Au_{2L}$ with different volumes of $HAuCl_4$ solution. 68

Figure 4.6 UV-vis spectra of the double-shelled nanocubes and Au@Au/Ag nanorattles prepared by reaction with different volumes of $HAuCl_4$ solution. 69

Figure 4.7 Extinction spectra calculated for Au@Ag nanocubes, Au@Ag@Au double-shell nanocubes, and Au@Au/Ag nanorattles using the DDA method 71

Figure 4.8 TEM images of Au@Au/Ag nanorattles obtained from $Au@Ag@Au_{2–3L}$ and the corresponding UV-vis spectra recorded during the titration process. 72

Figure 4.9 The mole percent of Au in the resultant nanostructures when different volumes of aqueous $HAuCl_4$ were titrated into suspensions of Au@Ag@Au nanocubes. 73

Figure 4.10 TEM images of the Pd cuboctahedral seeds, Pd@Ag nanocubes, Pd@Au/Ag nanorattles; Pt spherical seeds, Pt@Ag nanocubes, and Pt@Au/Ag nanorattles. 75

Figure 4.11 Digital photo of MDA-MB-231 cell culture dish after incubation with the 15-nm Au@Au/Ag nanorattles, fluorescence images of calcein AM and red fluorescence dye co-stained cells after laser irradiation, and cell viability of the cells treated with nanorattles and 808 nm laser irradiation for 5 min with different power densities. 77

Figure 4.12 Truncation model used in the DDA simulation. 83

Figure 5.1 A schematic illustration showing the structural changes for Ag nanowires before and after their surfaces have been coated with Au. 88

Figure 5.2 TEM image of the pristine Ag nanowires before Au deposition. 89

Figure 5.3 TEM image, UV-vis absorbance, and transmittance spectra of Ag@Au core-sheath nanowires prepared by adding different volumes of Au precursor solution. 91

Figure 5.4 High-resolution TEM and HAADF-STEM images of a Ag@Au core-sheath nanowire, and corresponding EDS elemental mapping of Ag and Au. 94

Figure 5.5 TEM images of the Ag@Au core-sheath nanowires synthesized at room temperature before and after H_2O_2 etching. 95

Figure 5.6 UV-vis spectra of pristine Ag nanowires and Ag@Au core-sheath nanowires before and after the etching with gaseous O_2, 0.85 M aqueous H_2O_2 solution, and 1 mM aqueous $Fe(NO_3)_3$ solution, and corresponding TEM images of Ag@Au core-sheath nanowires after etching with H_2O_2 and $Fe(NO_3)_3$. 97

Figure 5.7 UV-vis spectra of the Ag@Au core-sheath nanowires before and after incubation with 100 mM NaCl and 5 μM NaHS for 2 h, and the corresponding TEM images of the Ag@Au core-sheath nanowires after the incubation. 100

LIST OF SYMBOLS AND ABBREVIATIONS

A	precursor concentration
AA	ascorbic acid
C_p	specific heat
CT	computed tomography
CTAB	hexadecyltrimethylammonium bromide
CTAC	cetyltrimethylammonium chloride
DDA	discrete dipole approximation
DFT	density functional theory
DI	deionized
DMEM	Dulbecco's modified Eagle's medium
E	energy output
EDX	energy dispersive X-ray
EG	ethylene glycol
EPR	enhanced permeability and retention
fcc	face-centered cubic
FT	Fourier transform

HAADF	high-angle annular dark-field
HRTEM	high-resolution transmission electron microscopy
ICP-MS	inductively-coupled plasma mass spectrometry
ITO	indium tin oxide
k	rate constant
LSPR	localized surface plasmon resonance
MTT	3-(4,5-dimethylthiazol-2-thiazolyl)-2,5-diphenyl-2H-tetrazolium bromide
MBE	2-methyl-3-buten-2-ol
NIR	near-infrared
OLED	organic light emitting diode
OPV	organic photovoltaics
P	power density
PDX	patient derived xenograft
PET	positron emission tomography
PVP	poly(vinyl pyrrolidone)
Q	heat

r_o	initial reduction rate
$R_{deposition}$	rate of atomic deposition
$R_{diffusion}$	rate of atomic surface diffusion
SERS	surface-enhanced Raman scattering
STEM	scanning transmission electron microscopy
t	time
TEM	transmission electron microscopy
TNBC	triple-negative breast cancer
UV-vis	ultraviolet-visible
V	volume
XRD	X-ray diffraction
η	energy conversion efficiency
ρ	density
ε	dielectric constant

SUMMARY

Gold nanocages and related nanostructures have shown great potential in applications ranging from catalysis to theranostics. To make full use of these nanomaterials, it is crucial for us to precisely control their size, shape, and structure, since their physiochemical properties are determined by these parameters. This dissertation is focused on the synthesis of Au nanocages and their derivatives for photonic and biomedical applications. I start with the synthesis of Cu-doped Au nanocages through the co-reduction of Au and Cu precursors in the presence of pre-synthesized Au nanocages, and then demonstrate their use as a PET tracer when ^{64}Cu is involved. With the insights gained from this study, I carry out a systematic study to examine the deposition of Pd on Au nanocages, and reveal the relationship between the reduction kinetics of metal precursors and the deposition behaviors. In the third project, I demonstrate the synthesis of compact Au nanorattles with edge length as small as 15 nm, through a two-step procedure that combines the deposition of Au on Ag nanocubes to enhance their physical robustness and a galvanic reaction to complete the synthesis. Finally, I demonstrate the synthesis of Ag@Au core-sheath nanowires through the deposition of Au on Ag nanowires in a galvanic-free manner, in an effort to improve their stability against various oxidants. The mechanistic understanding achieved in this dissertation paves the road for the rational design and controlled synthesis of colloidal noble-metal nanomaterials with desired sizes, shapes, compositions, and structures.

CHAPTER 1

INTRODUCTION

1.1 Overview of Gold Nanomaterials

Gold is a precious metal with a characteristic bright and beautiful hue known as the golden yellow color [1]. The abundance of Au in the Earth's crust is extremely low (only 5 parts per billion) [2], which makes it one of the most valuable metals in the world. Besides, Au is characterized by a notable, long-lasting metal luster, making it popular in jewelry industry. Metallic Au also exhibits excellent malleability, and it can be easily formed into different shapes, and even hammered into very thin sheets or stretched into the find threads.

When processed into sub-100 nm structures, Au shows a unique collection of new properties distinct from bulk Au. The first scientific report on the production of Au nanomaterials can be traced back to the ground breaking work by Michael Faraday on Au colloids [3]. In 1857, Faraday discovered that "fine particles" could be formed by treating aqueous $HAuCl_4$ with phosphorus dissolved in CS_2 in a two-phase system. The aqueous suspension of such "fine particles" displayed a beautiful, ruby red color, completely different from the golden yellow color intrinsic to bulk Au. However, there was no theory to explain why such "fine particles" would produce a ruby red color until 1908, when Gustav Mie, a German physicist, solved the Maxwell equations and established that the intense red color could be attributed to the absorption and scattering of light by the Au nanoparticles contained within the samples (Mie theory) [4]. When light impinges on a Au nanoparticle, the free electrons of the metal will immediately sense the electromagnetic field and begin to oscillate collectively relative to the lattice of positive ions at the same frequency as the incident light. Figure 1.1A shows a schematic illustration of this phenomenon for a Au nanosphere. This phenomenon is commonly known as localized

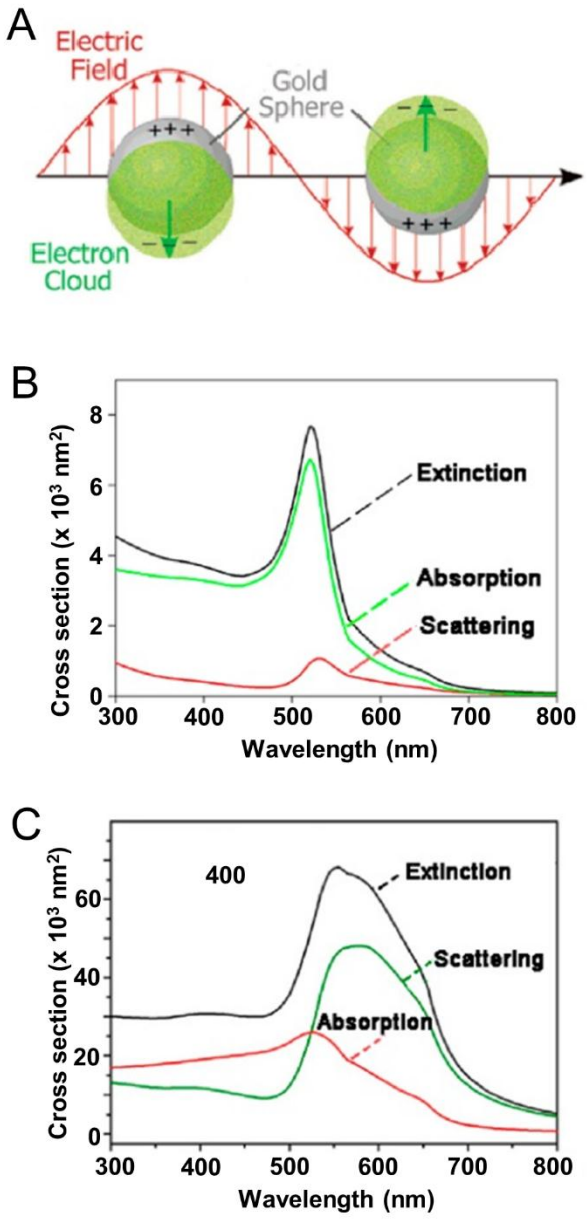

Figure 1.1. (A) Schematic illustration of the collective oscillation of free electrons in a Au nanosphere, which is responsible for the localized surface plasmon resonance (LSPR). (B) LSPR spectra calculated for a 50 nm Au nanosphere using Mie theory. (C) LSPR spectra calculated for a 100 nm Au nanosphere using Mie theory. Reprinted from [6]. Copyright 2005 Materials Research Society.

surface plasmon resonance (LSPR), which can occur in any nanomaterial with an adequately high density of free electrons, including those made of metals and heavily doped semiconductors [5–9]. In general, this process can be divided into two types of light-matter interactions: *scattering*, in which the incident light is re-radiated at the same frequency but into all direction, and *absorption*, in which the light is converted to heat (*i.e.*, phonons or vibrations of the crystal lattice). Together, these two processes lead to extinction (extinction = scattering + absorption) or attenuation in intensity for the incident light. In addition, strong electric fields are generated on the surface of the nanostructure, which can be used to greatly enhance the optical signals (*e.g.*, fluorescence or Raman scattering) arising from molecular species in the vicinity of the surface [10–14].

The LSPR properties (*e.g.*, the peak position and the ratio of scattering to absorption) of a Au nanostructure are determined by a number of parameters, including the size, shape, structure, and morphology, as well as the environment surrounding the surface of the nanostructure [5]. In general, the LSPR peak of a Au nanostructure will be shifted when the dielectric constant of the medium surrounding the nanostructure is altered, which can be employed for optical sensing. The LSPR peak position of Au nanostructures only shifts slightly when the size is changed. As shown in Figure 1.1B, Au nanospheres of 50 nm in diameter have an LSPR peak around 520 nm [6]. The strong absorption at this wavelength (green color) gives an immediate explanation for the ruby red color (complementary to the green color) displayed by Faraday's samples of Au colloids. However, the LSPR peak shifted only to 550 nm when the Au nanospheres were enlarged to 100 nm in diameter (Figure 1.1C). Gold nanostructures with LSPR peaks in the near-infrared region (NIR, 650–900 nm), are particularly interesting for biomedical applications. At these wavelengths, light can penetrate deeply into soft tissues because of the low absorption from blood and water as well as the weak scattering from soft tissues [15]. To this end, we must rely on other parameters than size in order to tune the LSPR peak of Au nanostructures to the NIR region: careful control of the shape or aspect ratio of nonspherical nanoparticles,

or fine-tuning of the shell thickness in hollow or core-shell nanostructures [7, 8]. In these cases, even small variations in terms of corner sharpness, aspect ratio, or shell thickness can lead to large shifts in the LSPR peak position. In addition, agglomeration of nanoparticles can lead to drastic red shifts for the LSPR peak position as the nanoparticles will interact with each other electromagnetically when they approach one another [16].

In addition to the aforementioned optical properties, Au also has a variety of inherent attributes that make its nanostructures attractive for various applications. First, Au is one of the least reactive known metals, and it has incredible resistance against both oxidation and corrosion. When exposed to air, not even a single atomic layer of gold oxide(s) can be detected on the surface of a Au substrate. This nonreactive and thus bio-inert nature of Au makes it an excellent candidate for biomedical applications both *in vitro* and *in vivo*. The low acute toxicity of Au nanomaterials has been documented by a number of *in vitro* studies, and preliminary reports have also shown favorable results for *in vivo* and clinical biocompatibility [5, 8].

Despite its extraordinary inertness under most conditions, Au is well-known for its ability to form a relatively strong (about 184 kJ/mol) gold–thiolate (Au-S) bond with compounds containing the thiol (–SH) or disulfide group (S–S) [17, 18]. This type of bond has been extensively researched in the setting of self-assembled monolayers (SAMs), wherein long-chain alkanethiols or alkyl disulfides can easily form a highly order molecular monolayer on the surface of a Au substrate (Figure 1.2) [19]. This well-characterized binding has been widely investigated to add functionality to the surface of Au nanostructures. By varying the functional group at the distal end of a thiol or disulfide molecule, one can easily generate robust, well-defined interfaces that are specifically designed to fulfill the requirements of different applications [20].

It is also worth noting that the content of Au in a sample can be easily quantified using a number of techniques such as inductively coupled plasma mass spectrometry (ICP-MS), inductively coupled plasma optical emission spectrometry (ICP-OES), and optical

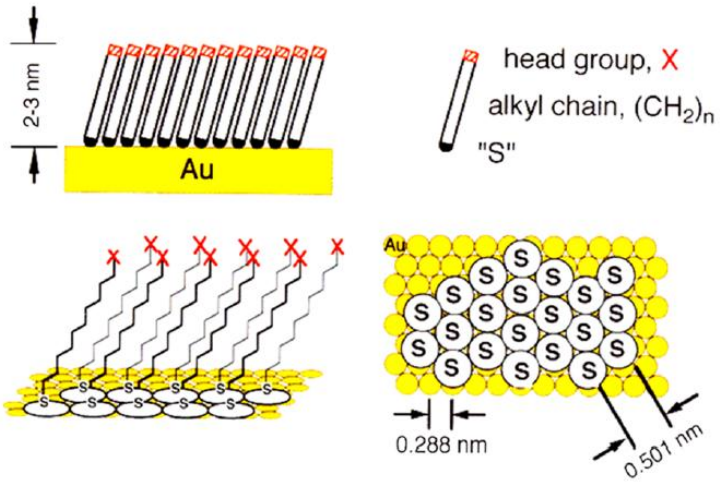

Figure 1.2. Schematic illustration of a self-assembled monolayer (SAM) of alkanethiolate formed on the surface of a Au substrate. The thickness of the organic monolayer is determined by the number of methylene groups (*n*) in the alkyl chain, which is approximately 2.5 nm for *n* =16. The alkyl chains extend from the surface on a nearly all-*trans* configuration and are tilted by roughly 30° from the normal to the surface to maximize the van der Waals interactions among the alkyl chains. Reprinted from [19]. Copyright 1990 American Chemical Society.

absorption spectroscopy. In particular, it should be noted that both $AuCl_4^-$ salt and Au nanostructures have characteristic absorption peaks in the UV-vis-NIR region, allowing their concentrations to be readily derived based on the Beer-Lambert law once calibration curves are made [21, 22].

Due to the unique, highly tunable optical properties of Au nanomaterials, they have been widely used in various biomedical applications. For example, Au nanomaterials can serve as optical probes for sensing as well as contrast agents for optical imaging [5, 8, 23–28]. Particularly, the absorption and scattering cross section of a Au nanostructure is

typically 5–6 orders of magnitude greater than that of an organic dye molecule, making it an ideal contrast agent for a number of newly developed imaging modalities [5, 8]. The LSPR peaks of Au nanostructures can be readily tuned to the NIR region to fulfill the requirement for *in vivo* applications while their sizes, shapes and surface properties can all be precisely engineered for optimal tumor targeting. Significantly, the photothermal conversion capability inherent to Au nanostructures can be utilized to trigger and manage the release of drugs and thus help achieve on-demand release with high spatial and temporal resolutions [29–31]. Even Au nanostructures themselves can be directly used for the ablation of tissues and killing of cancer cells owing to the photothermal effect [32–34]. With these properties combined together, Au nanomaterials can serve as a multifunctional platform for biomedicine and biological studies. In a sense, each tiny Au nanostructure can be engineered to carry all the functions sought for theranostics, together with intraoperative capability.

1.2 Gold Nanocages and Related Nanostructures

Gold nanocages represent a novel class of Au nanostructures invented by the Xia group in 2002 [35]. They are characterized by hollow interiors and/or porous walls, and thus exhibit tunable LSPR properties from the visible to the NIR region. Depending on the porosity of the walls, these nanostructures can be further classified into nanoboxes, nanocages, and nanoframes, with an increase in porosity [36–40].

Gold nanocages can be conveniently synthesized *via* a galvanic replacement reaction between a Au(III) or Au(I) precursor and Ag nanocrystals [36–40]. In this approach, each Ag nanocube serves as a sacrificial template, around which the resultant Au atoms are deposited to generate a nanobox. Figure 1.3 shows a schematic illustration of the major steps involved in the formation of these hollow/porous Au nanostructures [37, 41]. The shape and dimensions of the nanobox are determined by the template while the wall thick-

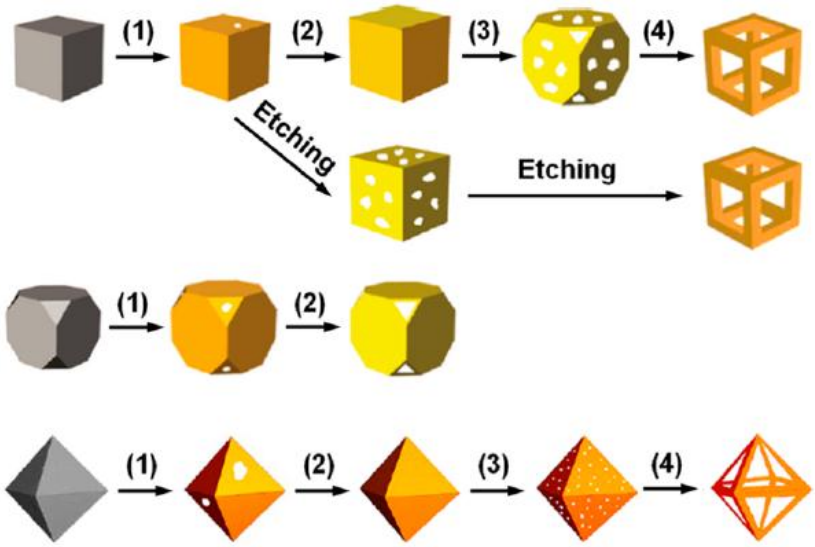

Figure 1.3. Schematic illustration of morphological changes involved in the galvanic replacement reaction between aqueous $HAuCl_4$ and a Ag nanocube with sharp corners (top trace), a nanocube with truncated corners (middle trace), and an octahedron (bottom trace). In all of these examples, step 1 corresponds to the initial deposition of Au on the surface of Ag nanostructures and the concurrent dissolution of Ag; step 2 corresponds to the additional deposition of Au and the alloying between Au and Ag; step 3 indicates the dealloying of the alloyed nanostructures, and step 4 shows the further dealloying of the alloyed nanostructures and the formation of Au nanoframes. The Au content keeps increasing as the galvanic replacement reaction proceeds. The pathway indicated by "etching" corresponds to the removal of Ag from the alloyed nanostructures using an aqueous etchant such as H_2O_2 or $Fe(NO_3)_3$, and the formation of a Au nanoframe. Reprinted from [57]. Copyright 2015 American Chemical Society.

ness can be easily and precisely tuned by varying the ratio between the Au(III) or Au(I) precursor and the Ag nanocrystals. By controlling the alloying and dealloying process involved, the walls of a nanobox can be further engineered to generate a nanocage and eventually a nanoframe [36–40, 42].

The idea of using a galvanic replacement reaction to generate hollow and/or porous metal nanostructures was first conceived and demonstrated by our group in 2002, with the involvement of multiple-twinned Ag nanoparticles as the sacrificial templates [35]. Later, most syntheses were focused on the use of Ag nanocubes as the templates owing to their well-defined shapes and facets, as well as their broad range of controllable sizes [36, 37, 43]. At the current stage of development, high quality Au nanoboxes and nanocages with edge lengths in the range of 20–200 nm can be routinely produced in relatively large quantities [44–48]. Figure 1.4 shows TEM images of some representative examples of Au nanocages. In a typical process, aqueous $HAuCl_4$ was titrated dropwise into an aqueous suspension of Ag nanocubes held at 90 °C. Upon contact of the two solutions, the galvanic replacement reaction will immediately take place between $HAuCl_4$ and Ag nanocubes according to the following equation [38]:

$$3\mathrm{Ag}_{(s)} + {AuCl_4^-}_{(aq)} \rightarrow Au_{(s)} + 3{Ag^+}_{(aq)} + 4{Cl^-}_{(aq)} \quad (1)$$

Driven by the difference in electrochemical potential between $AuCl_4^-$/Au (1.00 V) and Ag^+/Ag (0.80 V), Ag atoms are continuously oxidized and dissolved from the nanocubes, emptying the interior of the template. Simultaneously, Au(III) ions are reduced to generate Au(0) atoms, which are epitaxially deposited on the surface of each Ag template. The LSPR peak position of the resultant Au nanostructures can be tuned continuously from the visible into the NIR region by controlling the thickness and porosity of the walls, in addition to particle size. The tuning can be precisely achieved by simply controlling the amount of $HAuCl_4$ titrated into the suspension of Ag nanocubes. At the

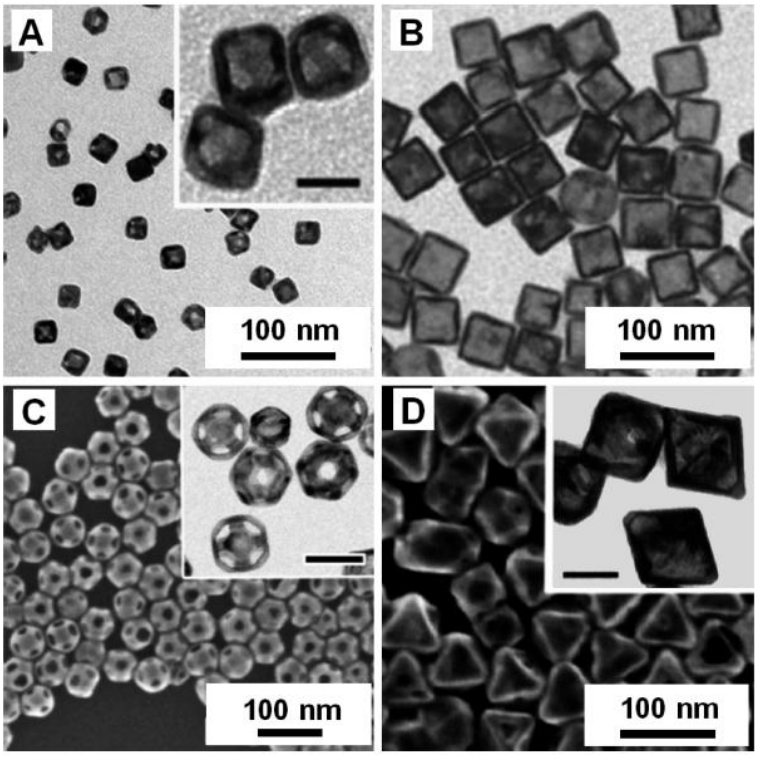

Figure 1.4. Electron micrographs of Au nanocages with different sizes and shapes. (A, B) TEM images of cubic Au nanocages with edge lengths of 25 and 55 nm, respectively. (C) TEM image of truncated cubic Au nanocages with an edge length of 30 nm, together with well-defined pores at the corner sites. (D) SEM and TEM (inset) images of octahedral Au nanocages with an edge length of 65 nm. The size and shape of Au nanocages are determined by the Ag templates used for the galvanic replacement reaction. The insets are the corresponding high-magnification TEM images, with the scale bars equal to 20 nm for (A) and 50 nm for (C) and (D), respectively. Reprinted from [57]. Copyright 2015 American Chemical Society.

moment, the most effective method for producing Ag nanocubes is still based on the polyol method [36, 44, 47]. Most recently, Ag nanocubes with edge lengths as short as 13 nm have also been achieved by modifying the original polyol method based upon ethylene glycol [49].

The synthetic process could be easily monitored using UV-vis-NIR spectroscopy, because of the red shift in LSPR peak for the nanostructures caused by the transformation in morphology. For the Au nanoboxes and nanocages derived from Ag nanocubes, their LSPR peak positions can be easily and precisely tuned from 400 nm all the way to 1200 nm. When an aqueous etchant, such as $Fe(NO_3)_3$ or NH_4OH, is used to selectively remove Ag from the alloyed walls, the nanocages could be transformed to nanoframes with tunable optical properties similar to those of Au nanorods [42]. Recently, researchers at Georgia Tech have developed a new two-step synthetic approach for Au nanocages, which involves: *i*) conformal deposition of thin layer of Au (3~6 atomic layers) onto pre-synthesized Ag nanocubes, and *ii*) selectively removal of Ag-based templates with aqueous H_2O_2 [50]. Compared to the conventional galvanic replacement approach, this method can produce Au nanocages with a precisely-controlled wall thickness, together with well-defined pores at corner sites. Significantly, Au nanocages with walls less than 2 nm were successfully prepared, with a characteristic LSPR peak positioned at *ca.* 1060 nm.

The unique structure and physicochemical properties of Au nanocages make them useful in a wide variety of applications including photothermal tumor destruction [34, 51], drug delivery [31, 52], multi-photon luminescence imaging [26], and photoacoustic imaging [53, 54]. Through a facile radio-labeling, Au nanocages can also be employed as radio-tracers for positron emission tomography and Cerenkov luminescence imaging [34, 55, 56].

1.3 Scope of This Work

The aim of this work is to develop synthetic approaches to Au nanocages and related

nanostructures to achieve desired physicochemical properties and/or bring additional functionality. The work is organized into three main sections: the use of conformal deposition to introduce additional metal layer onto Au nanocages to broaden their applications; the exploration of deposition patterns in seed-mediated growth of Au nanocages; the synthesis of Au-based hollow nanostructures with reduced size; and the synthesis of Ag@Au core-sheath nanowires with improved stability against oxidation.

In Chapter 2, I describe a method for incorporating Cu directly into the crystal lattice of Au nanocages *via* the co-deposition of Au and Cu atoms onto the surface of pre-synthesized nanocages. The optical properties of the resulting Cu-doped Au nanocages were found to resemble those of the pristine Au nanocages, as characterized by strong absorption peaks in the NIR region. The Cu content in the resultant nanocages could be readily tuned by varying the thickness of the Au-Cu shells and/or altering the feeding ratio of Au to Cu precursors during a synthesis. When some Cu atoms in the alloy shell were substituted with ^{64}Cu, radioactive Au nanocages were obtained, which were then used as a PET tracer for cancer imaging. The nanocages showed effective accumulation in both 4T1 and PDX tumor models due to the EPR effect. Autoradiography analysis of the tumors also indicated a homogeneous intra tumoral distribution for the nanocages in both models.

In Chapter 3, I demonstrated the selective deposition of Pd on the outer surfaces or both the outer and inner surfaces of Au nanocages could be realized by controlling the reduction kinetics of the precursor. Specifically, if $PdCl_4^{2-}$ was used as a precursor to elemental Pd, its fast reduction kinetics favored the solution reduction pathway and the resultant Pd atoms were deposited on the outer surface only for the generation of Au@Pd double-shell nanocages. When switched to $PdBr_4^{2-}$ with slow reduction kinetics to support the surface reduction pathway, the precursor could readily diffuse into the interiors of Au nanocages prior to its reduction to elemental Pd. As such, both the outer and inner surfaces of the nanocages were coated with Pd for the generation of Pd@Au@Pd triple-shell nanocages.

In Chapter 4, I demonstrated a method for the synthesis of M@Au/Ag (M = Au, Pd and Pt) nanorattles with compact sizes. As a typical example, I prepared Au@Au/Ag nanorattles with an overall dimension of 15 nm and a wall thickness around 2.5 nm. The formation of ultrathin Au shells on the Au@Ag nanocubes prior to the galvanic replacement reaction is critical to the successful synthesis, in that it effectively enhanced their structural robustness. The compact nanorattles exhibited optical properties similar to those of Au nanocages with much larger dimensions and thick walls. The compact Au@Au/Ag nanorattles were able to effectively kill cancer cells upon laser irradiation, suggesting their great potential as effective photothermal transducers for cancer diagnostics and therapeutics.

In Chapter 5, I further developed the Au deposition method described in Chapter 4, and applied it to the synthesis of Ag@Au core-sheath nanowires. The Au-coated nanowires were identical to the pristine Ag nanowires in terms of morphology and optical properties, together with high transparency in the visible region. The as-prepared Ag@Au core-sheath nanowires exhibited greatly enhanced stability against oxidation by various types of oxidants, including O_2, H_2O_2, and $Fe(NO_3)_3$, qualifying them as a potential replacement for the conventional Ag nanowires in the fabrication of flexible transparent conductors.

1.4 Notes to Chapter 1

Part of this chapter is adapted from a review article entitled “Gold nanomaterials at work in biomedicine”, co-authored by me and published in *Chemical Reviews* [57].

1.5 References

[1] Gray, T.; Mann, N. *The Elements: A Visual Exploration of Every Known Atom in the Universe*; Black Dong & Leventhal Publishers, Inc.: New York, 2012.

[2] Tilling, R. I.; Gottfried, D.; Rowe, J. J. *Econ. Geol. Bull. Soc. Econ. Geol.* **1973,** *68*, 168–186.

[3] Faraday, M. *Philos. Trans. R. Soc. London* **1857,** *147*, 145–181.

[4] Mie, G. *Ann. Phys.* **1908,** *330*, 377–445.

[5] Cobley, C. M.; Chen, J.; Cho, E. C.; Wang, L. V.; Xia, Y. *Chem. Soc. Rev.* **2011,** *40*, 44–56.

[6] Xia, Y.; Halas, N. J. *MRS Bull.* **2005,** *30*, 338–348.

[7] Huang, X.; Neretina, S.; El-Sayed, M. A. *Adv. Mater.* **2009,** *21*, 4880–4910.

[8] Dreaden, E. C.; Alkilany, A. M.; Huang, X.; Murphy, C. J.; El-Sayed, M. A. *Chem. Soc. Rev.* **2012,** *41*, 2740–2779.

[9] Willets, K. A.; Van Duyne, R. P. *Annu. Rev. Phys. Chem.* **2007,** *58*, 267–297.

[10] Stiles, P. L.; Dieringer, J. A.; Shah, N. C.; Van Duyne, R. P. *Annu. Rev. Anal. Chem.* **2008,** *1*, 601–626.

[11] Campion, A.; Kambhampati, P. *Chem. Soc. Rev.* **1998,** *27*, 241–250.

[12] Qian, X.-M.; Nie, S. M. *Chem. Soc. Rev.* **2008,** *37*, 912–920.

[13] Aslan, K.; Gryczynski, I.; Malicka, J.; Matveeva, E.; Lakowicz, J. R.; Geddes, C. D. *Curr. Opin. Biotechnol.* **2005,** *16*, 55–62.

[14] Lakowicz, J. R. *Anal. Biochem.* **2001,** *298*, 1–24.

[15] Weissleder, R. *Nat. Biotechnol.* **2001,** *19*, 316–317.

[16] Daniel, M.-C.; Astruc, D. *Chem. Rev.* **2004,** *104*, 293–346.

[17] Ulman, A. *Chem. Rev.* **1996,** *96*, 1533–1554.

[18] Love, J. C.; Estroff, L. A.; Kriebel, J. K.; Nuzzo, R. G.; Whitesides, G. M. *Chem. Rev.* **2005,** *105*, 1103–1169.

[19] Whitesides, G. M.; Laibinis, P. E. *Langmuir* **1990,** *6*, 87–96.

[20] Lane, L. A.; Qian, X.; Smith, A. M.; Nie, S. *Annu. Rev. Phys. Chem.* **2015,** *66*, 521–547.

[21] Cho, E. C.; Zhang, Q.; Xia, Y. *Nat. Nanotechnol.* **2011,** *6*, 385–391.

[22] Cho, E. C.; Zhang, Y.; Cai, X.; Moran, C. M.; Wang, L. V.; Xia, Y. *Angew. Chem., Int. Ed.* **2013,** *52*, 1152–1155.

[23] Reynolds, R. A.; Mirkin, C. A.; Letsinger, R. L. *J. Am. Chem. Soc.* **2000,** *122*, 3795–3796.

[24] Wang, Z.; Lee, J. H.; Lu, Y. *Adv. Mater.* **2008,** *20*, 3263–3267.

[25] Li, H. X.; Rothberg, L. J. *Proc. Natl. Acad. Sci. U. S. A.* **2004,** *101*, 14036–14039.

[26] Tong, L.; Cobley, C. M.; Chen, J.; Xia, Y.; Cheng, J.-X. *Angew. Chem., Int. Ed.* **2010,** *49*, 3485–3488.

[27] Gobin, A. M.; Lee, M. H.; Halas, N. J.; James, W. D.; Drezek, R. A.; West, J. L. *Nano Lett.* **2007,** *7*, 1929–1934.

[28] Kneipp, K.; Haka, A. S.; Kneipp, H.; Badizadegan, K.; Yoshizawa, N.; Boone, C.; Shafer-Peltier, K. E.; Motz, J. T.; Dasari, R. R.; Feld, M. S. *Appl. Spectrosc.* **2002,** *56*, 150–154.

[29] Takahashi, H.; Niidome, Y.; Yamada, S. *Chem. Commun.* **2005,** 2247–2249.

[30] Poon, L.; Zandberg, W.; Hsiao, D.; Erno, Z.; Sen, D.; Gates, B. D.; Branda, N. R. *ACS Nano* **2010,** *4*, 6395–6403.

[31] Yavuz, M. S.; Cheng, Y.; Chen, J.; Cobley, C. M.; Zhang, Q.; Rycenga, M.; Xie, J.; Kim, C.; Song, K. H.; Schwartz, A. G.; Wang, L. V.; Xia, Y. *Nat. Mater.* **2009,** *8*, 935–939.

[32] Hirsch, L. R.; Stafford, R. J.; Bankson, J. A.; Sershen, S. R.; Rivera, B.; Price, R. E.; Hazle, J. D.; Halas, N. J.; West, J. L. *Proc. Natl. Acad. Sci. U. S. A.* **2003,** *100*, 13549–13554.

[33] von Maltzahn, G.; Park, J.-H.; Agrawal, A.; Bandaru, N. K.; Das, S. K.; Sailor, M. J.; Bhatia, S. N. *Cancer Res.* **2009,** *69*, 3892–3900.

[34] Chen, J.; Glaus, C.; Laforest, R.; Zhang, Q.; Yang, M.; Gidding, M.; Welch, M. J.; Xia, Y. *Small* **2010,** *6*, 811–817.

[35] Sun, Y.; Mayers, B. T.; Xia, Y. *Nano Lett.* **2002,** *2*, 481–485.

[36] Skrabalak, S. E.; Au, L.; Li, X.; Xia, Y. *Nat. Protoc.* **2007,** *2*, 2182–2190.

[37] Skrabalak, S. E.; Chen, J.; Sun, Y.; Lu, X.; Au, L.; Cobley, C. M.; Xia, Y. *Acc. Chem. Res.* **2008,** *41*, 1587–1595.

[38] Sun, Y.; Xia, Y. *Science* **2002,** *298*, 2176–2179.

[39] Wan, D.; Xia, X.; Wang, Y.; Xia, Y. *Small* **2013,** *9*, 3111–3117.

[40] Au, L.; Chen, Y.; Zhou, F.; Camargo, P. H. C.; Lim, B.; Li, Z.-Y.; Ginger, D. S.; Xia, Y. *Nano Res.* **2008,** *1*, 441–449.

[41] Wang, Y.; Wan, D.; Xie, S.; Xia, X.; Huang, C. Z.; Xia, Y. *ACS Nano* **2013,** *7*, 4586–4594.

[42] Lu, X.; Au, L.; McLellan, J.; Li, Z.-Y.; Marquez, M.; Xia, Y. *Nano Lett*. **2007,** *7*, 1764–1769.

[43] Sun, Y.; Xia, Y. *J. Am. Chem. Soc.* **2004,** *126*, 3892–3901.

[44] Wang, Y.; Zheng, Y.; Huang, C. Z.; Xia, Y. *J. Am. Chem. Soc.* **2013,** *135*, 1941–1951.

[45] Cobley, C. M.; Xia, Y. *Mater. Sci. Eng., R* **2010,** *70*, 44–62.

[46] Zhang, Q.; Li, W.; Moran, C.; Zeng, J.; Chen, J.; Wen, L.-P.; Xia, Y. *J. Am. Chem. Soc.* **2010,** *132*, 11372–11378.

[47] Zhang, Q.; Li, W.; Wen, L.-P.; Chen, J.; Xia, Y. *Chem.-Eur. J.* **2010,** *16*, 10234–10239.

[48] Chen, J.; Yang, M.; Zhang, Q.; Cho, E. C.; Cobley, C. M.; Kim, C.; Glaus, C.; Wang, L. V.; Welch, M. J.; Xia, Y. *Adv. Funct. Mater.* **2010,** *20*, 3684–3694.

[49] Ruditskiy, A.; Xia, Y. *J. Am. Chem. Soc.* **2016,** *138*, 3161–3167.

[50] Sun, X.; Kim, J.; Gilroy, K. D.; Liu, J.; König, T. A. F.; Qin, D. *ACS Nano* **2016,** *10*, 8019–8025.

[51] Sun, T.; Wang, Y.; Wang, Y.; Xu, J.; Zhao, X.; Vangveravong, S.; Mach, R. H.; Xia, Y. *Adv. Healthcare Mater.* **2014,** *3*, 1283–1291.

[52] Moon, G. D.; Choi, S.-W.; Cai, X.; Li, W.; Cho, E. C.; Jeong, U.; Wang, L. V.; Xia, Y. *J. Am. Chem. Soc.* **2011,** *133*, 4762–4765.

[53] Yang, X.; Skrabalak, S. E.; Li, Z.-Y.; Xia, Y. *Nano Lett.* **2007,** *7*, 3798–3802.

[54] Kim, C.; Cho, E. C.; Chen, J.; Song, K. H.; Au, L.; Favazza, C.; Zhang, Q.; Cobley, C. M.; Gao, F.; Xia, Y.; Wang, L. V. *ACS Nano* **2010,** *4*, 4559–4564.

[55] Wang, Y.; Liu, Y.; Luehmann, H.; Xia, X.; Brown, P.; Jarreau, C.; Welch, M. J.; Xia, Y. *ACS Nano* **2012,** *6*, 5880–5888.

[56] Wang, Y.; Liu, Y.; Luehmann, H.; Xia, X.; Wan, D.; Cutler, C.; Xia, Y. *Nano Lett.* **2013,** *13*, 581–585.

[57] Yang, X.; Yang, M.; Pang, B.; Vara, M.; Xia, Y. *Chem. Rev.* **2015,** *115*, 10410–10488.

CHAPTER 2

RADIOACTIVE GOLD NANOCAGES FOR POSITRON EMISSION TOMOGRAPHY

2.1 Introduction

Gold nanostructures have been extensively explored for biomedical applications in recent years owning to their remarkable physicochemical properties [1−3]. Gold is biologically inert and yet its surface can be easily functionalized with different thiol-based ligands through the formation of Au-S bond in a well-controlled manner [4]. For Au nanostructures such as nanorods [5], nanoshells [6], and nanocages [7], their localized surface plasmon resonance (LSPR) peaks could be readily tuned from the visible to the near-infrared (NIR) region, making them particularly favorable for *in vivo* applications due to the deep penetration depth of soft tissues at these wavelengths [8]. As a result, these Au nanostructures have been extensively explored as drug delivery carriers, imaging contrast agents, and photothermal transducers for cancer theranostics [9−14].

To achieve their full potential in cancer theranostics, it is necessary to label Au nanostructures with additional probes so that they can be used for imaging-guided therapy to achieve enhanced treatment efficiency. Among the various imaging techniques, one particularly interesting modality is based upon radionuclide-labeling, as represented by positron emission tomography (PET). This imaging modality is extremely sensitive, and a quantitative analysis of whole-body imaging can be acquired with the introduction of only a trace amount of the probe [15, 16]. To be resolved by PET, Au nanostructures need to be labelled with a radioactive isotope. Owing to its desirable nuclear properties (half-life = 12.7 h, β^+ = 17%, and β^- = 40%), ^{64}Cu has emerged as one of the most commonly-used isotopes in nanomedicine [15, 16]. In a typical labelling process, $^{64}Cu^{2+}$ is attached to the surface of a Au nanostructure through the use of a macrocyclic chelating ligand, such as

1,4,7,10-tetraazacyclododacane-1,4,7,10-tetraacetic acid (DOTA) [15, 17, 18]. Despite the extensive use, this approach is marred by the complex procedures required for the synthesis and purification. Besides, there is a potential issue with regard to the *in vivo* stability of the chelated $^{64}Cu^{2+}$ ions, which could be transchelated to proteins, resulting in high uptake in non-targeted organs and thus misinterpretation of the PET images [19]. In addition, the presence of surface-bound macrocyclic ligands will inevitably modify the characteristics of Au nanostructures and reduce the loading capability of other ligands for the targeting or therapeutic purpose. To address these issues, an alternative labeling approach has recently been developed, by which ^{64}Cu atoms were directly incorporated into the crystal lattice of Au nanoparticles [20−23]. The resultant nanoparticles showed enhanced performance, with greatly improvement in radiolabeling stability and superior targeting efficiency without suffering from the aforementioned issues. Despite these successful attempts, there is still room for improvement by developing a facile and reliable method for radiolabeling with ^{64}Cu atoms, especially for Au nanostructures with strong absorption in the NIR region.

In this work, I demonstrated a facile synthesis of Cu-doped Au nanocages through the co-titration, co-reduction, and co-deposition of Au and Cu atoms onto the surfaces (both outer and inner) of pre-synthesized Au nanocages. The amount of Cu component incorporated in the final nanostructures could be readily controlled by varying the total amount of Au and Cu atoms, as well as the molar ratio of Au to Cu, deposited on the nanocages. The Cu content could be varied from 2.2% to 10.2% (mole percentage) while the structure, morphology, and physicochemical properties of the initial Au nanocages could be largely retained. Significantly, radioactive ^{64}Cu could be easily incorporated when $^{64}CuCl_2$ was used in combination with the non-radioactive $CuCl_2$ during a synthesis. The alloy structure ensured excellent radiolabel stability, enabling their sensitive and accurate detection in a mouse 4T1 triple-negative breast cancer (TNBC) model and a patient derived xenograft (PDX) tumor model. Additionally, autoradiography of tumor tissues showed a homogeneous intra-tumoral distribution for the ^{64}Cu-doped Au nanocages because of their

hollow structure, as our group reported previously [24]. These ^{64}Cu-doped Au nanocages are expected to find use in an array of applications related to cancer theranostics, including imaging-guided drug delivery and photothermal therapy.

2.2 Results and Discussion

First, I developed the synthetic protocol by focusing on non-radioactive materials. Figure 2.1 shows a schematic illustration of the structural changes involved in the co-deposition of Au and Cu atoms on pre-synthesized Au nanocages.

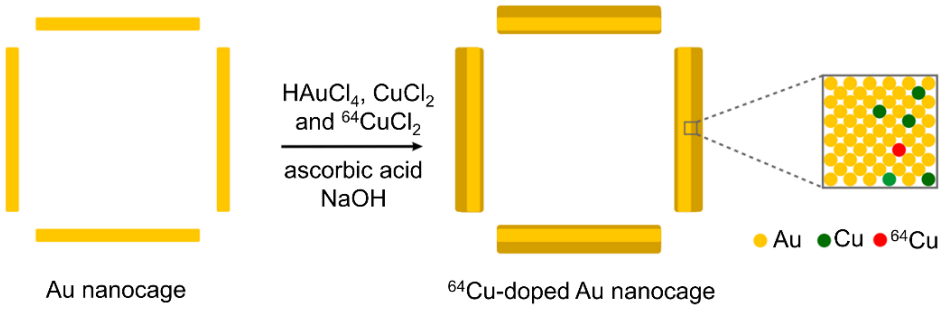

Figure 2.1. Schematic illustration showing the synthesis of ^{64}Cu-doped Au nanocages through co-deposition of Au and Cu atoms onto the surface of pre-synthesized Au nanocages [37]. Printed with permission from John Wiley & Sons. Copyright 2017.

Figure 2.2A shows a representative TEM image of the original Au nanocages, characterized by well-defined hollow interiors, ultrathin walls, and openings at the corner sites. They were prepared using a new method recently developed by the Qin group at Georgia Tech [25]. The nanocages had an average edge length of 38.6 ± 2.5 nm, together

with a wall thickness of 2.8 ± 0.3 nm. The average edge length of the cubic cavities inside the nanocages was 33.0 ± 2.4 nm. The average size of the openings was estimated to be ca. 8.0 nm by counting 100 particles. In a typical process for the co-deposition of Au and Cu atoms, aqueous solutions of $HAuCl_4$ and $CuCl_2$ were titrated simultaneously into a suspension containing the Au nanocages, ascorbic acid (AA), and NaOH using a syringe pump. Poly(vinyl pyrrolidone) (PVP) was added as a colloidal stabilizer to prevent the nanostructures from aggregation. The final solid products were collected by centrifugation and a typical TEM image is shown in Figure 2.2B. The morphology of these nanocages was essentially identical to the original nanocages, including the well-defined hollow interiors and the openings at the corner sites. The average edge length was increased to 41.0 ± 1.5 nm, as measured from the TEM images. The average edge length of the cubic cavities inside the nanocages was reduced to 32.8 ± 1.5 nm. Compared to the original Au nanocages, the average wall thickness was increased by ca. 1.3 nm to 4.1 ± 0.3 nm due to the co-deposition of Au and Cu atoms on both the outer and inner surfaces. In addition, there was a clear size reduction for the pores at the corner sites. The average size of the openings became 5.4 nm, which was about 2.6 nm smaller than the initial pores. This observation correlated well with our previous report, in which pure Au was deposited onto Au nanocages [26].

The thickness of the deposited Au-Cu shell could be readily tuned by varying the total amount of metal precursors added into the reaction system. When I tripled the amount of the metal precursors added, nanocages with thicker Au-Cu overlayers were obtained (Figure 2.2C), with an increase of 3.6 nm for the wall thickness. The average edge length of the nanocages was increased to 43.7 ± 1.9 nm, while the average edge length of the cubic cavities inside the nanocages was further reduced to 31.0 ± 1.8 nm. I could still observe well-defined openings at the corners although their average size was reduced to ca. 4.0 nm. These nanocages still showed a smooth outer surface, suggesting the relatively small

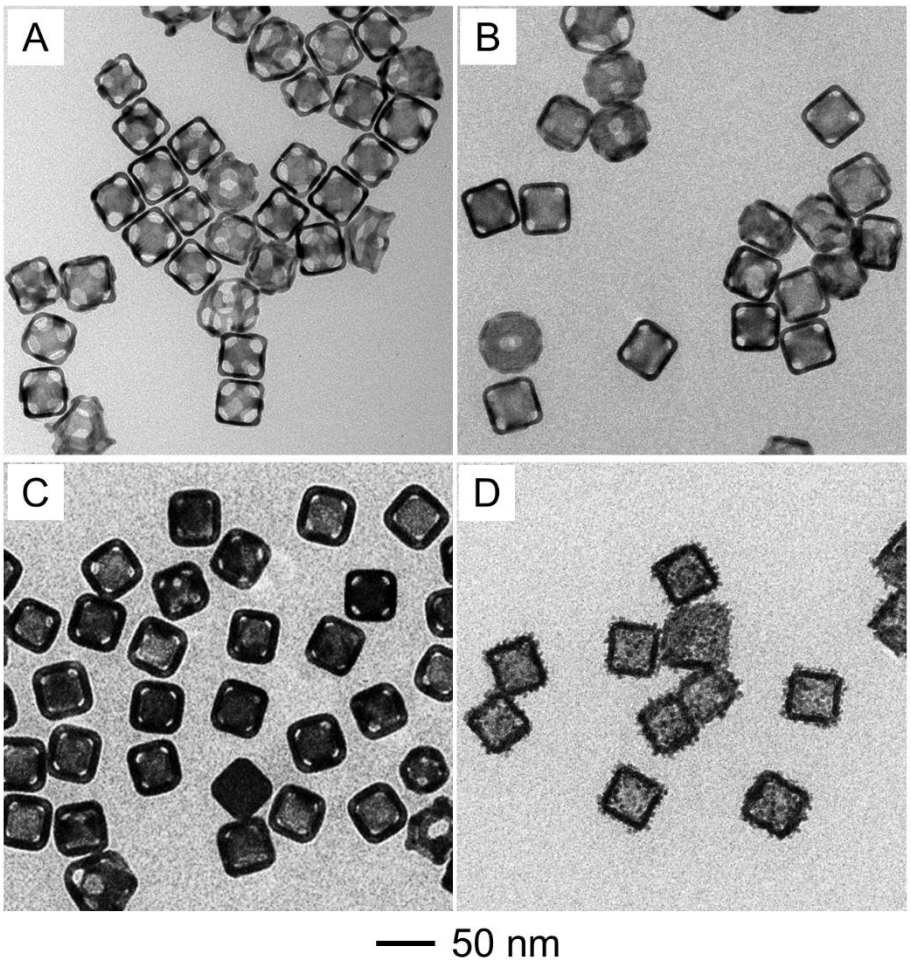

Figure 2.2. TEM images of Au nanocages (A) before and (B, C) after coating with Au-Cu alloy shells of (B) 1.3 nm and (C) 3.6 nm, respectively, in thickness. (D) Cu-doped Au nanocages with increased Cu ratio (wall thickness of 3.0 nm) [37]. Printed with permission from John Wiley & Sons. Copyright 2017.

amount of Cu incorporated into the shell had essentially no effect on the overall morphology because the deposition was conformal and uniform.

With the presence of pores on the surface, it is reasonable to assume that the metal precursors could also access the hollow interior of a nanocage through diffusion for their reduction and deposition on the inner surface. To gain more information about this issue, I systematically analyzed the size of void space inside the nanocage before and after the metal deposition. According to the TEM images, the overall edge lengths of the nanocages shown in Figure 2.2, B and C, were measured to be ca. 41.0 and 43.7 nm, respectively. The average edge length of the cubic cavities inside the nanocages were 32.8 nm and 31.0 nm, respectively, for these two samples. For the pristine Au nanocages, their cubic cavities had an average edge length of 33.0 nm. From these numbers, the void space did shrink during the co-deposition of Au and Cu, clearly indicating the involvement of inner surface. However, the amount of Au and Cu deposited on the inner surface of a nanocage was much lower compared to that deposited on the outer surface. The thickness of the Au-Cu overlayers deposited on the outer and inner surfaces of the nanocages were 1.2 and 0.1 nm, respectively, for the sample shown in Figure 2.2B, and 2.6 nm *vs.* 1.0 nm for the sample shown in Figure 2.2C. The dominance of deposition on the outer surface can be attributed to the faster reduction of metal precursors by AA under alkaline condition, which worked to minimize the "lifespan" of metal ions between their introduction into the reaction solution and their reduction to zero-valent atoms and being deposited. The short "lifespan" of metal ions serves to lower the possibility for them to access the hollow interiors of nanocages through the pores.

If the Cu-doped nanocages are used for imaging purpose, the most critical parameter is the Cu content in the final structures. A higher Cu content can decrease the amount of nanomaterials needed for PET imaging, which could potentially reduce the toxicity and side effects brought by the nanomaterial-based probes. Given that all the Cu content in the Cu-doped nanocages comes from the Au-Cu alloy overlayers, it is feasible to control the

Cu content by controlling the total amount of Au and Cu deposited. To this end, I analyzed the elemental compositions (Au and Cu) of the nanostructures involved in this study using inductively coupled plasma mass spectrometry (ICP-MS). With the presence of thicker Au-Cu overlayers (3.6 nm), a higher Cu content of 5.3% (mole percentage) was achieved, while this number dropped to 2.2% when thinner Au-Cu overlayers (1.3 nm) were involved. These data indicate that the Cu level can be readily tuned by varying the thickness of the Au-Cu overlayers by varying the amount of metal precursors added during the deposition process.

Another possible approach to adjust the Cu component is to vary the molar ratio of Au to Cu in the deposited alloy shell by manipulating the feeding ratio of the two metal precursors. When the total amount of metal atoms (Au plus Cu) to be deposited remains constant, the molar ratio of the two components is proportional to the concentrations of their corresponding precursor solutions, given that the same volume is involved. Along this concept, I varied the concentration ratio of the precursor solutions ($HAuCl_4$:$CuCl_2$) from the previously used 9:1 to 3:1. Specifically, aqueous solutions of $HAuCl_4$ (0.075 mM) and $CuCl_2$ (0.025 mM) were used for the synthesis instead of the previously used concentrations (0.09 mM for $HAuCl_4$ and 0.01 mM for $CuCl_2$). Other parameters, such as the titration rates and the injection volumes of the precursor solutions, were kept the same as those used for the preparation of 43.7 nm nanocages shown in Figure 2.2C, in order to maintain a similar thickness for the Au-Cu shells. The resultant nanocages are shown in Figure 2.2D, with an average wall thickness of 5.8 ± 0.5 nm (corresponding to the deposition of a Au-Cu shell of 3.0 nm in thickness). However, these nanocages showed a rough outer surface, with the presence of many small particle-like branches. This morphology was quite different from what was observed in the previous syntheses, where the products with a smooth outer surface were obtained. This difference was caused by the increased ratio of Cu in the alloy shell and thus the increase in strain because of their different lattice constants: 0.3597 nm for Cu and 0.4065 nm for Au. More importantly, the

reduction rate of Cu^{2+} is much faster compared to that of $AuCl_4^-$, and as such self-nucleation of Cu came into play when I increased the feeding concentration of $CuCl_2$ solution from 0.01 mM to 0.025 mM. As a result, small particles of Cu were formed for their attachment to the outer surface of the Au nanocages, leading to a rough outer surface for the final product. The ICP-MS data confirmed a higher Cu content of 10.2% for this sample, validating an alternative way to tune the Cu level in the final products by varying the concentration ratio of the precursor solutions during the synthesis.

UV-vis spectroscopy was used to monitor the optical properties of the Au nanocages and the three samples of the Cu-doped Au nanocages. The results are shown in Figure 2.3.

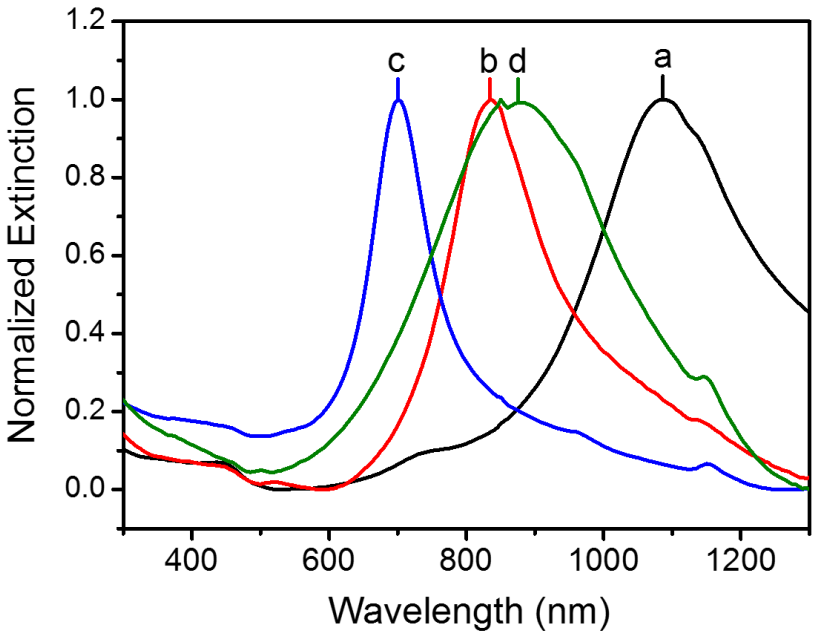

Figure 2.3. UV-vis spectra of Au nanocages (a) before and (b−d) after coating with Au-Cu alloy shells of various thicknesses: (b) 1.3 nm, (c) 3.6 nm, and (d) 3.0 nm (with a rough surface) [37]. Printed with permission from John Wiley & Sons. Copyright 2017.

The pristine Au nanocages had a LSPR peak at 1085 nm, due to their hollow interiors and ultrathin walls. After the deposition of Au-Cu alloy shells, an increase in the overall wall thickness led to a blue-shift for the LSPR peak. For the Cu-doped Au nanocages with an average wall thickness of 4.1 nm, the LSPR peak was shifted to 835 nm. A further blue-shift to 705 nm was observed when I increased the wall thickness to 6.4 nm by depositing more Au and Cu atoms. This observation was consistent with the experimental results and theoretical calculation reported previously for Au-Ag alloyed nanocages [26, 27]. When the Cu content was increased by raising the molar ratio of Cu to Au, the resulting rough surface caused a red-shift for the LSPR peak to 880 nm. A similar trend has been reported in literature for Au-based nanostructures with rough surfaces [28]. In summary, all the Cu-doped Au nanocages synthesized in this study showed LSPR peaks in the NIR region while their wall thicknesses were varied in the range of 4.1−6.4 nm. The NIR absorption makes these nanomaterials ideal for biomedical applications, such as photothermal therapy, photoacoustic imaging, and controlled release, due to the high transparency of water and soft tissues in this “biological transparency window”.

Apart from experimental measurements, my colleagues and I have also used discrete dipole approximation (DDA) to calculate the extinction spectra of all the four different samples of Au nanocages shown in Figure 2.2. For the pristine Au nanocages, we assumed they had the geometry of a hollow cube with an edge length of 40 nm, a wall thickness of 3 nm, and 1/8 of spherical pores (12.5 nm in radius) at all corners. The dielectric constant was extracted from literature for Ag and Au compositions set to 48% and 52%, respectively (similar to the 1:1 ratio measured by ICP-MS) [29]. To model the Cu-doped Au nanocages with smooth surfaces, we added an additional solid layer made of Au-Cu alloy with a thickness of 1 and 3.5 nm on the outer surface of the original Au nanocages. The dielectric constant of the Au-Cu alloy was taken to be pure Au, which we considered to be a valid assumption for two reasons: *i*) Au dominated Cu in the deposited shell with a measured ratio of approximately 10:1, and *ii*) the dielectric constants of pure Au and Cu are very

close over the wavelength range of interest. For the modelling of Cu-doped Au nanocages with rough surfaces (Figure 2.2D), a 46-nm Au cubic box with a 40-nm void in the center (wall thickness of 3 nm) was created. Then, 2-nm of Au spheres were placed periodically on the corners, edges, and faces of the nanobox, spaced from one another at a 11.5 nm increment. The calculated extinction spectra were shown in Figure 2.4, and a similar trend was observed for the evolution of LSPR peaks when compared with the experimental results, with the peak positions in reasonable agreement with the experimental data shown in Figure 2.3A.

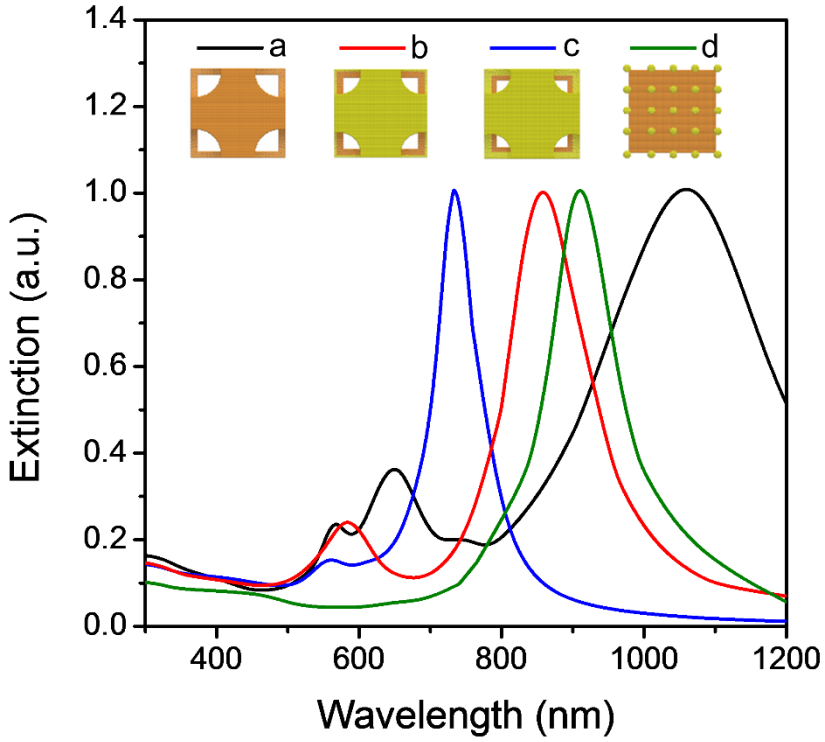

Figure 2.4. Extinction spectra calculated using the DDA method for (a) a pristine Au nanocage; (b) a Au nanocage coated with a Au-Cu alloy shell of 1 nm in thickness; (c) a Au nanocage coated with a Au-Cu alloy shell of 3 nm in thickness; and (d) a Au nanocage coated with a roughened Au-Cu alloy shell of 2 nm in thickness [37]. Printed with permission from John Wiley & Sons. Copyright 2017.

Next, I prepared radioactive, ^{64}Cu-doped Au nanocages by following the same synthetic protocol described above except for the replacement of some $CuCl_2$ with $^{64}CuCl_2$. As shown in Figure 2.5, the radioactivity of the ^{64}Cu-doped Au nanocages increased linearly with the radioactivity of $^{64}CuCl_2$ precursor used for the synthesis. The specific activity of the ^{64}Cu-doped Au nanocages was calculated to be 55 mCi nmol^{-1} when 200 μCi of $^{64}CuCl_2$ was used for the co-deposition, enabling the trace amount (0.6 pmol) administration for PET imaging. Given the presence of a large amount of non-radioactive Cu^{2+} in the $^{64}CuCl_2$ precursor [30], there is still room to further improve the specific activity of the ^{64}Cu-doped Au nanocages.

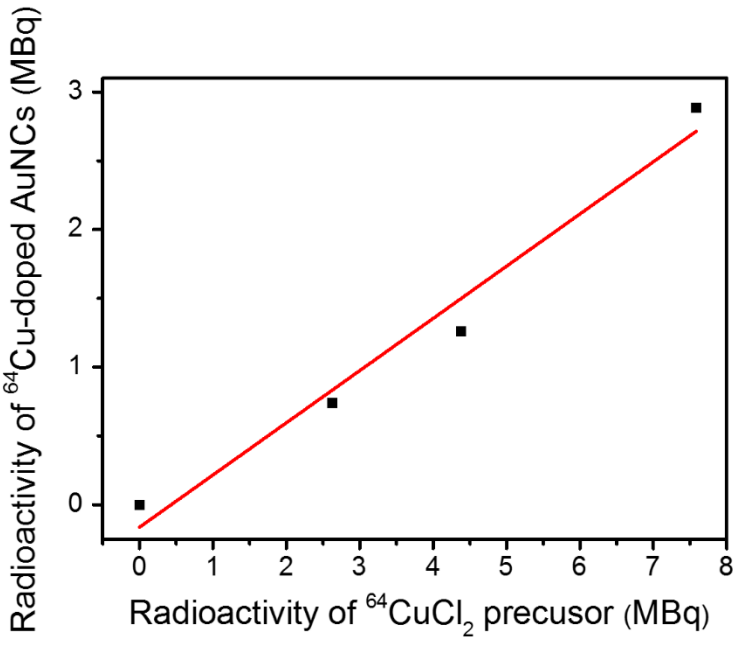

Figure 2.5. Correlation between the radioactivity of the $^{64}CuCl_2$ precursor used in a synthesis and the resultant ^{64}Cu-doped Au nanocages [37]. Printed with permission from John Wiley & Sons. Copyright 2017.

After incorporation of ^{64}Cu, the as-obtained Au nanocages were PEGylated with thiol terminated methoxy polyethylene glycol (mPEG-SH) *via* the Au-S linkage. Both 4T1 and PDX tumor models were used for *in vivo* PET imaging with the PEGylated, ^{64}Cu-doped nanocages. As shown in Figure 2.6A, PET/CT images clearly showed accumulation of the ^{64}Cu-doped nanocages in both 4T1 and PDX models at 24 h post tail vein injection. Interestingly, the intra-tumoral distributions of the nanocages were relatively homogeneous (Figure 2.6B), consistent with our previous report [24], despite the difference in cancer model and the heterogeneity of each tumor. This unique feature is particularly important in cancer photothermal treatment for ensuring the complete ablation of tumor and improving the treatment efficacy. The quantification of tumor uptake in both models demonstrated an effective and gradually increased accumulation (Figure 2.6C). The localizations of PEGylated ^{64}Cu-doped nanocages in 4T1 tumors (4.12 $\pm$ 0.29 %ID/g and 6.71 $\pm$ 0.52 %ID/g at 4 h and 24 h post injection, respectively) were comparable to the results acquired in other breast cancer xenografts [19, 24]. However, their accumulation in the PDX model was significantly reduced at both time points (4 h: 1.58 $\pm$ 0.25 %ID/g, $p < 0.0005$, $n = 3$; 24 h: 3.08 $\pm$ 0.86 %ID/g, $p < 0.005$, $n = 3$).

My colleagues and I further investigated the whole body distribution profiles of the PEGylated, ^{64}Cu-doped Au nanocages. As shown in Figure 2.7, these nanocages showed comparable accumulation in all organs tested except for tumor tissues between the 4T1 and PDX models at 24 h post injection. Consistent with PET imaging, the tumor accumulation of the nanocages in 4T1 tumors (6.49 $\pm$ 0.20 %ID/g, $p < 0.0005$) was significantly higher than that in the PDX tumors (3.19 $\pm$ 0.47 %ID/g). It is known that tumor vasculature plays an important role in nanostructure enhanced permeability and retention (EPR) effect. Given the comparable blood retentions of the nanocages in both tumor models, the difference in tumor accumulation can be likely attributed to the variation in tumor vasculature [31]. Since the PDX model not only retains the architecture and stromal components of the

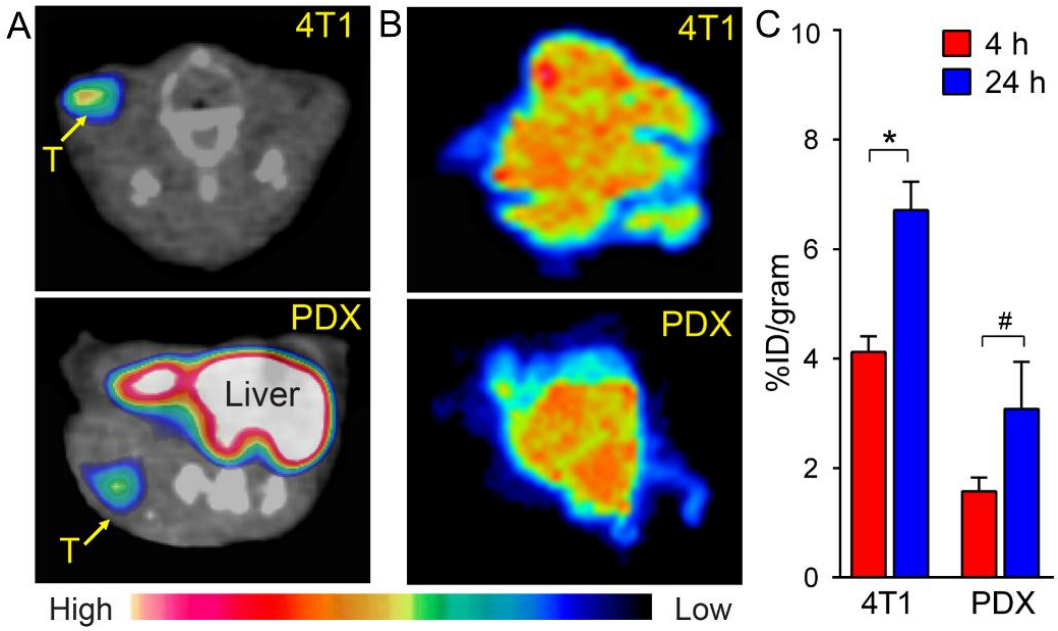

Figure 2.6. (A) Transverse PET/CT images of the PEGylated, ^{64}Cu-doped Au nanocages in mice 4T1 and PDX tumor models at 24 h post injection. (B) Autoradiography showing a relatively homogeneous distribution profile for Au nanocages in both tumor models. (C) Quantification of tumor uptake in both tumor models. *$p < 0.0005$, $^{\#}p < 0.005$ [37]. Printed with permission from John Wiley & Sons. Copyright 2017.

original tumor but also replicates the phenotypic and molecular characteristics of the original human cancer [32], this finding demonstrated the translational potential of the ^{64}Cu-doped nanocages for effective TNBC photothermal therapy, as well as the importance of using PDX tumor model to better assess the effectiveness of nanostructures for cancer imaging and therapy.

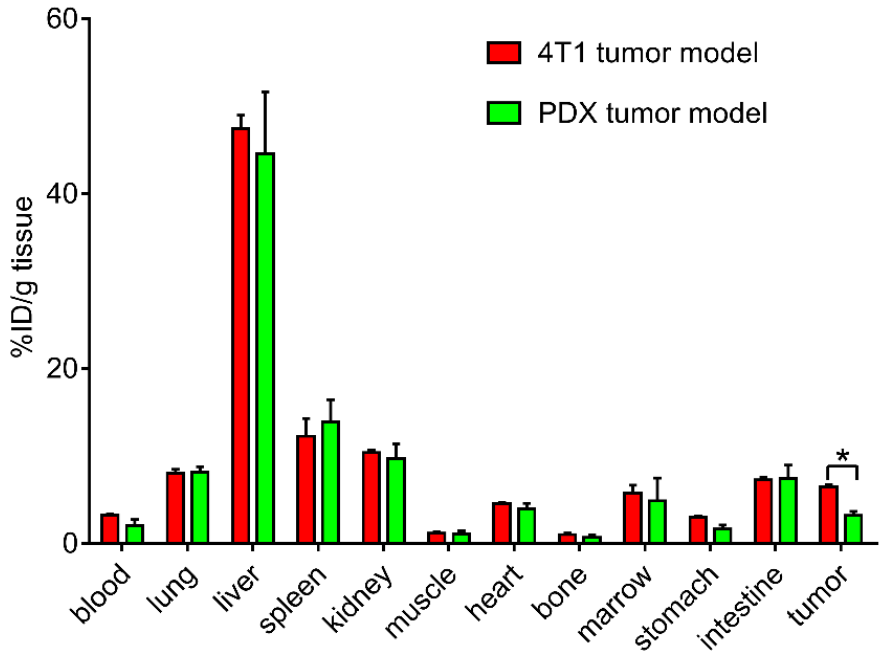

Figure 2.7. A comparison of the *in vivo* distribution profiles of the PEGylated, ^{64}Cu-doped Au nanocages in both 4T1 and PDX tumor models at 24 h post injection. *$p < 0.0005$ [37]. Printed with permission from John Wiley & Sons. Copyright 2017.

2.3 Conclusion

In summary, I have demonstrated the synthesis of Au nanocages with Cu atoms being directly incorporated into the crystal lattice via the co-deposition of Au and Cu atoms onto

the surface of pre-synthesized Au nanocages. Based on experimental results and theoretical calculations, the optical properties of these Cu-doped nanocages resemble those of the pristine Au nanocages, with strong absorption peaks in the NIR region. The Cu content in the new nanocages could be easily tuned by varying the thickness of the Au-Cu shells and/or altering the feeding ratio of Au to Cu precursors during a synthesis. With the substitution of some Cu atoms in the alloy shell with ^{64}Cu, radioactive Au nanocages were obtained with controllable radioactivity. After PEGylation, these radioactive nanocages were used as PET tracer for cancer imaging and demonstrated effective accumulation in both 4T1 and PDX tumor models because of the EPR effect. Autoradiography analysis of the tumors indicated a homogeneous intra-tumoral distribution for the nanocages in both models. Taken together, this study demonstrates that the radioactive Au nanocages have great potential in imaging-guided cancer theranostics.

2.4 Experimental Section

Chemicals and Materials. *L*-ascorbic acid (> 99.0%), sodium hydroxide (NaOH, >98%), poly(vinyl pyrrolidone) ($M_W \approx 55{,}000$), hydrogen tetrachloroaurate trihydrate ($HAuCl_4 \cdot 3H_2O$, >99.9%) and copper(II) chloride dihydrate ($CuCl_2 \cdot 2H_2O$, >99.0%) were all obtained from Sigma-Aldrich (St. Louis, MO). Thiol terminated methoxy polyethylene glycol ($M_W \approx 2{,}000$) was purchased from Laysan Bio (Arab, AL). All chemicals were used as received. Deionized water with a resistivity of 18.2 MΩ·cm was used throughout the experiment.

Synthesis of Au Nanocages. The Au nanocages were synthesized from Ag nanocubes through a two-stage method by following a recently reported protocol [25]. In a typical synthesis, 2 mL of aqueous PVP (1 mM) was added to a 20 mL vial, followed by 0.5 mL of aqueous NaOH (200 mM), 0.5 mL of aqueous AA (100 mM), and 40 μL of Ag nanocube suspension. To the reaction mixture, 0.4 mL of aqueous $HAuCl_4$ (0.1 mM) was injected at a rate of 0.02 mL min^{-1} using a syringe pump. After completing the titration of Au

precursor, the reaction mixture was maintained under magnetic stirring for additional 5 min. The solid products were collected by centrifugation at 8000 rpm for 10 min. After removing the supernatant, the pellet was re-dispersed in an aqueous solution containing PVP (0.7 mM) and AA (30 mM), and this suspension was incubated at room temperature (22 ℃). After 20 min, the particles were collected by centrifugation and re-dispersed in 0.1 mL DI water. At the end, 1 mL of aqueous H_2O_2 (3%) was added to selectively etch away the Ag component. The resultant Au nanocages were collected by centrifugation and re-dispersed in 100 μL of DI water for future use.

Synthesis of Cu-doped Au Nanocages. The Cu-doped Au nanocages were prepared through the co-deposition of Au and Cu onto pre-synthesized Au nanocages. In a typical synthesis, 2 mL of aqueous PVP (1 mM) was added into a 20 mL vial, followed by 0.5 mL of aqueous NaOH (200 mM), 0.5 mL of aqueous AA (100 mM), and 100 μL of the Au nanocage suspension. To this vial, aqueous solutions of $HAuCl_4$ (0.09 mM, 0.3 mL) and $CuCl_2$ (0.01 mM, 0.3 mL) were titrated simultaneously using a syringe pump at an injection rate of 0.02 mL min^{-1}. The reaction mixture was maintained under magnetic stirring for additional 5 min after the titration had been complete. The solid products were separated by centrifugation, washed twice with DI water, and finally re-dispersed in 100 μL DI water.

Synthesis of Radioactive ^{64}Cu-doped Au Nanocages. The ^{64}Cu-doped Au nanocages were synthesized using the same protocol as the one for the non-radioactvive nanocages, except that the aqueous $CuCl_2$ solution was replaced with a mixture of $CuCl_2$ and a small amount of radioactive $^{64}CuCl_2$. The total radioactivity of $^{64}CuCl_2$ used in the synthesis was 600 μCi. After purification, ^{64}Cu-doped nanocages with a radioactivity of 234 μCi were obtained.

PEGylation of ^{64}Cu-doped Au Nanocages. For PEGylation, 100 μL of aqueous mPEG-SH (10 mg mL^{-1}) was added into a suspension containing the ^{64}Cu-doped nanocages (200 μCi) and the mixture was stirred for 1 h at room temperature. This was enough for the ligand exchange process between the PVP molecules anchored on the

nanocages and the mPEG-SH molecules. Afterwards, the solid sample was collected by centrifugation and washed with DI water to remove excess PEG. The final product was re-suspended in PBS at a final radioactivity concentration of 300 μCi mL^{-1}.

Mouse Tumor Model. All animal used were purchased from Charles River Laboratories with related procedures approved by the Washington University Animal Studies Committee. The 4T1 tumor model was generated by orthotopical injection of 3×10^5 cancer cells in 100 μL of saline at the mammary fat pad (right) of 7-week old female BALB/c mice. The tumors were allowed to grow for 2 weeks to reach a size of 200−300 mm^3 before the biodistribution and PET imaging studies.

Washington University Human-in-Mouse (WHIM) line 12 was established and characterized previously and passaged subcutaneously in the NSG mice to establish the PDX tumor model [33, 34]. For the generation of WHIM12 tumor-bearing mice, 1×10^6 cancer cells re-suspended in 60 μL of Collagen: Matrigel (1:1 v/v) were injected into the right flank of 8-week old female NSG mice. The tumors were allowed to grow for 4 weeks to reach a size of 200−300 mm^3 before the bio-distribution and PET imaging studies.

PET Imaging of the ^{64}Cu-doped Au Nanocages. PET imaging was employed to assess the passive accumulation of PEGylated ^{64}Cu-doped Au nanocages in both 4T1 and PDX tumor models (n = 3). The tumor-bearing mice were injected intravenously with the PEGylated ^{64}Cu-doped Au nanocages in 100 μL of saline suspension (approximately 30 μCi/mouse). MicroPET scans were performed on Inveon PET/CT system (Siemens, Malvern, PA) at 24 h post injection. All the PET scanners were cross-calibrated periodically.

Bio-distribution of ^{64}Cu-doped Au Nanocages. After PET imaging, the mice were sacrificed *via* cervical dislocation and organs of interest were collected, weighted and counted in a Beckman 8000 gamma counter (Beckman, Fullterton, CA). The distribution profiles of the ^{64}Cu-doped Au nanocages were calculated based on standards, and presented as percentage of injected dose in per gram of tissue (%ID/g).

Autoradiographic Imaging. Tumors tissues from the mice bearing 4T1 and PDX tumor were fixed in 4% paraformaldehyde, embedded, and sectioned into slices with a *ca.* 40 μm thickness using a Vibratome 8850 whole body cryomicrotome (SIMS Co., Ltd., Tokyo, Japan). 2D autoradiography of tumor section was generated by using an Instant Imager Electronic Autoradiography system (Packard, Meriden, CT). Images were acquired and analyzed using the Imager software (Packard, Meriden, CT).

Statistical Analysis. Triplicate data were analyzed *via* student *t* test by using GraphPad Prism (version 7.0) on the significance level of $p < 0.005$. Significant differences are indicated by asterisks in the Figures.

Discrete Dipole Approximation (DDA) Calculation. The Discrete Dipole Approximation (DDSCAT 7.3) software package was used to simulate the optical properties of all the structures discussed herein [35]. The simulated structures consisted of a finite array of polarizable points whose structure and composition were derived from TEM images and ICP-MS measurements, respectively. Furthermore, more than 10^5 dipoles were used in all simulations to ensure accurate results. The dielectric constants of pure Au and Cu were taken from Johnson and Christy [36] while the dielectric constant of the $Au_{52}Ag_{48}$ alloy was extracted from Peña-Rodr ǵuez [28]. The dielectric constant of the Au-Cu alloy was taken to be pure Au. The dielectric constant of the medium and void spaces was taken to be $\varepsilon_m = n^2 = 1.78$.

2.5 Notes to Chapter 2

Part of this chapter is adapted from a paper entitled “Facile synthesis of ^{64}Cu-doped Au nanocages for positron emission tomography imaging”, which was co-authored by me and published in *ChemNanoMat* [37].

2.6 References

[1] Huang, X.; Neretina, S.; El-Sayed, M. A. *Adv. Mater.* **2009,** *21*, 4880−4910.

[2] Dreaden, E. C.; Alkilany, A. M.; Huang, X.; Murphy, C. J.; El-Sayed, M. A. *Chem. Soc. Rev.* **2012,** *41*, 2740−2779.

[3] Yang, X.; Yang, M.; Pang, B.; Vara, M.; Xia, Y. *Chem. Rev.* **2015,** *115*, 10410−10488.

[4] Love, J. C.; Estroff, L. A.; Kriebel, J. K.; Nuzzo, R. G.; Whitesides, G. M. *Chem. Rev.* **2005,** *105*, 1103−1170.

[5] Murphy, C. J.; Sau, T. K.; Gole, A. M.; Orendorff, C. J.; Gao, J.; Gou, L.; Hunyadi, S. E.; Li, T. *J. Phys. Chem. B* **2005,** *109*, 13857−13870.

[6] Charnay, C.; Lee, A.; Man, S.-Q.; Moran, C. E.; Radloff, C.; Bradley, R. K.; Halas, N. J. *J. Phys. Chem. B* **2003,** *107*, 7327−7333.

[7] Skrabalak, S. E.; Au, L.; Li, X.; Xia, Y. *Nat. Protoc.* **2007,** *2*, 2182−2190.

[8] Weissleder, R. *Nat. Biotechnol.* **2001,** *19*, 316−317.

[9] Cho, E. C.; Kim, C.; Zhou, F.; Cobley, C. M.; Song, K. H.; Chen, J.; Li, Z.-Y.; Wang, L. V.; Xia, Y. *J. Phys. Chem. C* **2009,** *113*, 9023−9028.

[10] Hu, M.; Chen, J.; Li, Z.-Y.; Au, L.; Hartland, G. V.; Li, X; Marquez, M.; Xia, Y. *Chem. Soc. Rev.* **2006,** *35*, 1084−1094.

[11] Cobley, C. M.; Chen, J.; Cho, E. C.; Wang, L. V.; Xia, Y. *Chem. Soc. Rev.* **2011,** *40*, 44−56.

[12] Ghosh, P.; Han, G.; De, M.; Kim, C. K.; Rotello, V. M. *Adv. Drug Delivery Rev.* **2008,** *60*, 1307−1315.

[13] Xia, Y.; Li, W.; Cobley, C. M.; Chen, J.; Xia, X.; Zhang, Q.; Yang, M.; Cho, E. C.; Brown, P. K. *Acc. Chem. Res.* **2011,** *44*, 914−924.

[14] Bardhan, R.; Lal, S.; Joshi, A.; Halas, N. J. *Acc. Chem. Res.* **2011,** *44*, 936−946.

[15] Liu, Y.; Welch, M. J. *Bioconjug. Chem.* **2012,** *23*, 671−682.

[16] Guo, Y.; Aweda, T.; Black, K. C.; Liu, Y.; *Curr. Top. Med. Chem.* **2013,** *13*, 470−478.

[17] Anderegg, G.; Arnaud-Neu, F.; Delgado, R.; Felcman, J.; Popov, K. *Pure Appl. Chem.* **2005,** *77*, 1445−1495.

[18] Wadas, T. J.; Wong, E. H.; Weisman, G. R.; Anderson, C. J. *Chem. Rev.* **2010,** *110*, 2858−2902.

[19] Wang, Y.; Liu, Y.; Luehmann, H.; Xia, X.; Brown, P.; Jarreau, C.; Welch, M.; Xia, Y. *ACS Nano* **2012,** *6*, 5880−5888.

[20] Zhao, Y.; Sultan, D.; Detering, L.; Luehmann, H.; Liu, Y. *Nanoscale* **2014,** *6*, 13501−13509.

[21] Zhao, Y.; Sultan, D.; Detering, L.; Cho, S.; Sun, G.; Pierce, R.; Wooley, K. L.; Liu, Y. *Angew. Chem. Int. Ed.* **2014,** *53*, 156−159.

[22] Sun, X.; Huang, X.; Yan, X.; Wang, Y.; Guo, J.; Jacobson, O.; Liu, D.; Szajek, L. P.; Zhu, W.; Niu, G.; Kiesewetter, D. O.; Sun, S.; Chen, X. *ACS Nano* **2014,** *8*, 8438−8446.

[23] Pang, B.; Zhao, Y.; Luehmann, H.; Yang, X.; Detering, L.; You, M.; Zhang, C.; Zhang, L.; Li, Z.-Y.; Ren, Q.; Liu, Y.; Xia, Y. *ACS Nano* **2016,** *10*, 3121−3131.

[24] Black, K. C. L.; Wang, Y.; Luehmann, H. P.; Cai, X.; Xing, W.; Pang, B.; Zhao, Y.; Culter, C. S.; Wang, L. V.; Liu, Y.; Xia, Y. *ACS Nano* **2014,** *8*, 4385−4394.

[25] Sun, X.; Kim, J.; Gilroy, K. D.; Liu, J.; König, T. A.; Qin, D. *ACS Nano* **2016,** *10*, 8019−8025.

[26] Wan, D.; Xia, X.; Wang, Y.; Xia, Y. *Small* **2013,** *9*, 3111−3117.

[27] Skrabalak, S. E.; Chen, J.; Au, L.; Lu, X.; Li, X.; Xia, Y. *Adv. Mater.* **2007,** *19*, 3177−3184.

[28] Li, J.; Zhou, J.; Jiang, T.; Wang, B.; Gu, M.; Petti, L.; Mormile, P. *Phys. Chem. Chem. Phys.* **2014,** *16*, 25601−25608.

[29] Peña-Rodríguez, O.; Caro, M.; Rivera, A.; Olivares, J.; Perlado, J. M.; Caro, A. *Opt. Mater. Express* **2014,** *4*, 403−410.

[30] Zeng, D.; Anderson, C. J. *Chem. Commun.* **2013,** *49*, 2697−2699.

[31] Tentler, J. J.; Tan, A. C.; Weekes, C. D.; Jimeno, A.; Leong, S.; Pitts, T. M.; Arcaroli, J. J.; Messersmith, W. A.; Eckhardt, S. G. *Nat. Rev. Clin. Oncol.* **2012,** *9*, 338−350.

[32] Choi, S. Y. C.; Lin, D.; Gout, P. W.; Collins, C. C.; Xu, Y.; Wang, Y. *Adv. Drug Deliv. Rev.* **2014,** *79−80*, 222−237.

[33] Ding, L. et. al. *Nature* **2010,** *464*, 999−1005.

[34] Li, S. et. al. *Cell Rep.* **2013,** *4*, 1116−1130.

[35] Draine, B. T.; Flatau, P. J. *Opt. Soc. Am. A* **1994,** *11*, 1491−1499.

[36] Johnson, P. B.; Christy, R. W. *Phys. Rev. B* **1972,** *6*, 4370−4379.

[37] Yang, M.; Huo, D.; Gilroy, K. D.; Sun, X.; Sultan, D.; Luehmann, H.; Detering, L.; Li, S.; Qin, D.; Liu, Y.; Xia, Y. *ChemNanoMat* **2017,** *3*,44−50.

CHAPTER 3

CONTROLLING THE DEPOSITION OF PALLADIUM ON GOLD NANOCAGES: OUTER SURFACE ONLY VERSUS BOTH OUTER AND INNER SURFACES

3.1 Introduction

Nobel-metal nanomaterials have found use in a variety of applications, including those related to catalysis [1−3], plasmonics [4−6], and medicine [7−10]. Many different protocols have been developed for the synthesis [10, 11−14], but they can be broadly divided into two major categories--seed-mediated growth *versus* one-pot growth--depending on whether exotic seeds are added or not. Due to the separation of growth from nucleation, seed-mediated synthesis often leads to a much better control over the final products, in terms of size, composition, structures, and morphology [15]. Most of the seeds reported in literature have a solid structure so the atoms can only nucleate and grow from one interface, and major progress has been made in recent years in understanding and controlling the evolution of structures [16−22]. In contrast, there are only a few studies on the use of seeds with hollow interiors and porous walls, as exemplified by Au nanocages [23, 24]. When such particles are applied to seed-mediated growth, both the outer and inner surfaces participate, leading to more complicated products. The resulting particles, characterized by a hollow structure similar to that of the seeds, have recently been reported to hold great promise for applications in catalysis and nanomedicine. For example, the utilization of both outer and inner surfaces offers more flexibility in engineering the active sites for catalysis, in addition to the increase in utilization efficiency for some of the rarest metals on Earth, such as Pt and Ru [3, 25]. Furthermore, the presence of a hollow interior contributes to a higher loading capacity for drugs when these nanomaterials are used for encapsulation and controlled release, while the surrounding metallic walls can provide

additional protection for the payloads during their transition [26, 27]. Taken together, it is well justified to explore the concept of seed-mediated growth using hollow seeds such as Au nanocages. The major challenge in studying such a synthesis can be attributed to the difficulty in differentiating the outer and inner surfaces, in an effort to separately understand the growth behaviors of these two types of surfaces with different dependences on bulk diffusion.

With Au nanocages as a typical example, here I demonstrate that it is feasible to manipulate the pattern of deposition by maneuvering the reduction kinetics of the salt precursor. Specifically, two different Pd(II) precursors, K_2PdCl_4 and K_2PdBr_4, are employed for the synthesis, with the former having a much faster reduction kinetics [28−30]. By taking advantage of the uniformity of the Au nanocages with ultrathin walls and well-defined pores, I am able to resolve minor changes to both the outer and inner edge lengths. This allows us to obtain quantitative information with regard to the thickness of Pd shells deposited on the outer and inner surfaces of the Au nanocages. When the synthesis is conducted using $PdBr_4^{2-}$, I obtain Pd@Au@Pd triple-shell nanocages with Pd being deposited on both the outer and inner surfaces of Au nanocages. The slow reduction of $PdBr_4^{2-}$ ensures adequate time for the precursor ions to access the interior space of a hollow structure through diffusion. In comparison, the deposition of Pd is mainly confined to the outer surfaces of Au nanocages when $PdCl_4^{2-}$ is used, primarily due to its instant reduction to atomic species upon injection into the reaction solution. The Pd atoms tend to collide with the outer surfaces of Au nanocages and be deposited, with essentially no chance to enter the interior through diffusion. This work clearly demonstrates that the reduction rate of a salt precursor can serve as a control knob for manipulating the structure of bimetallic nanocrystal prepared through overgrowth on seeds with hollow interiors and porous walls. This study also offers mechanistic insights into the rational design and facile synthesis of bi- and even multi-metallic hollow nanostructures with well-defined elemental distributions to meet specific requirements for different applications.

3.2 Results and Discussion

Controlling the Deposition Pattern of Pd on Au Nanocages. For the deposition of Pd on Au nanocages, the pattern was found to be largely determined by the type of precursor involved, when all other experimental parameters, including temperature, reductant, solvent, concentrations of precursors and the injection rate, were kept the same. When K_2PdCl_4 was used as a precursor, I obtained Au@Pd double-shell nanocages. In contrast, the products changed to Pd@Au@Pd triple-shell nanocages when K_2PdCl_4 was replaced by K_2PdBr_4. My study clearly demonstrates a strong correlation between the deposition pattern and the reduction kinetics of the Pd(II) precursor.

Figure 3.1 shows a schematic illustration of the two different scenarios of deposition. The upper panel shows the case of $PdCl_4^{2-}$, a precursor that can be quickly reduced by AA in the solution phase. The resulting zero-valence Pd atoms then collide with and nucleate on the outer surface of the Au nanocage. Despite the relatively large (4.7%) mismatch in lattice constants between Pd and Au, conformal deposition was observed for the formation of continuous Pd shells on the outer surfaces of Au nanocages. When switched to $PdBr_4^{2-}$, a salt precursor that could not be easily reduced by AA in the solution phase at room temperature, the ions absorbed onto nanocages, followed by surface-catalyzed reduction. Under such a growth condition, Pd@Au@Pd triple-shell nanocages are obtained as the final products, as illustrated in the lower panel of Figure 3.1.

Figure 3.3a shows a typical TEM image of the Au nanocages used in the current study, which were prepared using a two-step method recently reported by Qin and co-workers [22]. Specifically, an ultrathin layer of Au was first deposited on pre-formed Ag nanocubes, followed by the etching of Ag in the core to generate Au-Ag alloy nanocages. Here I refer them as Au nanocages for simplicity. According to the TEM image, the Au cubic nanocages had an average edge length of 37.4 ± 2.1 nm, an ultrathin wall thickness of around 2.8 nm, as well as characteristic pores at the corner sites. The good uniformity of these nanocages are crucial to this study, in that it enables me to resolve minor changes to their dimensions.

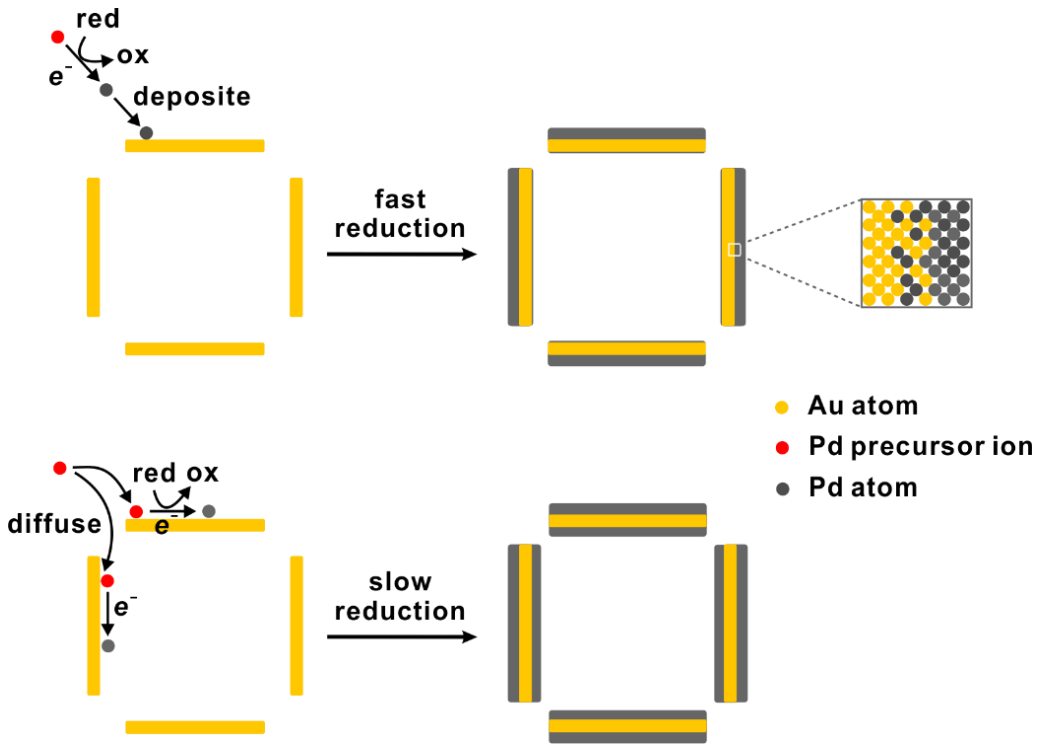

Figure 3.1. Schematic illustration of two different scenarios for the deposition of Pd on the surfaces of Au nanocages with openings at the corners: (top panel) Pd is only deposited on the outer surface and (bottom panel) Pd is deposited on both the outer and inner surfaces. The deposition pattern can be controlled by simply varying the reduction kinetics of the precursor to elemental Pd.

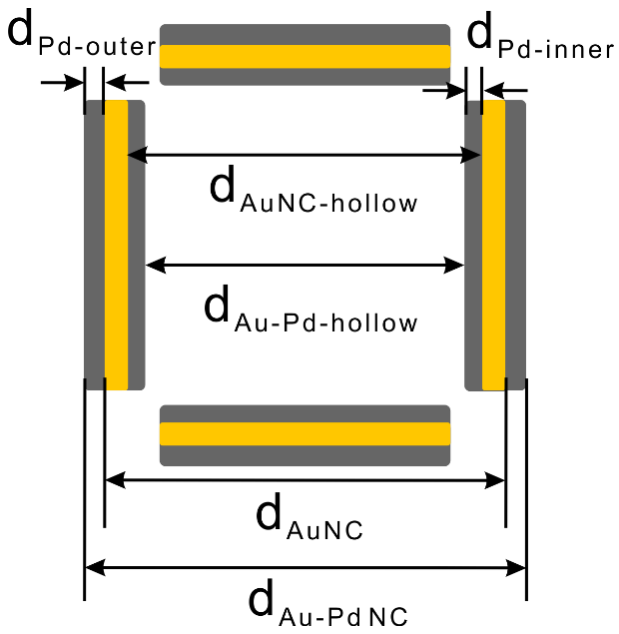

Figure 3.2. Schematic illustration showing that the thickness of Pd shell on the outer surface ($d_{Pd\text{-}outer}$) and inner surface ($d_{Pd\text{-}inner}$) of a Au nanocage could be calculated through the edge length of the Au-Pd nanocage ($d_{Au\text{-}Pd\ NC}$) and pristine Au nanocage (d_{AuNC}), and the dimension of the hollow spaces of these two ($d_{Au\text{-}Pd\text{-}hollow}$ and AuNC-hollow).

Besides, the ultrathin Au walls allow us to resolve the hollow interiors under TEM. The nanocages were then used as seeds for the growth of Au-Pd bimetallic nanostructures through seed-mediated growth. In the first set of experiments, different amounts of aqueous K_2PdCl_4 solution (0.1 mM) were slowly titrated into a suspension containing AA, PVP and Au nanocages using a syringe pump. The final solid products were collected by centrifugation. Figure 3.3b shows a typical TEM image of the sample obtained at a titration volume of 0.75 mL. The morphology of the Au-Pd bimetallic nanocages was identical to that of the original nanocages, including the cubic shape, the well-defined hollow structure, and the openings at corner sites. Compared to the pristine nanocages, a clear increase in wall thickness was observed, because of the deposition of Pd. When I increased the volume of precursor solution to 1.5 mL, Au-Pd nanocages with thicker walls were obtained. Apart from that, the Pd shell became kind of rough on the surface due to the relatively large difference in lattice constants between Pd and Au, as well as insufficient diffusion of Pd atoms when the deposition was conducted at room temperature (25 ^{o}C). To gain a quantitative understanding of the growth process, I carefully measured the overall edge length, wall thickness, and the edge length of the hollow space in the Au-Pd nanocages, by counting 100 individual particles. As expected, the overall edge length of the resulting particles increased to 40.6 ± 1.7 and 42.7 ± 2.0 nm after the injection of 0.75 and 1.5 mL aqueous $PdCl_4^{2-}$, respectively. Taking the dimensions of the original nanocages into consideration, the Pd coating presented on the outer surface of a nanocage was calculated to be 1.6 and 2.7 nm, respectively. On the other hand, the thickness of Pd coating on the inner surface of nanocage could be derived from the reduction in lateral dimensions for the hollow interiors after Pd deposition. According to the TEM images, the average thicknesses of Pd shells deposited on the inner surface were calculated to be 0.2 and 0.4 nm, after the addition of 0.75 and 1.5 mL aqueous K_2PdCl_4, respectively. The wall thickness for the original Au nanocages, as well as the Pd shells deposited on the outer and inner surfaces are summarized in Figure 3.3d. Clearly, majority of the Pd atoms were deposited on the

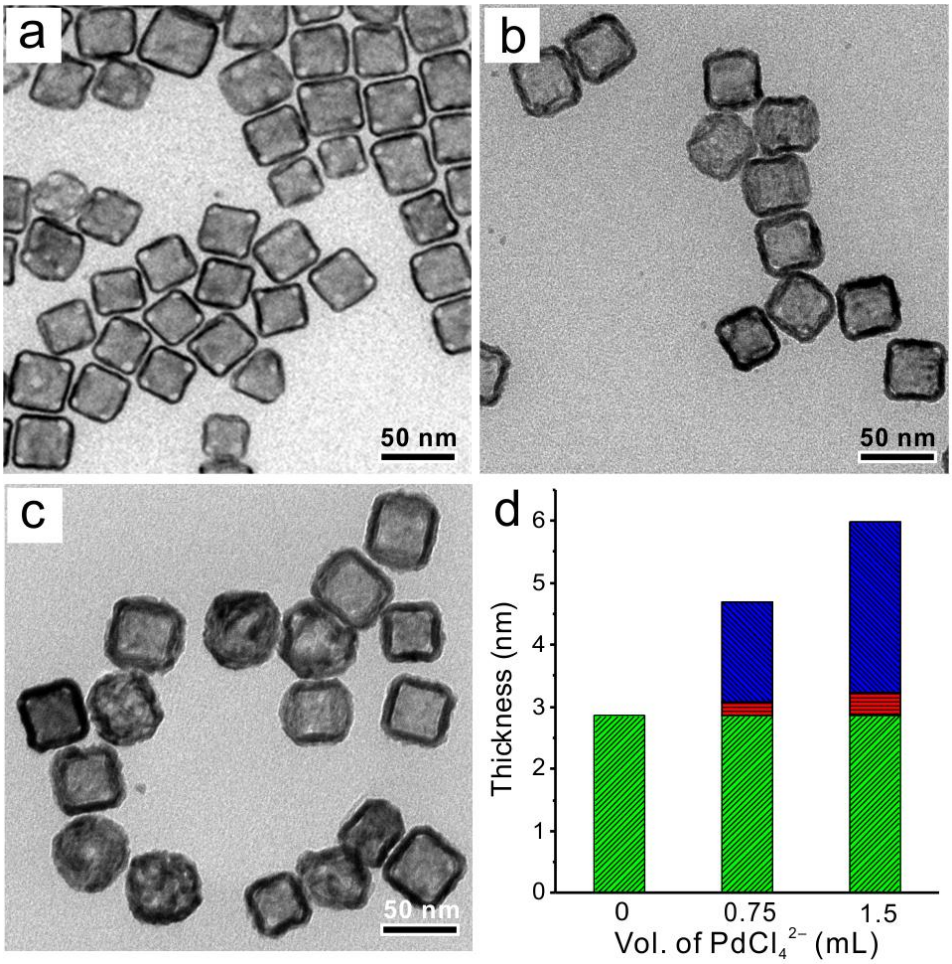

Figure 3.3. TEM images of (a) the Au nanocages and (b, c) Au-Pd nanocages prepared by titrating two different volumes, (b) 0.75 and (c) 1.5 mL, respectively, of aqueous K_2PdCl_4 (0.1 mM) into the suspension of Au nanocages at an injection rate of 0.02 mL/min. (d) The green segments represent the average wall thickness of the pristine Au nanocages while the red and blue segments corresponding to changes to the wall thickness caused by the deposition of Pd onto the inner and outer surfaces of the Au nanocages, respectively.

outer surface of the nanocages, with only negligible growth on the inner surface.

When I changed the precursor to K_2PdBr_4 while keeping all other experimental parameters the same, Au nanocages with Pd shells deposited on both outer and inner surfaces were obtained, as shown in Figure 3.4, a and b. When 0.75 mL of aqueous K_2PdBr_4 (0.1 mM) was introduced, the overall edge length of the resulting nanocages increased to 41.0 ± 2.0 nm, while their hollow interiors decreased from 31.8 nm to 28.7 nm. These numbers correspond to average thicknesses of 1.8 and 1.6 nm, respectively, for the Pd shells deposited on the outer and inner surfaces of the Au nanocages. The comparable thicknesses imply that Pd deposition took place simultaneously on both outer and inner surfaces when $PdBr_4^{2-}$ was used as a precursor. A similar pattern was observed when I increased the volume of aqueous $PdBr_4^{2-}$ from 0.75 to 1.5 mL (Figure 3.4, b and c). At a higher magnification, I could resolve the tri-layer structure of the walls, as shown in Figure 3.4c. The Pd shell showed a lighter contrast compared to the original Au component under TEM imaging because of the difference in atomic numbers for the two elements. Besides, a Moiré pattern could be observed after covering the Au surface with a Pd layer, as illustrated by alternative bright and dark stripes on the particles, due to the superposition of two misfit crystalline lattices associated with Pd and Au [31]. The wall thickness for the original Au nanocages and the Pd shells deposited on the outer and inner surfaces are plotted in Figure 3.3d.

To gain more information on the structure of the resulting Au-Pd nanocages, high-resolution TEM (HRTEM) and high-angle annular dark-field scanning TEM (HAADF-STEM) analyses were performed. The left column in Figure 3.5 shows images of the Au-Pd nanocage obtained using 0.75 mL of $PdCl_4^{2-}$ as the precursor. I can resolve a bi-layer structure mainly comprised of Au and Pd, respectively. The Au nanocage also showed some distortion, together with a wavy structure for the projected outer surface, making them different from the pristine Au nanocages. I believe the internal strain caused by the lattice mismatch between Au and Pd is responsible for this wavy structure, which could be relaxed

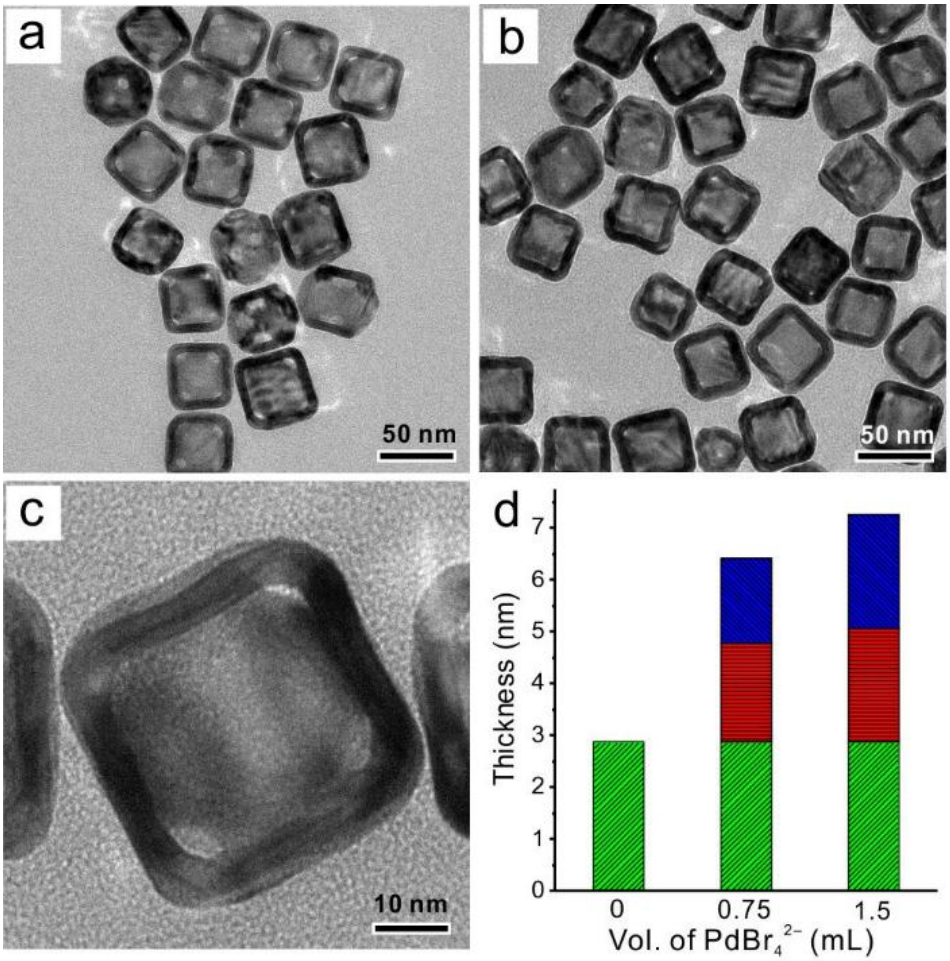

Figure 3.4. (a, b) TEM images of Au-Pd nanocages prepared by titrating two different volumes, (b) 0.75 and (c) 1.5 mL, respectively, of aqueous K_2PdBr_4 (0.1 mM) into the suspension of Au nanocages at an injection rate of 0.02 mL/min. (c) high-magnification TEM image of a typical Au-Pd nanocage as shown in panel (b). (d) The green segments represent the average wall thickness of the pristine Au nanocages while the red and blue segments corresponding to changes to the wall thickness caused by the deposition of Pd onto the inner and outer surfaces of the Au nanocages, respectively.

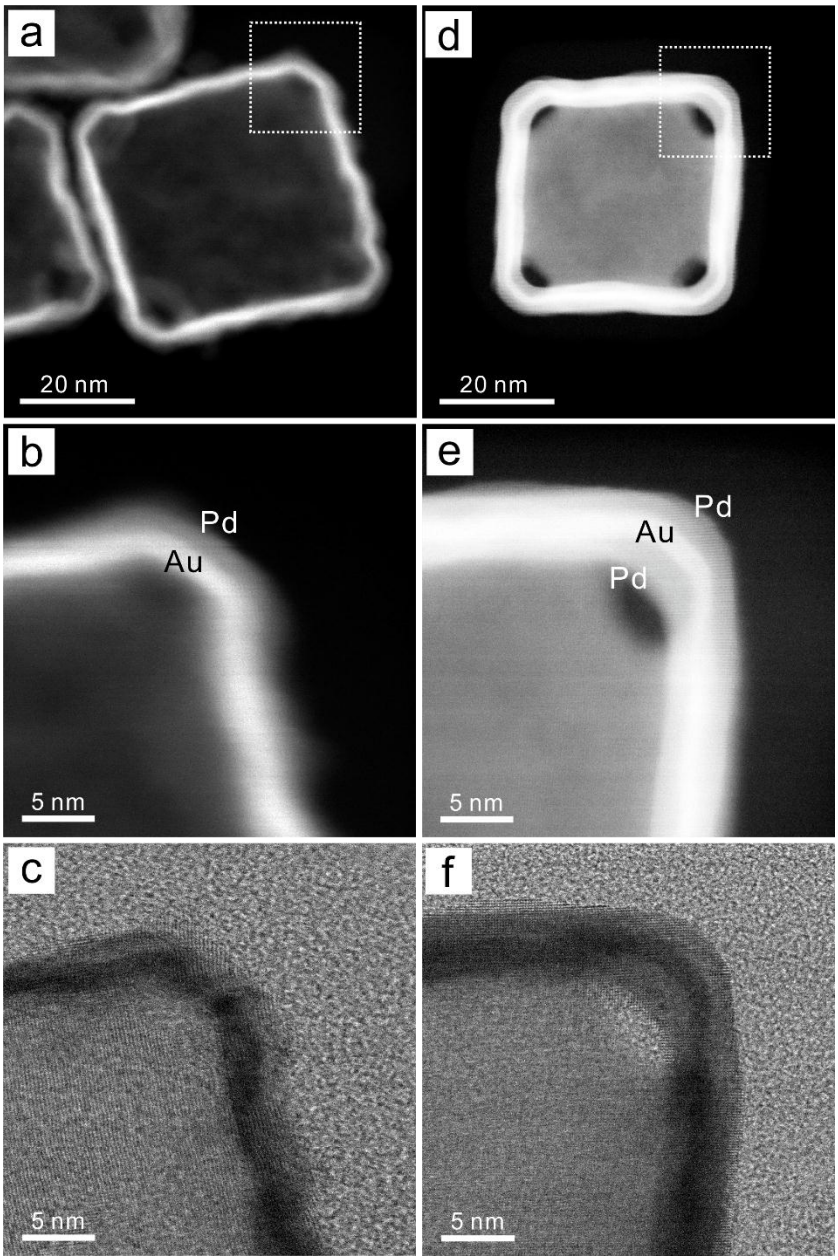

Figure 3.5. (a) HAADF-STEM image of a Au-Pd nanocage prepared using 0.75 mL of K_2PdCl_4. (b) HAADF-STEM image taken from the corner marked by a box in (a), showing Au-Pd bi-layer structure. (c) HR-TEM image of the same corner shown in (a). (d) HAADF-STEM image of a Au-Pd nanocage prepared using 0.75 mL of K_2PdBr_4. (e) HAADF-STEM image taken from the corner marked by a box in (d), showing the Pd-Au-Pd tri-layer structure. (f) HR-TEM image of the same corner shown in (d).

by distorting the ultrathin walls of the nanocages [32].

The right column in Figure 3.5 shows images recorded from the Pd@Au@Pd nanocages obtained with the titration of 0.75 mL of aqueous $PdBr_4^{2-}$. Clearly, the original cubic structure of the Au nanocages, together with hollow interior and well-defined pores, was well-preserved during Pd deposition. Under HAADF-STEM, the Pd walls could be resolved to exhibit two lighter layers alongside each side of the original Au wall, which is brighter in contrast due to the larger atomic number of Au (Figure 3.5e). The thicknesses of the outer and inner Pd layers were estimated to be 1.6 nm and 1.7 nm respectively, in agreement with our previous calculation using TEM images. Importantly, the Pd layers were observed to be smooth, indicating the conformal deposition of Pd under the current experimental conditions. It is worth mentioning that the surface diffusion of the deposited Pd atoms should be relatively slow under the current experimental conditions. Still I was able to evenly coat the entire surface of a Au nanocage with Pd, possibly due to the absence of strong capping agents (such as the Br^- ions commonly used for the synthesis of Pd nanocubes). The tri-layer sandwich structure was also confirmed by HRTEM, as shown in Figure 3.5f.

Optical Properties of the Au-Pd Bimetallic Nanocages. The optical properties of the double-shell and triple-shell Au-Pd bimetallic nanocages were studied by using UV-vis spectroscopy, and the results were summarized in Figure 3.6. The pristine Au nanocages showed a characteristic localized surface plasmon resonance (LSPR) peak at 1065 nm (black curve), because of the hollow structure. After the deposition of a 2.7-nm Pd shell on the outer surface (Figure 3.3c), the LSPR peak changed its shape, showing two board peaks centered at 700 nm and 450 nm (red curve). This change in LSPR peak is due to the damping effect brought by the Pd shell coated on the surface [33]. When PdAu@Pd core-shell structure is formed (Figure 3.4b), the higher electron chemical potential of Pd will make electrons flow from Pd to Au, until an equal electron chemical potential is reached. The increased electron density on Au part will bring a blue shift of its LSPR band [34].

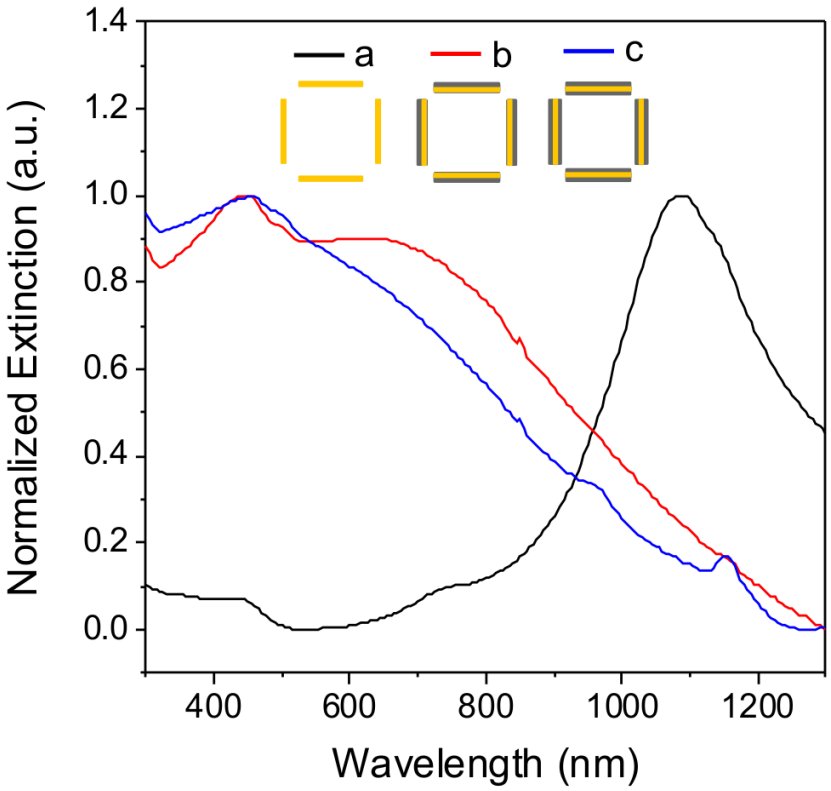

Figure 3.6. UV-Vis spectra recorded from aqueous suspensions of (a) the Au nanocages, (b) the Au-Pd nanocages prepared using 1.5 mL of $PdCl_4^{2-}$ (Figure 3.3c), and (c) Au-Pd nanocages prepared using 1.5 mL of $PdBr_4^{2-}$ (Figure 3.4b),

When Pd layers were formed at both surfaces of Au nanocage, the damping effect was much severe, leaving no observable peak in the UV-vis spectrum (blue curve). This observation is in agreement with the results reported by Xie and co-workers [35].

Mechanistic Investigation of the Formation of Bimetallic Nanocrystals with Distinctive Structures. To gain a better understanding of the transition from single-surface to double-surface deposition, it is necessary to know the reduction rates for the two Pd precursors. In a related study, the reduction kinetics of $PdCl_4^{2-}$ and $PdBr_4^{2-}$ in the presence of solid Pd nanocube seeds have been systematically studied [30]. Taking that identical experimental conditions were used in the current study except for the seed particles, it is not unreasonable to expect that similar reduction kinetics of the two precursors would be followed. The standard reduction potential of $PdCl_4^{2-}$/Pd (0.62 V) is much more positive than that of $PdBr_4^{2-}$/Pd (0.49 V), therefore $PdCl_4^{2-}$ ions are more prone to be reduced. Specifically, $PdCl_4^{2-}$ ions were reduced to atomic species by AA in the solution phase, and its reduction kinetics followed the Finke-Watzky model [36, 37]. The resultant Pd atoms would then undergo heterogeneous nucleation onto Au nanocages due to its lower activation energy compared to their homogeneous nucleation to form Pd particles. In this stage, two possible pathways are involved, *i*) Pd atoms collide and land on the surface of a Au nanocage, leading to Pd shell formation at the outer surface of a seed particle; and *ii*) Pd atoms diffuse through the openings and land on the inner-side of a Au nanocage, resulting in inner-surface deposition. The relative probabilities of each individual pathway are directly proportional to the area ratio of the solid surface to openings on a seed. According to the TEM image shown in Figure 3.3a, I assume that each surface of a Au nanocage is square in shape with 37 nm in edge length, and 4 1/4 round-shaped pores (5 nm in radius) are located at the corners. By calculation, the solid surface contributes over 94% to the total surface area, while the openings only accounts for a small portion (less than 6%). Given this estimation, it is not difficult to understand that Pd atoms will be mainly deposited on the outer surface of a nanocage seed, because of the low possibility

for them to diffuse into the hollow interior.

In the situation of $PdBr_4^{2-}$, its sluggish reduction rate disqualified it from the solution reduction pathway. Instead, the precursor ion will first adsorb on to the surface of a nanocage seed, followed by its reduction through a catalytic process (Figure 3.1, lower panel) [30]. However, the catalyzed reduction of $PdBr_4^{2-}$ is still much slower than that of $PdCl_4^{2-}$. As a result, $PdBr_4^{2-}$ ions will have enough time to diffuse freely into the nanocages, before they are reduced at either outer or inner surface to make the unique Pd@Au@Pd triple-shell sandwich structure. The Pd shells formed under surface reduction were observed to be smooth in structure and evenly distributed over the entire Au surface, because additional time for surface diffusion was provided under such circumstance due to the slow reduction of $PdBr_4^{2-}$. On the contrary, Pd atoms were generated and added to Au surface at a much faster pace in the case of $PdCl_4^{2-}$, cutting the time for their surface diffusion afterwards. Surface reduction of Pd ions also involved in $PdCl_4^{2-}$ case, but contributed much smaller compared to the solution reduction, which explained the unavoidable thin layer of Pd on the inner surface of a nanocage seed when using $PdCl_4^{2-}$ as a precursor.

The difference between the two precursors was much more obvious when I switched their introducing approach from dropwise to one-shot injection. As shown in Figure 3.7, metallic Pd could still be deposited on the nanocages through one-shot injection, but with some variations in the morphology of the final products. Figure 3.7, a and b showed the Au-Pd nanocages obtained by one-shot injecting aqueous K_2PdBr_4 (0.1 mM) with volumes of 0.75 and 1.5 mL into a suspension containing Au nanocages, respectively. Compared to the samples shown in Figure 3.3, b and c, they showed an increased roughness on their surface, which was caused by the faster reduction rate due to the higher precursor concentration upon their immediate injection. The rough surfaces were more obvious when a higher concentration of $PdBr_4^{2-}$ was used, as shown in Figure 3.7b. Under such reduction conditions, self-nucleation was largely kept away from the synthesis, as indicated by the

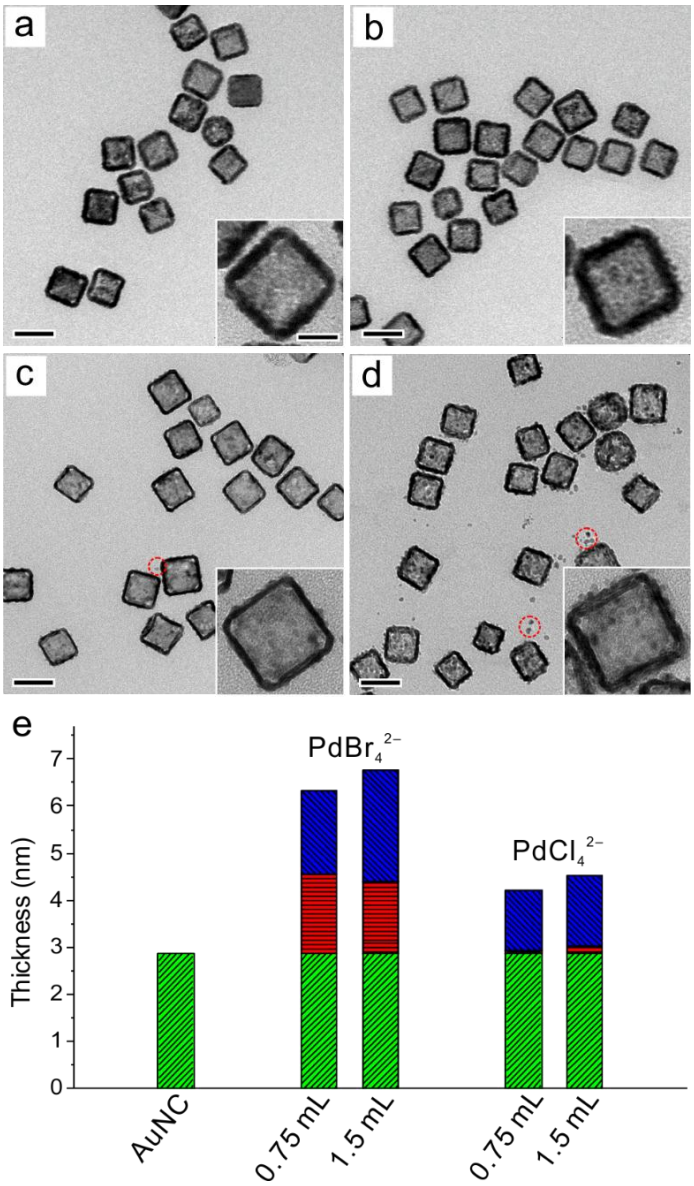

Figure 3.7. (a-d) TEM images of Au-Pd nanocages prepared by injecting various Pd(II) precursors solutions (0.1 mM) into suspensions of Au nanocages in one shot: (a) 0.75 mL aqueous K_2PdBr_4, (b) 1.5 mL aqueous K_2PdBr_4, (c) 0.75 mL aqueous K_2PdCl_4, and (d) 1.5 mL aqueous K_2PdCl_4. All scale bars are 50 nm. The insets show higher magnification images. The scale bar in the inset of (a) is 10 nm and applies to all other insets. The red circles in panels (c) and (d) indicates the Pd nanoparticles formed through homogeneous nucleation due to a fast reduction of precursor ions. (e) Comparison of the thicknesses of Pd layers deposited on the inner (red) and outer surfaces of Au nanocages.

absence of small Pd particles in the final products. This observation suggested that the majority of $PdBr_4^{2-}$ ions were still transformed to atomic species through surface reduction, and thus Pd coatings were expected to form at both sides of a Au seed. This expectation was confirmed by the measurement of the resulting particles by studying the TEM images, which was summarized in Figure 3.7e. It is worthwhile to mention that when $PdBr_4^{2-}$ was one-shot injected into the seed suspension, some precursor ions would eventually undergo solution reduction, due to a relatively fast reduction rate caused by a prompt increase of precursor concentration, especially in the case when higher precursor concentration was used. As a result, I expected a higher ratio of Pd precursors to be deposited on the outer surface of seed particles, compared to the products obtained through dropwise addition. To validate my expectation, the relative thickness ratio of the Pd shell presented on the outer surface of a seed versus that on the inner surface ($d_{Pd\text{-}outer}/d_{Pd\text{-}inner}$) was studied. When 0.75 and 1.5 mL aqueous $PdBr_4^{2-}$ (0.1 mM) was one-shot injected, $d_{Pd\text{-}outer}/d_{Pd\text{-}inner}$ was calculated to be 1.06 and 1.56, respectively, while these numbers dropped to 0.86 and 1.0 in the case of dropwise injection, clearly indicating a higher ratio of Pd deposited on the outer surface through one-shot injection.

On the other hand, when I one-shot injected $PdCl_4^{2-}$ for the synthesis, self-nucleation of Pd atoms took place, as indicated by the small particles circled in Figure 3.7, c and d. The homogeneous nucleation of Pd confirmed the solution reduction of $PdCl_4^{2-}$ ions before they could contact with the seed particles. As a result, Pd shells were mostly formed at the outer surface of the seeds (Figure 3.7e). Due to the consumption of $PdCl_4^{2-}$ by self-nucleation, much thinner Pd shells were observed in one-shot injection experiments (1.3 and 1.5 nm for 0.75 mL and 1.5 mL precursor solution, respectively) compared to that obtained through dropwise injection (1.6 and 2.7 nm). Apart from that, I also observed many particle-like patches on the surfaces of the final products, which was caused by the attachment of self-nucleated Pd particles as well as insufficient surface diffusion of Pd atoms due to their fast reduction rate.

3.3 Conclusion

In summary, I have quantitatively investigated the role of reduction kinetics in controlling the structures of Au-Pd nanocages formed through a seed-mediated growth using Au nanocage seeds. Based on the different reduction rates, Pd precursor ions could be reduced through various pathways. Specifically, a solution phase reduction of $PdCl_4^{2-}$ to Pd atom was observed due to its fast reduction rate, which lead to the formation of Pd shell on the outer surface of a hollow seed. When $PdBr_4^{2-}$ was used as a precursor to Pd, it would first adsorb onto seed particles, followed by the catalytic reduction. In this situation, Pd shells were found to be evenly deposited on both surfaces of a nanocage seed. This work not only greatly advances our understanding of the seed-mediated growth in the case of hollow seeds, but also paves the road for rational design and synthesis of noble-metal nanomaterials with desired structures for various applications.

3.4 Experimental Section

Chemicals and Materials. *L*-ascorbic acid (AA, >99.0%), sodium hydroxide (NaOH, >98%), poly(vinylpyrrolidone) (PVP, $M_W \approx 29{,}000$), hydrogen peroxide (H_2O_2, 30% in H_2O), potassium bromide (KBr, >99.0%), hydrogen tetrachloroaurate trihydrate ($HAuCl_4 \cdot 3H_2O$, >99.9%), potassium tetrachloropalladate (K_2PdCl_4, >99.99%), and potassium tetrabromopalladate (K_2PdBr_4) were all obtained from Sigma-Aldrich (St. Louis, MO). Lauric acid (>97%) was purchased from Spectrum Chemical MFG Corp. (Gardena, CA). All chemicals were used as received. Deionized (DI) water with a resistivity of 18.2 MΩ·cm was used throughout the experiment.

Synthesis of Au Nanocages to Be Used for Seed-mediated Growths. The Au nanocages with an average edge length of 37 nm were prepared using a previously reported method [22]. The final products were dispersed in DI water at a particle concentration of 0.3 nM for future use.

Seed-mediated Growth of Pd on Au Nanocages. In a standard protocol, 0.75 mL of aqueous $PdCl_4^{2-}$ (0.1 mM) or $PdBr_4^{2-}$ (0.1 mM) was titrated into 2 mL of an aqueous suspension containing 43.5 mg of PVP, 8.8 mg of AA, and 0.1 mL of the Au nanocages (0.3 nM in particle concentration) at an injection rate of 0.02 mL/min using a syringe pump. The reaction mixture was hosted in a 20 mL glass vial and held at room temperature for different periods of time to ensure complete reaction. When $PdCl_4^{2-}$ and $PdBr_4^{2-}$ were used as the precursors, the reaction was maintained for 2 h and 6 h, respectively. After reaction, the product was collected by centrifugation at 10,000 rpm for 10 min and washed three times with water.

Measurement of the Thicknesses of Pd Shells Deposited on the Outer and Inner Surfaces of a Au Nanocage. To obtain the thicknesses of Pd shells after deposition, I carefully measured and averaged the edge lengths of 100 individual nanocages on TEM images. The detailed calculation method is illustrated in Figure 3.2 and described below.

The thickness of Pd shell deposited on the outer surface of a Au nanocage is calculated as:

$$d_{Pd\text{-}outer} = 1/2(d_{Au\text{-}Pd\ NC} - d_{AuNC})$$

where $d_{Au\text{-}Pd\ NC}$ is the overall edge length of Au-Pd nanocages after Pd deposition and d_{AuNC} is the overall edge length of the original Au nanocages. The thickness of Pd shell deposited on the inner surface of a Au nanocage is calculated:

$$d_{Pd\text{-}inner} = 1/2(d_{AuNC\text{-}hollow} - d_{Au\text{-}Pd\text{-}hollow})$$

where $d_{AuNC\text{-}hollow}$ and $d_{Au\text{-}Pd\text{-}hollow}$ are the edge lengths of the cubic hollow space inside the Au nanocage before and after Pd deposition.

Instrumentation. Transmission electron microscopy images were taken using a Hitachi HT7700 microscope operated at 120 kV. The samples for TEM analysis were

prepared by drop-casting an aqueous suspension containing the nanoparticles on carbon-coated Cu grids and drying under ambient conditions. UV-vis extinction spectra were recorded using a Perkin-Elmer Lambda 750 UV-vis-NIR spectrometer. High resolution electron microscopy was carried out with an aberration-corrected Hitachi HD-2700 scanning transmission electron microscope operated at 200 kV.

3.5 Notes to Chapter 3

Part of this chapter is adapted from a manuscript entitled "Controlling the Deposition of Pd on Au Nanocages: Outer Surface Only *versus* Both Outer and Inner Surfaces", which was co-authored by me and to be submitted for publication.

3.6 References

[1] Yamada, Y.; Tsung, C. K.; Huang, W.; Huo, Z.; Habas, S. E.; Soejima, T.; Aliaga, C. E.; Somorjai, G. A.; Yang, P. *Nat. Chem.* **2011,** *3*, 372−376.

[2] Wang, X.; Choi, S.; Roling, L. T.; Luo, M.; Ma, C.; Zhang, L.; Chi, M.; Liu, J.; Xie, Z.; Herron, J. A.; Marikakis, M.; Xia, Y. *Nat. Commun.* **2015,** *6*, 7594.

[3] Zhang, L.; Roling, L. T.; Wang, X.; Vara, M.; Chi, M.; Liu, J.; Choi, S.; Park, J. Herron, J. A.; Xie, Z.; Mavrikakis, M.; Xia, Y. *Science* **2015,** *349*, 412−416.

[4] Burda, C.; Chen, X.; Narayanan, R.; El-Sayed, M. A. *Chem. Rev.* **2005,** *105*, 1025−1102.

[5] Rycenga, M.; Cobley, C. M.; Zeng, J.; Li, W.; Moran, C. H.; Zhang, Q.; Qin, D.; Xia, Y. *Chem. Rev.* **2011,** *111*, 3669−3712.

[6] Jones, M. R.; Osberg, K. D.; Macfarlane, R. J.; Langille, M. R.; Mirkin, C. A. *Chem. Rev.* **2011,** *111*, 3736−3827.

[7] Boisselier, E.; Astruc, D. *Chem. Soc. Rev.* **2009,** *38*, 1759−1782.

[8] Dreaden, E. C.; Alkilany, A. M.; Huang, X. H.; Murphy, C. J.; El-Sayed, M. A. *Chem. Soc. Rev.* **2012,** *41*, 2740−2779.

[9] Xia, Y.; Li, W.; Cobley, C. M.; Chen, J.; Xia, X.; Zhang, Q.; Yang, M.; Cho, E. C.; Brown, P. K. *Acc. Chem. Res.* **2011,** *44*, 914−924.

[10] Yang, X.; Yang, M.; Pang, B.; Vara, M.; Xia, Y. *Chem. Rev.* **2015,** *115*, 10410−10488.

[11] Huang, X.; Svetiana, N.; El-Sayed, M. A. *Adv. Mater.* **2009,** *21*, 4880−4910.

[12] Xia, Y.; Xiong, Y.; Lim, B.; Skrabalak, S. E. *Angew. Chem., Int. Ed.* **2009,** *48*, 60−103.

[13] Xia, X.; Wang, Y.; Ruditskiy, A.; Xia, Y. *Adv. Mater.* **2013,** *25*, 6313−6333.

[14] Ruditskiy, A.; Peng, H.-C.; Xia, Y. *Annu. Rev. Chem. Biomol. Eng.* **2016,** *7*, 327−348.

[15] Xia, Y.; Gilroy, K. D.; Peng, H.-C.; Xia, X. *Angew. Chem., Int. Ed.* **2017,** *56*, 60−95

[16] Jana, N. R.; Gearheart, L.; Murphy, C. J. *Chem. Mater.* **2001,** *13*, 2313−2322.

[17] Sun, Y.; Gates, B.; Mayers, B.; Xia, Y. *Nano Lett.* **2002,** *2*, 165−168.

[18] Wiley, B.; Sun, Y.; Mayers, B.; Xia, Y. *Chem. Eur. J.* **2005,** *11*, 454−463.

[19] Habas, S. E.; Lee, H.; Radmilovic, V.; Somorjai, G. A.; Yang, P. *Nat. Mater.* **2007,** *6*, 692−697.

[20] Xie, S.; Lu, N.; Xie, Z.; Wang, J.; Kim, M. J.; Xia, Y. *Angew. Chem., Int. Ed.* **2012,** *51*, 10266−10270.

[21] Xia, X.; Xie, S.; Liu, M.; Peng, H.-C.; Lu, N.; Wang, J.; Kim, M. J.; Xia, Y. *Proc. Natl. Acad. Sci. USA* **2013,** *110*, 6669−6673.

[22] Yang, Y.; Liu, J.; Fu, Z. W.; Qin, D. *J. Am. Chem. Soc.* **2014,** *136*, 8153−8156.

[23] Wan, D.; Xia, X.; Wang, Y.; Xia, Y. *Small* **2013,** *9*, 3111−3117.

[24] Yang, M.; Huo, D.; Gilroy, K. D.; Sun, X.; Sultan, D.; Luehmann, H.; Detering, L.; Li, S.; Qin, D.; Liu, Y.; Xia, Y. *ChemNanoMat* **2017,** *3*, 44−50.

[25] Zhao, M.; Figueroa-Cosme, L.; Elnabawy, A. O.; Vara, M.; Yang, X.; Roling, L. T.; Chi, M.; Mavrikakis, M.; Xia, Y. *Nano Lett.* **2016,** *16*, 5310−5317.

[26] Yavuz, M. S.; Cheng, Y.; Chen, J.; Cobley, C. M.; Zhang, Q.; Rycenga, M.; Xie, J.; Kim, C.; Song, K. H.; Schwartz, A. G.; Wang, L. H. V.; Xia, Y. *Nat. Mater.* **2009,** *8*, 935−939.

[27] Shi, P, Qu, K.; Wang, J.; Li, M.; Ren, J.; Qu, X. *Chem. Commun.* **2012,** *48*, 7640−7642.

[28] Zhang, H.; Jin, M.; Wang, J.; Li, W.; Camargo, P. H. C.; Kim, M. J.; Yang, D.; Xie, Z.; Xia, Y. *J. Am. Chem. Soc.* **2011,** *133*, 6078−6089.

[29] Timoshkin, A. Y.; Kudrev, A. G. *Russ. J. Inorg. Chem.* **2012,** *57*, 1362−1370.

[30] Yang, T.-H.; Peng, H.-C.; Zhou, S.; Lee, C.-T.; Bao, S.; Lee, Y.-H.; Wu, J.-M.; Xia, Y. *Nano Lett.* **2017,** *17*, 334−340.

[31] D. B. Williams, C. B. Carter, *Transmission Electron Microscopy, a Text for Materials Science*, Plenum, New York, **1996**.

[32] Wang, X.; Vara, M.; Luo, M.; Huang, H.; Ruditskiy, A.; Park, J.; Bao, S.; Liu, J.; Howe, J.; Chi, M.; Xie, Z.; Xia, Y. *J. Am. Chem. Soc.* **2015,** *137*, 15036−15042.

[33] Hu, J. W.; Zhang, Y.; Li, J. F.; Ren, B.; Sun, S. G.; Tian, Z. Q. *J. Phys. Chem. C* **2007,** *111*, 1105−1112.

[34] Mulvaney, P.; Giersig, M.; Henglein, A. *J. Phys. Chem.* **1992,** *96*, 10419−10424.

[35] Zhang, K.; Xiang, Y.; Wu, X.; Feng, L.; He, W.; Liu, J.; Zhou, W.; Xie, S. *Langmuir* **2009,** *25*, 1162−1168.

[36] Watzky, M. A.; Finke, R. G. *J. Am. Chem. Soc.* **1997,** *119*, 10382−10400.

[37] Watzky, M. A.; Finney, E. E.; Finke, R. G. *J. Am. Chem. Soc.* **2008,** *130*, 11959−11969.

[38] Moon, G. D.; Choi, S.-W.; Cai, X.; Li, W.; Cho, E. C.; Jeong, U.; Wang, L. V.; Xia, Y. *J. Am. Chem. Soc.* **2011,** *133*, 4762−4765.

CHAPTER 4

SYNTHESIS OF BI- AND TRI-METALLIC NANORATTLES WITH COMPACT SIZES

4.1 Introduction

Gold nanocages have been extensively explored in recent years for biomedical applications, owning to their remarkable optical properties and unique hollow structures [1−3]. As discussed in Chapter 1.2, Au nanocages are typically synthesized through a galvanic replacement reaction between Ag nanocubes and a Au precursor (*e.g.*, $HAuCl_4$), and their size are typically over 30 nm [4]. It has been shown that particle size plays a critical role when used *in vivo*. Previous studies suggested that a smaller particle size should contribute to an improved biodistribution, especially intratumoral distribution, after systemic administration [5, 6]. To prepare Au nanocages with reduced sizes, smaller Ag templates are required, which is hard to obtain through the conventional polyol-based approach, because (*i*) the growth process of Ag nanocubes is hard to terminate due to the intrinsic autocatalytic properties of Ag nanostructures; (*ii*) the corners of small nanocubes are typically truncated because of the oxidative etching of Ag atoms by the oxygen from air; and (*iii*) Ag nanostructures are not in favor of the cubic shape, which is thermodynamically less stable than cuboctahedron. As a result, the smallest Ag nanocubes that can be obtained through a polyol-based method is around 18 nm [7].

Seed-mediated growth provides another approach to the synthesis of Ag nanocubes. With the use of Au-based seeds, smaller Ag nanocubes with edge length of 13 nm could be prepared, thanks to the separation of nucleation from growth [8]. Gold nanocages prepared from such templates contain a core particle (*i.e.*, the seed used for the synthesis of Ag nanocube) and a hollow Au shell, which is also known as nanorattles. The Au cores can be replaced with nanoparticles made of other metals including Pt, Pd, and FePt, bringing additional functions (*e.g.*, catalytic and magnetic) to the nanorattles [9−12]. However, the

conversion of Ag nanocubes with reduced sizes to Au nanorattles remains a challenge. Previous attempts to produce such nanostructures have all failed, which embodied in the deformation or fragmentation of Ag-based templates during their conversion to nanorattles through galvanic replacement [8]. A blue-shift in LSPR always accompanied the structural changes, depriving the resultant nanostructures of optical absorption in the NIR region [7].

Our group recently demonstrated the preparation of Au nanoframes by introducing thin layers of pure Au onto Au nanocages before the dealloying process [13]. The presence of a Au layer served to reinforce the nanostructures and prevented them from collapsing. It is reasonable to argue that a similar approach would also work for the preparation of nanorattles with reduced size. In this work, I demonstrated a general method for the synthesis of M@Au/Ag (M = Au, Pd, and Pt) nanorattles in three major steps: *i*) preparation of M@Ag nanocubes through seed-mediated growth, *ii*) conformal deposition of an ultrathin shell of pure Au on the M@Ag nanocubes, and *iii*) formation of M@Au/Ag nanorattles through galvanic replacement. I was able to produce nanorattles with different metal cores (Au, Pd, and Pt) using Au, Pd, and Pt nanoparticles as the starting materials, respectively. Remarkably, Au@Au/Ag nanorattles with an average edge length as small as 15 nm and ultrathin Au/Ag alloy shells below 2.5 nm thick were obtained, together with a characteristic LSPR peak located in the near infrared (NIR) region. These nanorattles were further demonstrated with excellent photothermal conversion performance, and they were able to effectively eliminate MDA-MB-231 human breast cancer cells under NIR laser irradiation.

4.2 Results and Discussion

The schematic in Figure 4.1 illustrates the structural changes involved in the formation of nanorattles. A typical synthesis includes three major steps. In the first step, M@Ag (M = Au, Pd, and Pt) core-shell nanocubes were prepared through seed-mediated growth using M nanoparticles as the seeds and $AgNO_3$ as a source to elemental Ag by following a

previously reported protocol [8]. With the deposition of Ag atoms onto M seeds, the color of the suspension changed from the original light color (light red for Au seeds and light brown for Pd and Pt seeds) to yellow brown. After collection by centrifugation, ultrathin Au shells were deposited onto the M@Ag nanocubes by reducing $HAuCl_4$ with ascorbic acid (AA) in the presence of NaOH by following a protocol developed by the Qin group at Georgia Tech [14]. The thickness of the Au shell could be controlled by varying the volume

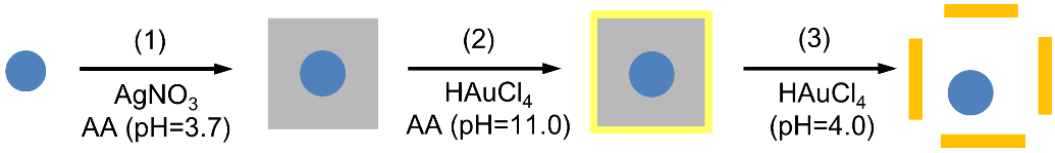

Figure 4.1. A schematic illustration of changes involved in the formation of M@Au/Ag nanorattles. The synthesis involves three major stages: (1) formation of M@Ag core-shell nanocubes via seed-mediated growth using various metal (M = Au, Pd, and Pt) nanoparticle as the seeds; (2) deposition of an ultrathin shell of Au onto the core-shell nanocube by reducing $HAuCl_4$ with ascorbic acid under an alkaline condition; and (3) formation of M@Au/Ag nanorattles *via* galvanic replacement with $HAuCl_4$ [28]. Printed with permission from John Wiley & Sons. Copyright 2017.

of $HAuCl_4$ solution added. After separation from the solution by centrifugation, the M@Ag@Au double-shelled nanocubes were re-dispersed in deionized (DI) water. An aqueous solution of $HAuCl_4$ was added to complete the synthesis through a galvanic reaction. The resulting nanorattle showed a cage-like structure, with a metal core surrounded by a Au/Ag alloy shell.

For the synthesis of nanorattles with Au cores, Au@Ag nanocubes were first prepared using 5.5 nm Au nanospheres as the seeds [8, 15]. The Au seeds were suspended in an aqueous cetyltrimethylammonium chloride (CTAC) solution, followed by the introduction of AA and $AgNO_3$. The reaction mixture was kept at 60 ℃ for 4 h. A typical transmission electron microscopy (TEM) image of the as-obtained Au@Ag nanocubes is shown in Figure 4.2A, which had an average edge length of 13.4 ±0.4 nm. These nanocubes showed a well-defined core-shell structure, displaying a darker Au core and brighter Ag shell due to the difference in atomic number. The nanocubes were slightly truncated at the corners owning to the oxidative etching caused by O_2 and Cl^- ions present in the solution. By varying the volume of $AgNO_3$ solution added during the growth step, the particle size could be well controlled.

To convert the Au@Ag nanocubes into nanorattles, an aqueous solution of $HAuCl_4$ was added directly to initiate a galvanic replacement reaction. However, the LSPR band of the products could not be tuned to the NIR region, with a maximum achievable wavelength at around 620 nm. Further addition of $HAuCl_4$ caused a blue shift to the LSPR peak because of the collapsing of the hollow structure. The blue shift stopped after they had reached 530 nm when more $HAuCl_4$ precursor was added, indicating the formation of solid Au nanoparticles [16]. This structural instability during galvanic reaction is a result of the limited number of Ag atoms contained in each Au@Ag nanocube. For one such particle with an edge length of 13.5 nm, the total number of Ag atoms included is estimated to be around 1.4×10^5. This number is about 27 times smaller than what is contained in a Ag nanocube (3.7×10^6) of 40 nm in edge length (which is commonly used in literature for the preparation of a Au nanocage). During the galvanic reaction, one Au atom will be deposited at the cost of three Ag atoms. As a result, the deposited Au shell would be too thin to support the cage-like structure, leading to the deformation and fragmentation of the resultant nanostructure. The core-shell nature of the template also contributes to the

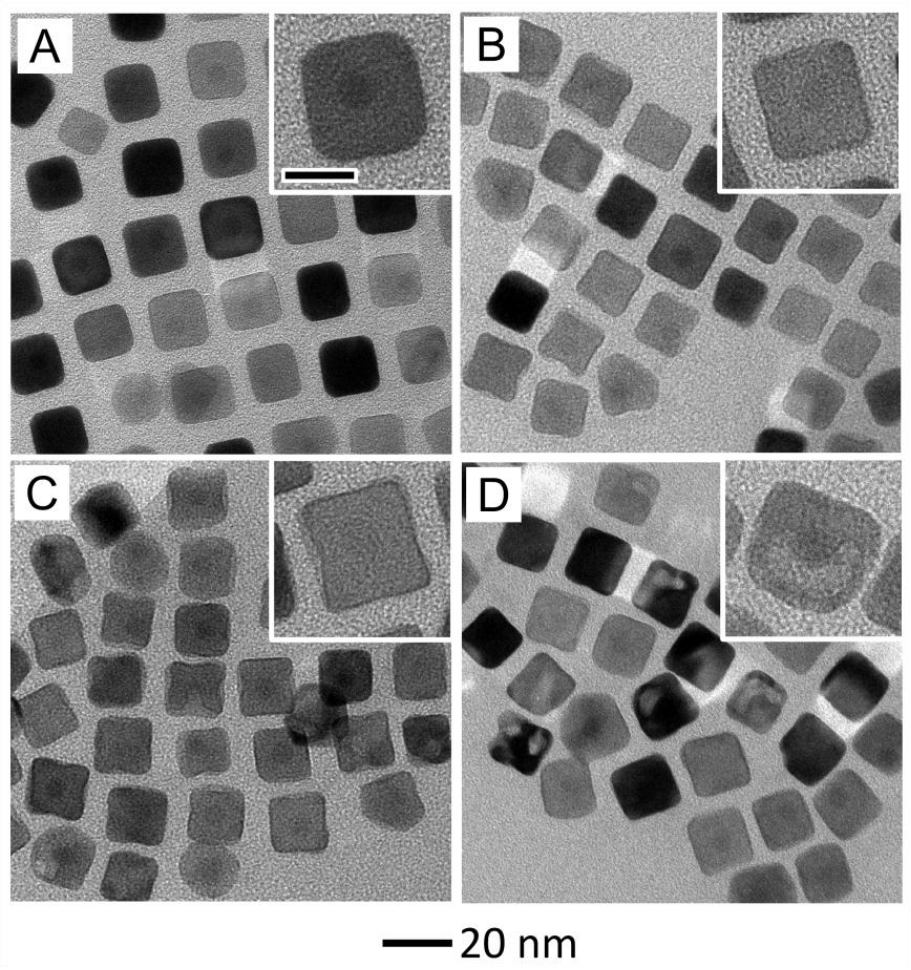

Figure 4.2. TEM images of (A) Au@Ag core-shell nanocubes and (B–D) the corresponding double-shelled nanocubes after the deposition of Au shells with different thicknesses: (B) 0.2, (C) 0.4, and (D) 0.5 nm, respectively (calculated by ICP-MS data), by varying the amount of aqueous $HAuCl_4$ solution (0.1 mM) added: (B) 0.5, (C) 1.0, and (D) 1.5 mL. The scale bar in the inset of (A) is 10 nm and applies to all other insets [28]. Printed with permission from John Wiley & Sons. Copyright 2017.

instability, due to a further reduction in the number of Ag atoms contained in each particle in the presence of a Au core.

To prevent the fragmentation of Au shells during galvanic reaction, an ultrathin layer of pure Au was deposited in advance. The additional Au layer has been reported to effectively improve the physical robustness of fragile nanostructures in the synthesis of Au/Ag alloy nanoframes [13]. Once $HAuCl_4$ was added to a reaction mixture containing Au@Ag nanocubes and AA, Au(III) could be reduced to Au(0) through two parallel pathways, namely, the direct reduction by AA and galvanic replacement involving Ag(0). These two reactions took place simultaneously and competed with each other. As a result, Au/Ag alloy nanocages with enriched Ag contents would be formed [17]. The reducing power of AA will be drastically enhanced when the reaction pH value is increased, which can be used to circumvent the galvanic pathway. Taken together, I deliberately adjusted the pH value of the reaction mixture to 11.2 using aqueous NaOH solution prior to the deposition of Au. However, the pH value of the reaction mixture would inevitably drop with the addition of $HAuCl_4$ due to its acidic nature, which could accelerate galvanic pathway due to the attenuated reducing power of AA, leading to the formation of hollow structures (Figure 4.3). To compensate for the pH drop, an aqueous NaOH solution (40 mM) was co-titrated with aqueous $HAuCl_4$. As shown in Figure 4.4, the pH value of the reaction mixture could be kept above 11.0 throughout the deposition process with the help of additional NaOH. Figure 4.2, B−D shows typical TEM images of the resulting Au@Ag@Au doubled-shelled nanocubes. After the addition of 0.5 mL $HAuCl_4$, I observed a slight increase in edge length for the resultant nanocubes compared to the pristine Ag@Au ones, as well as a dark contrast in their outer walls (Figure 4.2B). These results clearly indicate the formation of an ultrathin Au shell on the outer surface. The double-shelled Au@Ag@Au nanocubes were measured to have an average size of 13.8 ± 0.7 nm, with an ultrathin Au shell calculated to have only one atomic layer in thickness from inductively coupled plasma mass spectroscopy (ICP-MS) measurement (Au accounted for

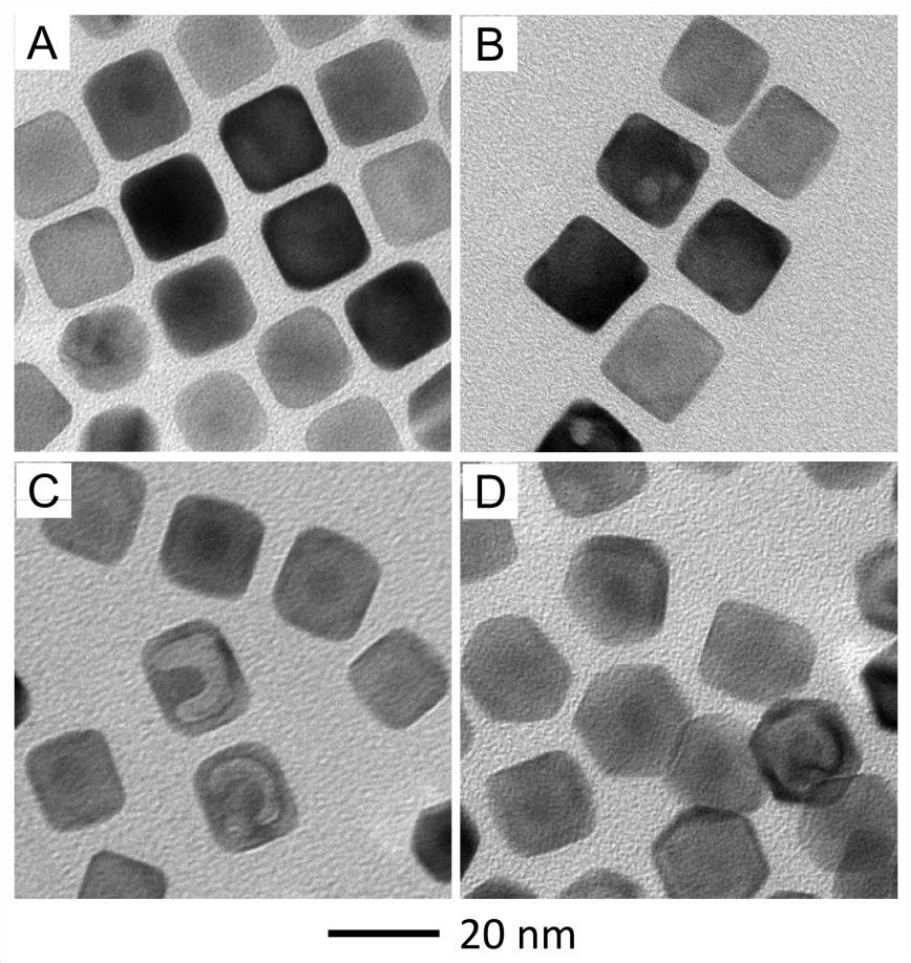

Figure 4.3. TEM images of (A) the Au@Ag nanocubes and (B–D) the corresponding structures after the titration of different volumes of aqueous $HAuCl_4$ (0.1 mM) without introducing NaOH solution to maintain the alkaline pH value: (B) 0.5, (C) 1.0, and (D) 2.0 mL [28]. Printed with permission from John Wiley & Sons. Copyright 2017.

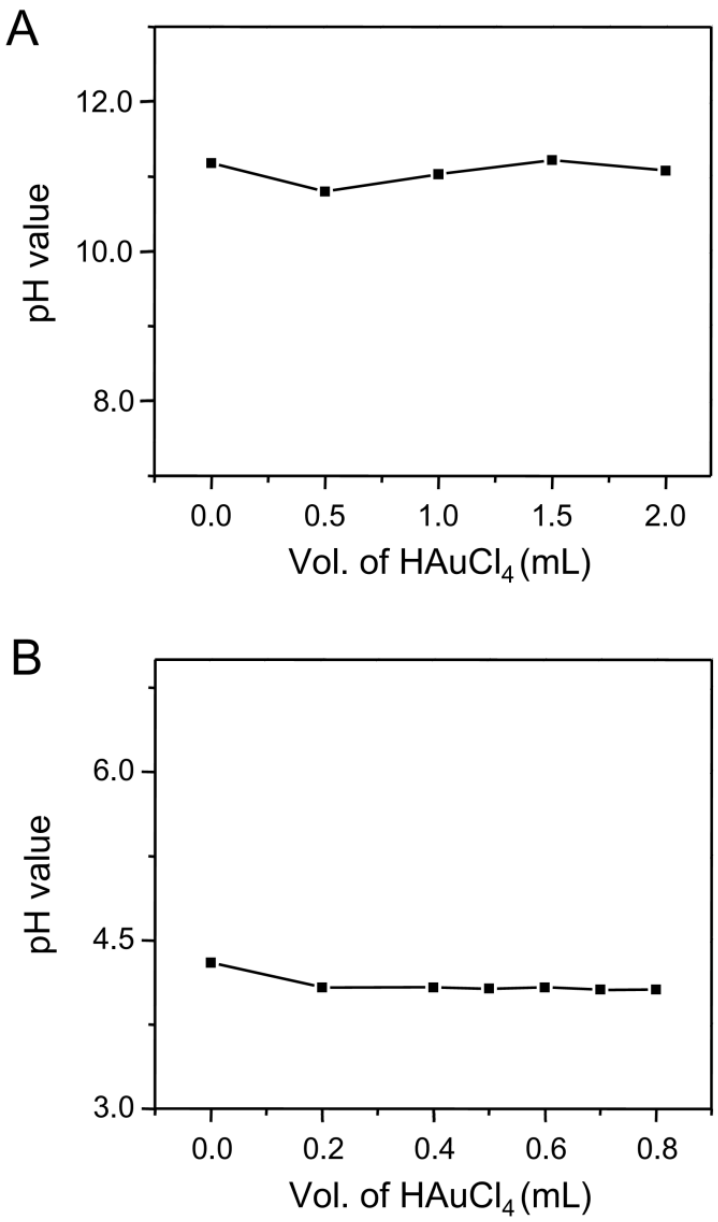

Figure 4.4. Plots of pH value as a function of the volume of aqueous $HAuCl_4$ added during (A) the Au deposition and (B) the galvanic replacement steps, respectively [28]. Printed with permission from John Wiley & Sons. Copyright 2017.

8.6% of the final product). These particles are termed Au@Ag@Au_{1L} for convenience. No void was noticeable under such conditions, suggesting the deposition of Au in a galvanic-free manner.

The thickness of the Au shell continued to increase with the addition of 1.0 mL $HAuCl_4$, with a Au content of 14.9% measured by ICP-MS, which corresponded to about two atomic layers of Au deposited on the surface (Au@Ag@Au_{2L}, Figure 4.2C). In this case, some void spaces showed up on a few of the nanocubes, indicating the occurrence of galvanic replacement. The voids were more obvious when 1.5 mL $HAuCl_4$ solution was added, and the Au content was measured to be around 20%, corresponding to 2–3 atomic layers of Au (Au@Ag@$Au_{2–3L}$, Figure 4.2D). These observations suggest that galvanic replacement reaction could be largely alleviated with a high reaction pH value (>11.00) during the deposition step, but a complete exclusion of such reaction is not possible.

The synthesis of Au@Au/Ag nanorattles was then finalized *via* galvanic replacement between Au@Ag@Au nanocubes and $HAuCl_4$. Figure 4.5 shows typical TEM images of the samples obtained by reacting Au@Ag@Au_{2L} with different amounts of $HAuCl_4$ solution. During the early stage of the reaction, small voids appeared on the side faces of nanocubes (Figure 4.5A), which gradually grew larger in size with the further addition of $HAuCl_4$ solution, producing a clear nanorattle structure (Figure 4.5, B and C). The resultant nanorattles were measured to have an average edge length of 15.6 ± 0.9 nm, as well as ultrathin Au/Ag alloy shells around 2.5 nm. Interestingly, the Au cores were observed to be positioned near the center of most nanorattles. This phenomenon was attributed to the remaining Ag skeleton after galvanic replacement with Au [18]. When excess $HAuCl_4$ was used, the hollow structure would collapse, accompanied by the release of Au cores (Figure 4.5D).

UV-vis spectroscopy was used to monitor the optical properties of the nanostructures during both the Au deposition and galvanic replacement processes. Figure 4.6A shows the UV-vis spectra taken from the pristine Au@Ag nanocubes and double-shelled nanocubes

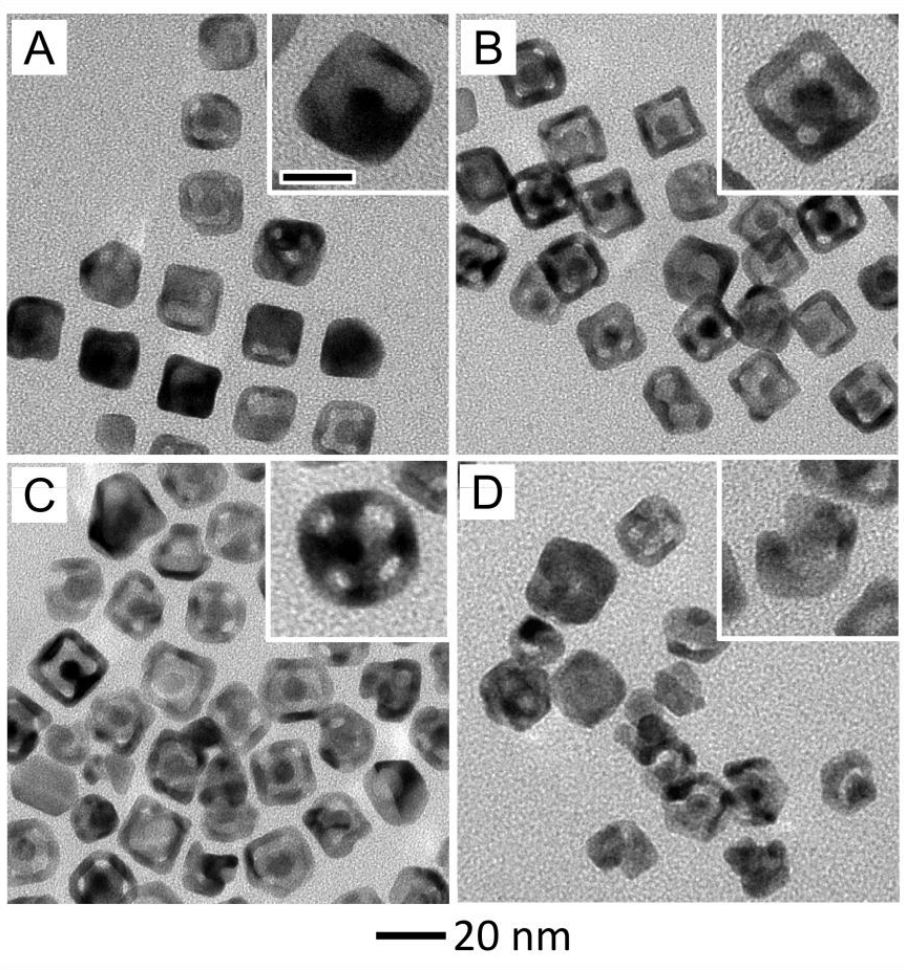

Figure 4.5. TEM images of the Au@Au/Ag nanorattles synthesized by reacting Au@Ag@Au_{2L} (shown in Figure 4.2C) with different volumes of $HAuCl_4$ solution (0.1 mM): (A) 0.2; (B) 0.4; (C) 0.6 and (D) 0.8 mL. The scale bar in the inset of (A) is 10 nm and applies to all other insets [28]. Printed with permission from John Wiley & Sons. Copyright 2017.

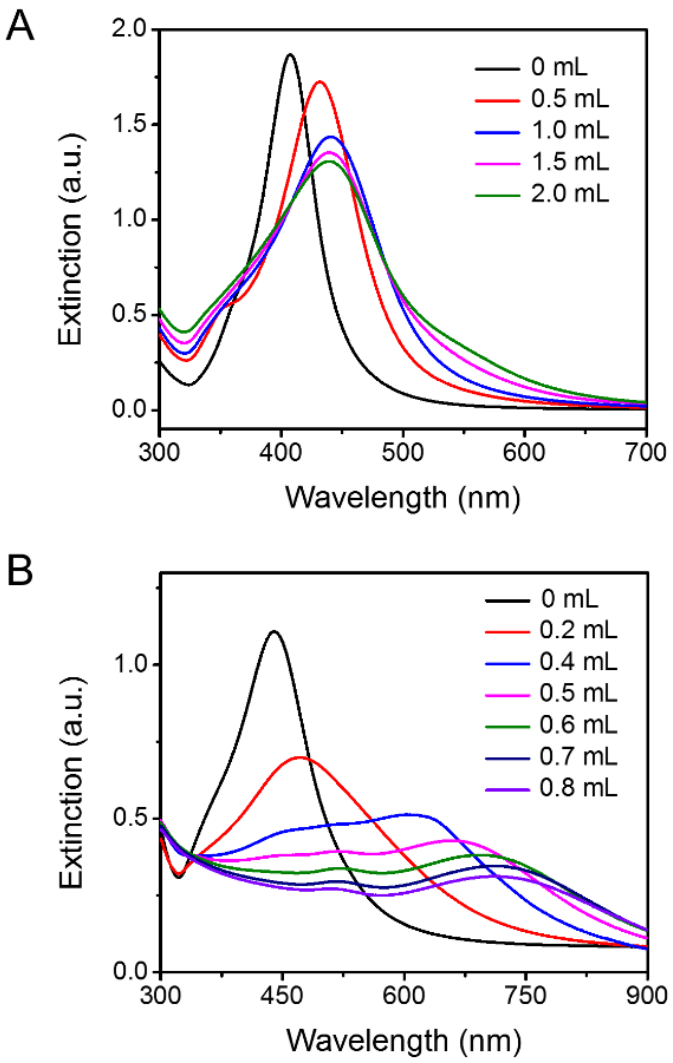

Figure 4.6. (A) UV-vis spectra taken from aqueous suspensions of the double-shelled nanocubes synthesized by reducing different volumes of $HAuCl_4$ solution (0.1 mM) with AA under an alkaline condition as shown in Figure 4.2. (B) UV-vis spectra taken from the galvanic replacement reaction between Au@Ag@Au_{2L} and different volumes of $HAuCl_4$ solution (0.1 mM) as shown in Figure 4.5 [28]. Printed with permission from John Wiley & Sons. Copyright 2017.

with ultrathin Au shells prepared with the introduction of different volumes of $HAuCl_4$ solution (0.1 mM) under an alkaline condition. A slight red shift for the LSPR peak from 405 nm to 420 nm was noticed after the initial addition of 0.5 mL $HAuCl_4$ solution, together with a negligible broadening in peak width. This observation was in agreement with the literature report [14], suggesting the formation of Au shells in a galvanic-free manner. Introducing more $HAuCl_4$ solution would bring a further red shift to the LSPR peak, with an obvious broadening of the peak width, which can be attributed to the change of the dielectric constants [19], and the presence of small voids in the doubled-shelled nanocubes [17].

Much pronounced changes to LSPR peaks were observed during the galvanic replacement step, as shown in Figure 4.6B, when Au@Ag@Au_{2L} were used as sacrificial templates. A distinct red shift of the LSPR peak into the NIR region was noticed due to the hollowing of the nanocubes, and a wavelength of 725 nm was reached when 0.8 mL of $HAuCl_4$ solution was added. The peak intensity dropped during the titration process, as the shells of the resultant nanostructures became thinner and more porous [20]. An excess amount of $HAuCl_4$ resulted in a blue-shift to the LSPR peak, due to the collapsing of the nanorattles. Besides the major LSPR peak that kept shifting throughout the reaction, the Au@Au/Ag nanotattles had another peak positioned at around 518 nm, which can be attributed to the Au cores. For a nanosphere made of pure Au, its LSPR peak is positioned at around 525 nm, and the blue-shift of the peak position observed in this study indicates the presence of residual Ag on the Au core [21]. Discrete dipole approximation (DDA) has also been applied to calculate the extinction spectra of Au@Ag nanocubes, Au@Ag@Au double-shelled nanocubes, and Au@Au/Ag nanorattles. The simulation results were summarized in Figure 4.7 and the peak positions were in reasonable agreement with our experimental results. A similar trend was observed in the case of Au@Ag@$Au_{2–3L}$, with the LSPR peak tunable from 435 to 705 nm (Figure 4.8B) during the reaction. The

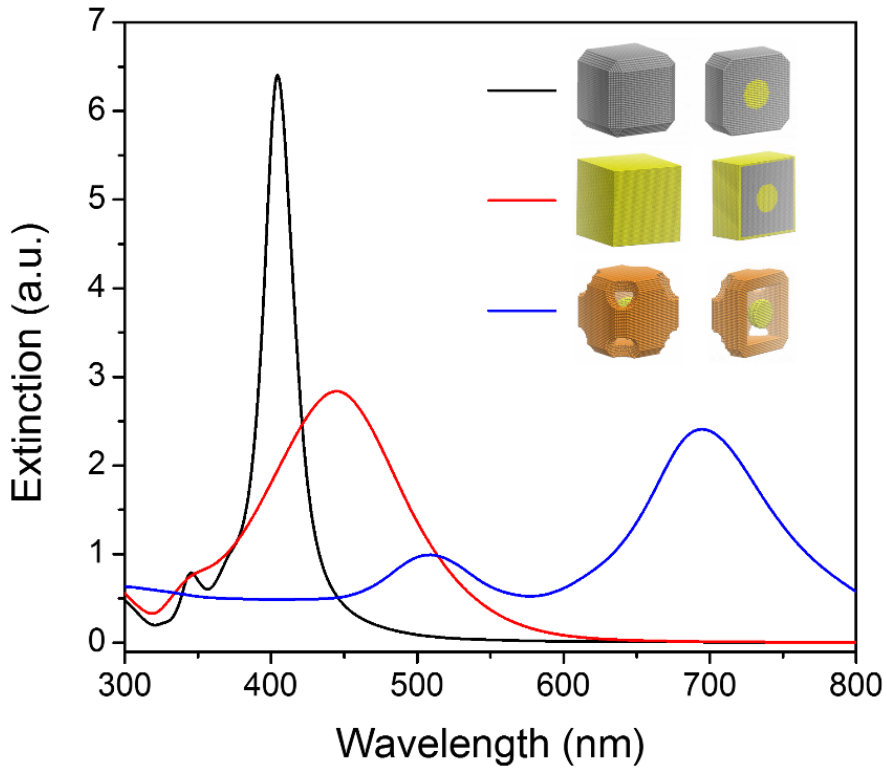

Figure 4.7. Extinction spectra calculated for Au@Ag nanocubes (black), Au@Ag@Au double-shell nanocubes (red), and Au@Au/Ag nanorattles (blue) using the DDA method [28]. Printed with permission from John Wiley & Sons. Copyright 2017.

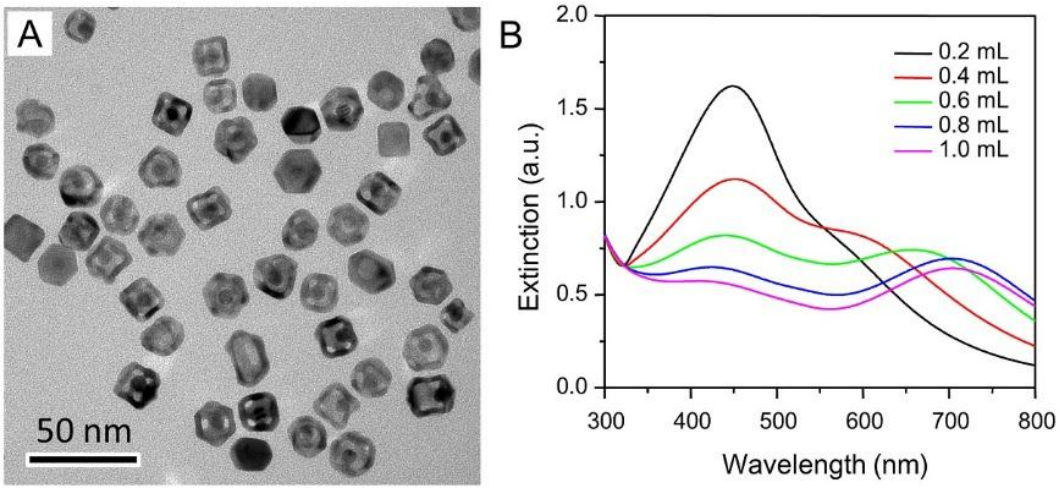

Figure 4.8. (A) TEM images of Au@Au/Ag nanorattles obtained after titrating 0.8 mL of aqueous $HAuCl_4$ (0.1 mM) into a suspension of $Au@Ag@Au_{2–3L}$ and (B) the corresponding UV-vis spectra recorded during the titration process [28]. Printed with permission from John Wiley & Sons. Copyright 2017.

maximum tunable wavelength of the LSPR peak is closely related to the wall thickness of the nanorattles, which was demonstrated experimentally here and theoretically in previous report [13]. Taken together, it is clear that the thickness of the Au shell deposited on the Ag@Au nanocube serves a critical role in manipulating the properties of the nanorattles: *i*) a thicker Au shell better reinforces the nanorattles; and *ii*) a thinner Au shell facilitates the red-shift of the LSPR peak into the NIR region. Based on the specific requirements of different applications, a tradeoff has to be made between the physical stability and the LSPR peak position when a proper thickness of the deposited Au shell is selected for the synthesis of Au@Au/Ag nanorattles.

The elemental compositions (Au and Ag) of the nanostructures involved in this study were also analyzed using ICP-MS (Figure 4.9). For $Au@Ag@Au_{1L}$, the mole percent of

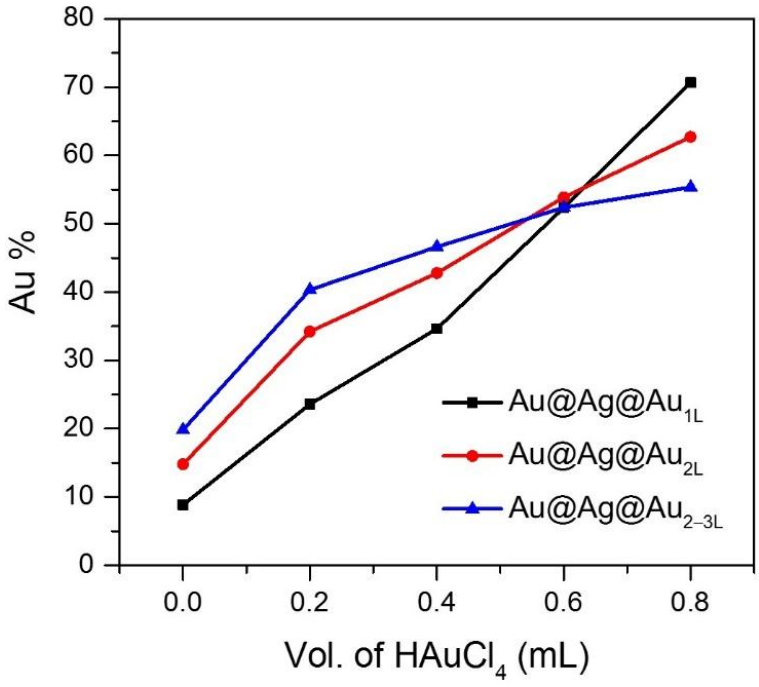

Figure 4.9. The mole percent of Au in the resultant nanostructures when different volumes of aqueous $HAuCl_4$ (0.1 mM) were titrated into suspensions of $Au@Ag@Au_{1L}$ (black), $Au@Ag@Au_{2L}$ (red) and $Au@Ag@Au_{2–3L}$ (blue), respectively [28]. Printed with permission from John Wiley & Sons. Copyright 2017.

Au was measured to be 8.6% prior to the galvanic replacement reaction. This Au amount corresponded to an average shell thickness of 0.2 nm, assuming the deposition of Au was conformal and uniform, and it was in reasonable agreement with the dimension change of the nanocubes before and after deposition measured by TEM image. The content of Au increased with the addition of $HAuCl_4$, due to the galvanic replacement between Au(III) and Ag(0). After 0.8 mL of $HAuCl_4$ solution had been titrated, the resultant nanorattles showed a Au content of 70.7%, which was similar to the value report for Au/Ag alloy nanocages [22], confirming the alloy nature of the products. For the nanorattles derived from the $Au@Ag@Au_{2L}$ and $Au@Ag@Au_{2–3L}$, less Au was observed, with its contents

being 62.7% and 55.4%, respectively. The results indicated that Ag atoms in these nanostructures were less reactive towards Au, due to the presence of a thicker shells. This trend was confirmed by the UV-vis spectrum, in which a clear Ag peak was observed around 420 nm after Au titration in the presence of a thicker Au shell (Figure 4.8B).

I also sought to extend the synthesis to other type of nanorattles, with the cores made of Pd and Pt. By simply replacing the Au spherical seeds with Pd or Pt seeds, Pd@Ag and Pt@Ag nanocubes were successfully prepared, which were then converted to Pd@Au/Ag and Pt@Au/Ag nanorttles using the same protocol (Figure 4.10). The results clearly indicated that the three-stage approach is kind of general for the synthesis of nanorattles with different metal cores.

I then evaluated the photothermal property of the 15-nm Au@Au/Ag nanorattles. The nanorattles were dispersed in 1.0 mL of DI water at a Au concentration of 20 μg mL^{-1}, and irradiated with 808 nm laser at 0.25, 0.5 and 1 W cm^{-2} up to 5 min. Pure water without nanorattles was used as a reference. An IR camera was used to monitor the temperature change during the irradiation. The temperatures of all the suspensions containing nanorattles rose with increasing irradiation time (Figure 4.11E). After irradiation at a power density of 1 W cm^{-2} for 5 min, the suspension showed a temperature increase of 33.1 ℃ while the pure water only showed an increase of 3.2 ºC. According to these data, I calculated the energy conversion efficiency (η) of the Au@Au/Ag nanorattles, which was defined by comparing the total heat (Q) generated in the solution with the total energy output (E) of the laser [23].

$$\eta = Q/E \tag{4.1}$$

$$Q = C_p m \Delta T = C_p \rho V \Delta T \tag{4.2}$$

$$E = PSt \tag{4.3}$$

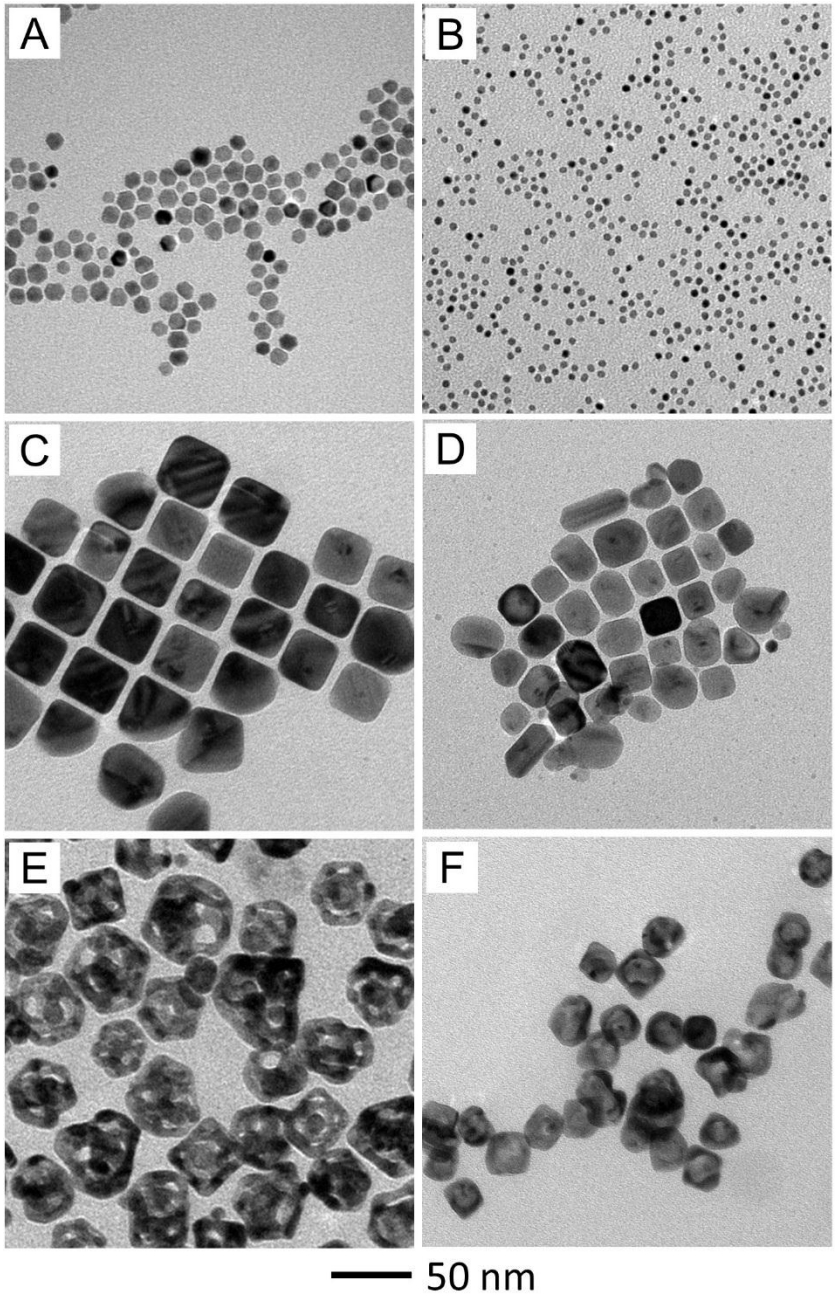

Figure 4.10. TEM images of (A) the 8-nm Pd cuboctahedral seeds, (C) Pd@Ag nanocubes, and (E) Pd@Au/Ag nanorattles; (B) the 3-nm Pt spherical seeds, (D) Pt@Ag nanocubes, and (F) Pt@Au/Ag nanorattles [28]. Printed with permission from John Wiley & Sons. Copyright 2017.

Here C_p is the specific heat of water (4.18 J g^{-1} K^{-1}), m is the mass of the solution, ρ is the density of water, V is the volume of the solution, P is the power density of the laser (1.0 W cm^{-2}), S is the irradiation area (1.13 cm^2) and t is the irradiation time. The η value was determined to be 40.7% for nanorattles with a Au concentration of 20 μg mL^{-1}, comparative to that of the commonly used Au nanocages (63.6%) of 45 nm in size and larger than 17 nm nanorods with an aspect ratio of 3.3 (22.1%) and hexapods with an average edge length of 25 nm (29.6%) with similar Au mass [23].

Finally, I evaluated the feasibility of using the 15-nm Au@Au/Ag nanorattles as a photothermal therapeutic agent, with MDA-MB-231 cells serving as a model system (Figure 4.11, A–D). The cells were incubated with the nanorattles for 4 h, followed by exposure to a diode laser (808 nm) for 5 min at energy densities of 0.25, 0.5 and 1 W cm^{-2}, respectively. After irradiation, the cells were stained with both calcein AM and red fluorescent reactive dyes. Under fluorescence microscopy, a clear demarcation line was observed between the live cells (green) and dead cells (red), and the dead cells were mostly located within the laser spot. In contrast, the cells treated with nanorattles or laser irradiation alone did not show obvious cell death. These results indicated that the Au@Au/Ag nanorattles could be used to effectively kill the cells through the photothermal effect induced by NIR irradiation. The photothermal cytotoxicity of the nanorattles was also quantified on cancer cells using the MTT assay (Figure 4.11F). After incubation with nanorattles for 4 h, the cell viability was not affected and remained at approximately 90%. However, under laser irradiation, the cell viability decreased dramatically with the increasing laser power, and less than 10% of the cells remained alive at a laser power of 1 W cm^{-2}. These results suggest that Au@Au/Ag nanorattles hold great promise as an effective transducer for photothermal therapy.

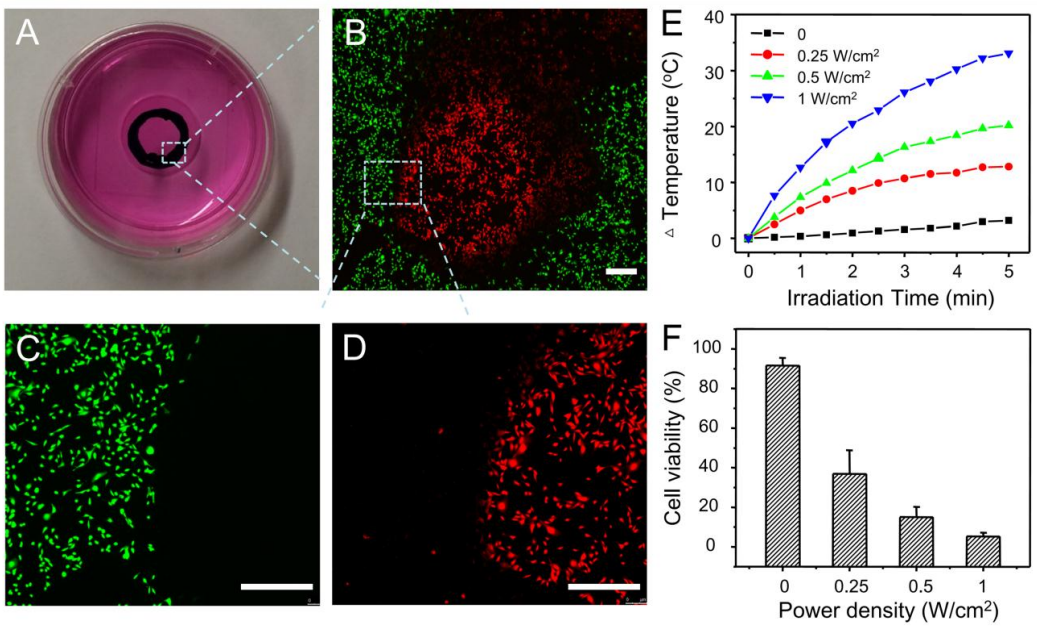

Figure 4.11. (A) Digital photo of MDA-MB-231 cell culture dish after incubation with the 15-nm Au@Au/Ag nanorattles. The black circle indicates the laser spot. (B–D) Fluorescence images of calcein AM (green, live cells) and red fluorescence dye (red, dead cells) co-stained MDA-MB-231 cells after laser irradiation. (E) Temperature elevation of water and nanorattle suspensions as a function of laser power. (F) Cell viability of MDA-MB-231 cells treated with nanorattles and 808 nm laser irradiation for 5 min with different power densities (0.25, 0.5 and 1 W cm^{-2}). The scale bars are 500 μm [28]. Printed with permission from John Wiley & Sons. Copyright 2017.

4.3 Conclusion

In summary, I have demonstrated a general method for the facile synthesis of M@Au/Ag (M = Au, Pd and Pt) nanorattles. The preparation can be divided into three major steps, including the formation of M@Ag nanocubes *via* seed-mediated growth method, conformal deposition of an ultrathin thin Au shell, and formation of nanorattles through galvanic replacement. The presence of ultrathin Au shells (only a few atomic layers thick) on the M@Ag nanocubes prior to the galvanic replacement reaction effectively enhanced their structural robustness, ensuring the successful preparation of nanorattles. As a typical example, I prepared Au@Au/Ag nanorattles with an overall dimension of 15 nm and a wall thickness around 2.5 nm. Significantly, their optical properties could be tuned to resemble those of Au nanocages with much larger dimensions and thick walls. The nanorattles showed NIR absorption and excellent photothermal conversion efficiency. They were capable of effectively killing cancer cells upon irradiation with a NIR laser, suggesting their great potential as effective photothermal transducers for cancer diagnostics and therapeutics.

4.4 Experimental Section

Chemicals and Materials. Ethylene glycol was purchased from J. T. Baker. *L*-ascorbic acid (>99.0%), sodium hydroxide (NaOH, >98%), sodium borohydride ($NaBH_4$, >99%), poly(vinylpyrrolidone) ($M_W \approx 55{,}000$), hexadecyltrimethylammonium bromide (CTAB, >99%), cetyltrimethylammonium chloride (CTAC, ~25% in H_2O), hydrogen tetrachloroaurate trihydrate ($HAuCl_4\ 3H_2O$, >99.9%), silver nitrate ($AgNO_3$, >99%), potassium tetrachloroplatinate (K_2PtCl_4, >99.9%), sodium tetrachloropalladate (Na_2PdCl_4, >99.99%) and 3-(4,5-dimethylthiazol-2-thiazolyl)-2,5-diphenyl-2H-tetrazolium bromide (MTT) were all obtained from Sigma-Aldrich (St. Louis, MO). Methoxy polyethylene glycol thiol ($M_W \approx 2{,}000$) was purchased from Laysan Bio

(Arab, AL). All chemicals were used as received. Calcein-AM cell-permeant dye was purchased from Invitrogen. Deionized (DI) water with a resistivity of 18.2 MΩ·cm was used throughout the experiment.

Synthesis of Au spherical seeds. The Au spherical seeds of 5.5 nm in diameter were prepared using a two-step procedure [22]. In the first step, Au nanospheres of 3 nm in size were prepared by adding 0.6 mL of ice-cooled aqueous $NaBH_4$ (10 mM) into 10 mL of another aqueous solution containing $HAuCl_4$ (0.25 mM) and CTAB (100 mM). Upon adding $NaBH_4$, the solution showed a brownish color, and this solution was left undisturbed at 30 ℃ for 3 h to ensure the complete decomposition of $NaBH_4$. To synthesize the CTAC-capped Au nanospheres, 2 mL of aqueous $HAuCl_4$ (0.5 mM), 2 mL of aqueous CTAC (200 mM) and 1.5 mL of aqueous AA (100 mM) were mixed in a 20 mL vial, followed by the introduction of 0.7 mL of the 3-nm Au nanoparticles. The reaction mixture quickly turned red, indicating the formation of larger Au nanoparticles. The mixture was kept undisturbed at room temperature for 30 min. The solid products were collected by centrifugation at 55000 rpm for 45 min and re-dispersed in 1.0 mL of DI water.

Synthesis of Pd cuboctahedral seeds. The Pd seeds of 9 nm in size were synthesized by following a reported protocol [24]. Typically, 8.0 mL of an aqueous solution containing 50 mg PVP, 60 mg AA, and 188 mg KCl was added into a 20 mL vial and heated at 80 ℃ under magnetic stirring for 10 min. Afterwards, 3.0 mL of an aqueous solution containing 57 mg Na_2PdCl_4 was introduced. The reaction was kept at 80 ℃ for 3 h. The solid products were collected through centrifugation, washed three times with DI water, and finally re-dispersed in 11 mL of DI water.

Synthesis of Pt spherical seeds. The Pt spherical seeds of 3 nm in diameter were prepared by injecting a solution of K_2PtCl_4 in EG into another solution of PVP and AA in EG with a pipet. In a typical synthesis, 50 mg of PVP, 50 mg of AA, and 7 mL of EG were mixed in a 20 mL vial at room temperature (22 ℃) under magnetic stirring for 10 min. Meanwhile, 14.2 mg of K_2PtCl_4 was dissolved in 3 mL EG and the solution was

subsequently added and kept under magnetic stirring for another 10 min at room temperature. The mixture was then heated in an oil bath at 160 ℃ for 3 h and allowed to naturally cool down to room temperature. The product was collected by centrifugation, washed once with acetone and twice with DI water, and finally re-dispersed in 10 mL of DI water.

Synthesis of M@Ag nanocubes (M = Au, Pd, and Pt). The M@Ag nanocubes were synthesized through seed-mediated growth by following the reported protocol [18]. In the case of Au@Ag, 0.3 mL of the Au spherical seeds were added to a round-bottom flask containing 15 mL aqueous CTAC solution (20 mM), and the mixture was heated at 60 ℃ for 20 min under magnetic stirring. Afterwards, 1.0 mL of aqueous AA (100 mM) was added, followed by the dropwise addition of 2.4 mL of aqueous $AgNO_3$ (2 mM) at a rate of 1 mL min^{-1} using a syringe pump. The reaction mixture turned from light red to yellow brown after the injection of $AgNO_3$, and it was kept at 60 ℃ for 4 h. Finally, the flask was cooled in an ice-bath and the resultant Au@Ag nanocubes were collected by centrifugation at 22,000 rpm for 15 min and then washed once with water. The size of the nanocubes could be controlled by varying the amount of $AgNO_3$ solution added. For Pd@Ag and Pt@Ag nanocubes, they were synthesized using a similar protocol by introducing 20 μL of the Pd spherical seeds and 5 μL of the Pt spherical seeds, respectively.

Synthesis of M@Ag@Au nanocubes (M = Au, Pd, and Pt). The M@Ag@Au nanocubes were synthesized by depositing Au onto M@Ag nanocubes using AA as a reducing agent under the alkaline condition [14]. In the case of Au@Ag@Au, 3 mL of aqueous PVP (1 mM) was mixed with 1 mL of aqueous CTAC (200 mM) in a 20 mL glass vial, to which 0.5 mL of aqueous AA (20 mM) and 0.2 mL of aqueous NaOH (200 mM) were added, followed by 0.5 mL of the suspension of Au@Ag nanocubes under magnetic stirring. Afterwards, 2 mL of aqueous $HAuCl_4$ (0.1 mM) was injected at a rate of 0.02 mL min^{-1} using a syringe pump. Simultaneously, 1 mL of aqueous NaOH (40 mM) was titrated at 0.01 mL min^{-1} to maintain the alkaline pH value. After reacting for 15 min, the solid

products were collected by centrifugation at 22,000 rpm for 15 min and washed once with DI water. The Au@Ag@Au nanocubes were re-dispersed in 0.5 mL DI water for future use. For Pd@Ag@Au and Pt@Ag@Au nanocubes, they were synthesized using a similar protocol by simply replacing the Au@Ag nanocubes with the Pd@Ag and Pt@Ag nanocubes, respectively.

Synthesis of M@Au/Ag nanorattles (M = Au, Pd, and Pt). The M@Au/Ag nanorattles were synthesized through a galvanic replacement reaction between the M@Ag@Au nanocubes and $HAuCl_4$. In the case of Au@Au/Ag, 0.5 mL of the double-shelled nanocubes was introduced into a 20 mL glass vial containing 3 mL aqueous PVP (2 mg mL^{-1}) under magnetic stirring, followed by the titration of aqueous $HAuCl_4$ (0.1 mM) at a rate of 0.1 mL min^{-1} using a syringe pump. The color of the reaction mixture turned from brownish-yellow to reddish-yellow, and then to brown and blue. UV-vis spectra were used to track the reaction process. The addition of $HAuCl_4$ was stopped when the desired LSPR peak was reached. The solid products were collected through centrifugation at 25,000 rpm for 20 min, washed once with DI water. and re-dispersed in 0.5 mL of DI water. For the Pd@Ag/Au and Pt@Ag/Au nanorattles, they were synthesized using a similar protocol by replacing Au@Ag@Au nanocubes with Pd@Ag@Au and Pt@Ag@Au nanocubes, respectively.

Live/dead dual staining. MDA-MB-231 human breast cancer cells were seeded in a 24-well plate at a density of 5×10^4 cells per well and cultured in DMEM medium supplemented with 10% fetal bovine serum (FBS) and 1% Penicillin-Streptomycin for 24 h. Afterwards, the cells were incubated with 500 μL of fresh DMEM cell medium containing the Au@Au/Ag nanorattles at a concentration of 20 μg mL^{-1} for 4 h, followed by irradiation with a laser (808 nm) at a power density of 1 W cm^{-2} for 5 min. The medium was replaced with 0.5 mL of PBS solution containing 1 μg mL^{-1} calcein-AM dye and 5 μg mL^{-1} red fluorescent reactive dye at 37 ℃ for 15 min to stain the live and dead cells,

respectively. Finally, the cells were washed twice with PBS and imaged by fluorescence microscopy.

MTT cell viability assay. MDA-MB-231 human breast cancer cells were seeded in a 96-well plate at a density of 1×10^4 cells per well. After incubation at 37 ℃ for 24 h, the cells were re-cultured in 100 mL of fresh medium containing 20 μg mL^{-1} the Au@Au/Ag nanorattles for 4 h, followed by irradiation with the 808 nm laser for 5 min at 0.25, 0.5 and 1 W cm^{-2}, respectively. The medium was then removed and the cells were re-cultured in 100 μL of fresh DMEM medium for additional 20 h at 37 °C. Afterwards, 25 μL of MTT solution (5 mg mL^{-1}) was added into each well and the cells were incubated at 37 ℃ for another 2 h. The medium containing MTT was replaced with 100 μL of 2-propanol, and the plate was shaken at 37 ℃ for 10 min to completely dissolve the formed formazan crystals. Finally, the absorbance of each well at 570 nm was recorded using a microplate reader (Tecan, Durham, NC).

Instrumentation. The UV-vis spectra were recorded on a Cary 60 spectrometer (Agilent Technologies, Santa Clara, CA). The metal contents were analyzed using an inductively coupled plasma mass spectrometer (NexION 300Q, PerkinElmer, Waltham, MA). Transmission electron microscopy images were taken using an HT7700 microscope (Hitachi, Tokyo, Japan) operated at 120 kV. The TEM sample was prepared by casting a drop of the product on a carbon-coated copper grid (Electronic Microscopy Science, Redding, CA) and dried under ambient conditions. Cell imaging was carried out using a DMI6000 fluorescence microscopy (Leica, Buffalo Grove, IL).

Simulation Details. The discrete-dipole approximation (DDA) was used to simulate the extinction spectra of the Au@Ag core-shell nanocubes, Au@Ag@Au double-shelled nanocubes, and Au@Au/Ag nanorattles synthesized in this study. The software used for the simulation is ddscat 7.2.0 [25]. The Au@Ag core-shell nanocube was composed by a 5.5 nm Au sphere isotropically encapsulated by a 13.4 nm Ag cube. The cubes were truncated along the edges ({110} facets) and corners ({111} facets), with truncation

distances (*i.e.*, from the edge and corner location to the center) of (2/3, 2/3, 0) nm and (5/2, 5/2, 5/2) nm as illustrated in Figure 4.12. The Au@Ag@Au double-shelled nanocubes were simulated by isotropically encapsulating a 5.5 nm Au sphere inside a 13.5 nm Ag cube without truncation. Then, a conformal 0.2 nm Au overlayer was added to the surface of the structure. The Au@Au/Ag nanorattle structure was simulated by placing a 5.5 nm Au sphere inside an 18-nm Au/Ag nanocage having a shell thickness of 2 nm. To generate voids at the corners, eight 6.7 nm spheres (centered at a distance of 1.7, 1.7, 1.7 nm away from the corners) were subtracted from the corner sites. The structure was truncated along the edges ({110} facets) with a truncation distance of (2/3, 2/3, 0) nm. The dielectric constants for Au and Ag and Au/Ag ($Au_{52}Ag_{48}$) were taken from literature [26, 27]. In all cases, the propagation (*k*-vector) and electric field (*E*-field) of the incident photon were perpendicular and parallel to the (100)-facet of the cube, respectively. Furthermore, in all simulations, greater than 10^5 dipoles were used. The empty space in the simulation was given a refractive index of 1.33 to simulate the water environment.

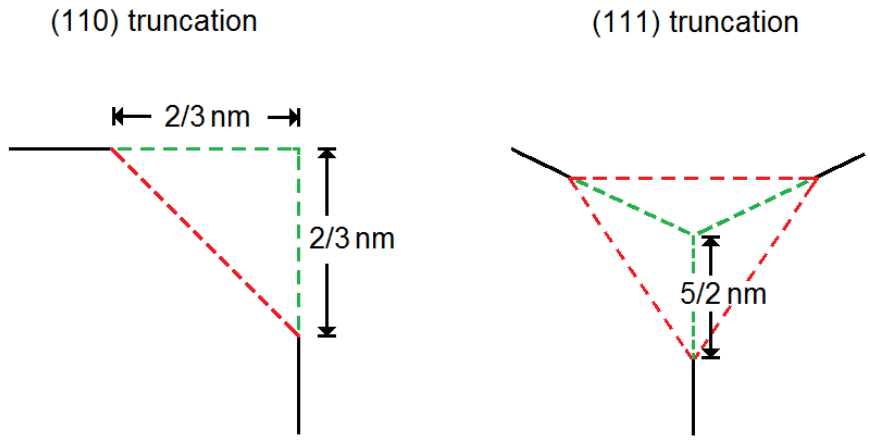

Figure 4.12. Truncation model used in the DDA simulation [28]. Printed with permission of John Wiley & Sons. Copyright 2017.

4.5 Notes to Chapter 4

Part of this chapter is adapted from a paper entitled "A general approach to the synthesis of M@Au/Ag (M = Au, Pd, and Pt) nanorattles with ultrathin shells less than 2.5 nm thick", which was co-authored by me and published in *Particle and Particle Systems Characterization* [28].

4.6 References

[1] Yang, X.; Yang, M.; Pang, B.; Vara, M.; Xia, Y. *Chem. Rev.* **2015,** *115*, 10410−10488.

[2] Xia, Y.; Li, W.; Cobley, C. M.; Chen, J.; Xia, X.; Zhang, Q.; Yang, M.; Cho, E. C.; Brown, P. K. *Acc. Chem. Res.* **2011,** *44*, 914−924.

[3] Chen, J.; Yang, M.; Zhang, Q.; Cho, E. C.; Cobley, C. M.; Claus, C.; Kim, C.; Wang, L. V.; Welch, M. J.; Xia, Y. *Adv. Funct. Mater.* **2010,** *20*, 3684−3694.

[4] Skrabalak, S. E.; Au, L.; Li, X.; Xia, Y. *Nat. Protoc.* **2007,** *2*, 2182−2190.

[5] Sonavane, G.; Tomoda, K.; Makino, K. *Colloids Surf. B* **2008,** *66*, 274−280.

[6] Fonge, H.; Lee, H.; Reilly, R. M.; Allen, C. *Mol. Pharmaceutics* **2010,** *7*, 1195−1208.

[7] Wang, Y.; Zheng, Y.; Huang, C.; Xia, Y. *J. Am. Chem. Soc.* **2013,** *135*, 1941−1951.

[8] Ma, Y.; Li, W.; Cho, E. C.; Li, Z.-Y.; Yu, T. K.; Zeng, J.; Xie, Z.; Xia, Y. *ACS Nano* **2010,** *4*, 6725−6734.

[9] Priebe, M.; Fromm, K. M. *Chem. Eur. J.* **2015,** *21*, 3854−3874.

[10] Kuai, L.; Wang, S.; Geng, B. *Chem. Commun.* **2011,** *47*, 6093−6095.

[11] Kuai, L.; Geng, B.; Wang, S.; Sang, Y. *Chem. Eur. J*. **2012,** *18*, 9423−9429.

[12] Xie, S.; Jin, M.; Tao, J.; Wang, Y.; Xie, Z.; Zhu, Y.; Xia, Y. *Chem. Eur. J.* **2012,** *18*, 14974−14980.

[13] Wan, D.; Xia, X.; Wang, Y.; Xia, Y. *Small* **2013,** *9*, 3111−3117.

[14] Yang, Y.; Liu, J. Y.; Fu, Z.-W.; Qin, D. *J. Am. Chem. Soc.* **2014,** *136*, 8153−8156.

[15] Zheng, Y.; Ma, Y.; Zeng, J.; Zhong, X.; Jin, M.; Li, Z.-Y.; Xia, Y. *Chem. Asian J.* **2013,** *8*, 792−799.

[16] Link, S.; El-Sayed, M. A. *J. Phys. Chem. B* **1999,** *103*, 4212−4217.

[17] Yang, Y.; Zhang, Q.; Fu, Z.-W.; Qin, D. *ACS Appl. Mater. Interfaces* **2014,** *6*, 3750−3757.

[18] Polavarapu, L.; Zanaga, D.; Altantzis, T.; Rodal-Cedeira, S.; Pastoriza-Santos, I.; Pérez-Juste, J.; Bals, S.; Liz-Marzán, L. M. *J. Am. Chem. Soc.* **2016,** *138*, 11453−11456.

[19] Wang, X.; Zhang, Z.; Hartland, G. V. *J. Phys. Chem. B* **2005,** *109*, 20324−20330.

[20] Chen, J.; Wiley, B.; Li, Z.-Y.; Campbell, D.; Saeki, F.; Cang, H.; Au, L.; Lee, J.; Li, X.; Xia, Y. *Adv. Mater.* **2005,** *17*, 2255−2261.

[21] Gonzalez, C. M.; Liu, Y.; Scaiano, J. C. *J. Phys. Chem. C* **2009,** *113*, 11861−11867.

[22] Au, L.; Lu, X.; Xia, Y. *Adv. Mater.* **2008,** *20*, 2517−2522.

[23] Zeng, J.; Goldfeld, D.; Xia, Y. *Angew. Chem. Int. Ed.* **2013,** *52*, 4169−4173.

[24] Zhang, H.; Jin, M.; Wang, J.; Kim, M. J.; Yang, D.; Xia, Y. *J. Am. Chem. Soc.* **2011,** *133*, 10422−10425.

[25] Flatau, P. J.; Draine, B. T. *Opt. Express* **2012,** *20*, 1247−1252.

[26] Johnson, P. B.; Christy, R. W. *Phys. Rev. B* **1972,** *6*, 4370.

[27] Peña-Rodr ǵuez, O.; Caro, M.; Rivera, A.; Olivares, J.; Perlado, J. M.; Caro, A. *Opt. Mater. Express* **2014,** *4*, 403−410.

[28] Yang, M.; Gilroy, K. D.; Xia, Y. *Part. Part. Syst. Charact.* **2017,** DOI: 10.1002/ppsc.201600279.

CHAPTER 5

COATING SILVER NANOWIRES WITH ULTRATHIN SHEATHS OF GOLD TO IMPROVE THEIR STABILITY AGAINST OXIDATION

5.1 Introduction

Transparent conductors are a key component in many electrical devices, such as displays, touch screens, organic light emitting diodes (OLEDs), smart windows, and organic photovoltaics (OPVs) [1]. Currently, indium tin oxide (ITO) is the dominant material for the production of such conductors owing to its advanced optical and electrical properties (*e.g.*, with a transmittance on glass >90% at 10 Ω sq^{-1}) [2, 3]. However, the abundance of indium on earth is very low (1.6×10^{-5} %), and there is no pure mineral or ore for this metal, making ITO expensive in terms of material cost. Besides, the fabrication of ITO films requires a vapor-phase sputtering process, which is marred by its slow production rate and much higher cost relative to a liquid-based coating process [4]. Apart from the production and cost issues, ITO films are also troubled by brittleness and strong optical absorption in the near-infrared (NIR) region. All these issues motivate the research community to find a suitable replacement for ITO. The substitute is expected to be flexible, low cost in terms of both material and fabrication, and possess a conductivity and transmittance as high as ITO.

Up until now, various types of materials have been proposed and studied for this purpose; notable examples include conducting polymers [5], carbon nanotubes [6], graphenes [7], and metallic nanowires [4, 8]. Among them, Ag nanowires represent a promising candidate because of not only high electrical conductivity (16 nΩ m, the highest among all metals) and good mechanical flexibility of the resulting film, but also a facile solution-based film fabrication process [8]. One obstacle hampering the real-world application of Ag nanowires lies in the high tendency of Ag toward oxidation when

exposed to air [9, 10]. The resulting oxidation product, silver oxide, will gradually cover the surface of the Ag nanowires, reducing both their electrical conductivity and light transmittance [11]. To mitigate this issue, it is necessary to protect Ag nanowires by means of surface coating. Several coating techniques have been reported in literature, including those based upon organic materials [12], polymers [11, 13], and metals [14], among others. Indeed, the coated Ag nanowires showed improvement in stability against oxidation, but at the cost of *i*) reduced electrical conductivity, *ii*) lowered transparency, and *iii*) increased fabrication cost. Alternatively, coating Ag nanowires with metallic Au, an inert metal well-known for its high resistance against oxidation, could potentially offer a better solution. However, it is challenging to fabricate such a core-sheath structure owing to the thermodynamically favored galvanic replacement reaction between elemental Ag and Au^{+} or Au^{3+} species [15]. As a result, one can only obtain Ag/Au alloyed hollow structures instead of the well-defined Ag@Au core-sheath nanowires.

In this chapter, I demonstrated a facile synthesis of Ag@Au core-sheath nanowires *via* the reduction of $Au(OH)_4^-$ by ascorbic acid (AA) in the presence of Ag nanowires under an alkaline condition. A schematic illustration of the process is shown in Figure 5.1. Upon optimization of experimental conditions, the galvanic replacement can be suppressed to enable conformal deposition of Au atoms as a dominant process, leading to the formation of well-defined Ag@Au nanowires. These core-sheath nanowires are essentially identical to the pristine Ag nanowires in terms of morphology and optical properties, but with much improved stability against oxidation, thanks to the protection by the Au sheath. As a result, the Ag@Au core-sheath nanowires can serve as a potential replacement for ITO in the production of transparent conductors.

5.2 Results and Discussion

The industrial applications of transparent Ag nanowire films require a high stability of the electrode materials against oxidation throughout the product lifetime, which typically

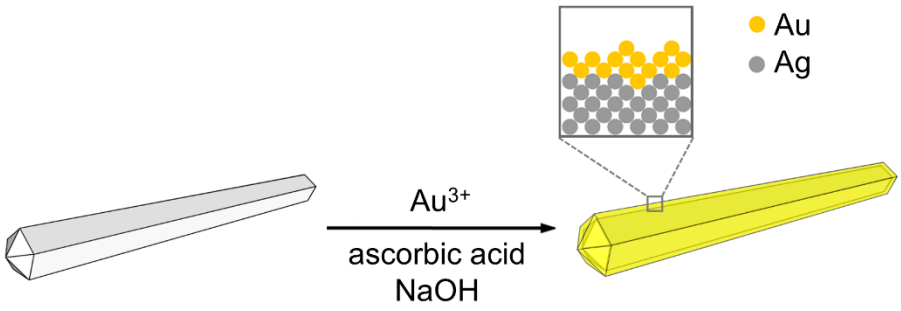

Figure 5.1. A schematic illustration of structural changes for Ag nanowires before and after their surfaces have been coated with Au. The stability of Ag@Au core-sheath nanowires is greatly enhanced against oxidation when compared to the pristine Ag nanowires. Reprinted with permission from [27]. Copyright 2017 Royal Society of Chemistry.

lasts for several years, or even decades. However, elemental Ag is known to be susceptible to oxidation by the oxygen from air. To address this issue, I propose to conformally coat the surface of Ag nanowires with an ultrathin sheath of Au to enhance their stability against oxidation. My rationale is supported by the chemical inertness of Au, as well as the similarity in terms of electrical conductivity between bulk Au (24 nΩ m) and bulk Ag (16 nΩ m). Also, the close matching in lattice constant between these two noble metals also facilitates epitaxial deposition of Au on Ag, ensuring the formation of a protective barrier. Silver nanowires were synthesized using a polyol-based protocol recently developed by our group [16], in which NaBr and poly(vinyl pyrrolidone) (PVP) with a molecular weight of 1,300,000 were introduced to modify the conventional polyol method. As shown in Figure 5.2, the Ag nanowires had an average diameter of 34 ± 6 nm, together with lengths up to 20 μm.

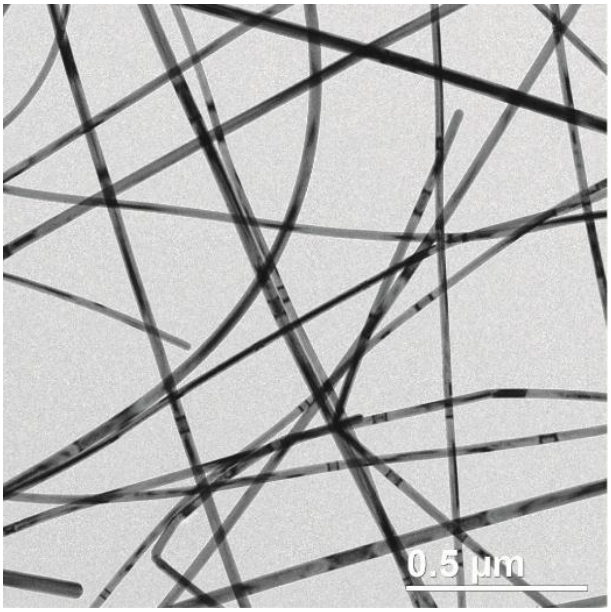

Figure 5.2. TEM image of the pristine Ag nanowires before Au deposition. Reprinted with permission from [27]. Copyright 2017 Royal Society of Chemistry.

The Ag@Au core-sheath nanowires were prepared through conformal deposition of Au atoms on the pre-synthesized Ag nanowires. Ascorbic acid was used as a reducing agent for the deposition, and an alkaline condition (pH≈11.0) was created through the addition of NaOH. Under this condition, the reducing power of AA is drastically enhanced, accelerating the reduction of Au^{3+} to Au to circumvent the galvanic replacement between Au^{3+} and Ag [17]. However, a complete suppression of such a reaction seems to be impossible according to the experimental results discussed in Chapter 4, which inevitably creates voids in the Ag nanowires and thereby cause some changes to their optical properties [18]. To further reduce the possibility of galvanic replacement, I tried to increase the energy barrier for this reaction by lowering the reduction potential of the Au^{3+}/Au pair. It was reported that the Cl^- in $AuCl_4^-$ could be replaced by OH^- ions consecutively, and

the degree of reaction is pH dependent [19]. Accompanying the ligand exchange, the reduction potential of Au^{3+} species would gradually decrease in the order of $AuCl_4^-$ > $Au(OH)Cl_3^-$ > $Au(OH)_2Cl_2^-$ > $Au(OH)_3Cl^-$ > $Au(OH)_4^-$. When the pH value was higher than 10.35, almost all (>97%) of the Au^{3+} ions in the solution would take the form of $Au(OH)_4^-$, which showed the lowest oxidation ability [19]. Based on this concept, I prepared an alkaline solution containing $HAuCl_4$ (0.1 mM) and NaOH (20 mM), aiming to transform $AuCl_4^-$ to $Au(OH)_4^-$. The alkaline $Au(OH)_4^-$ solution was then used as a Au source in the following experiment. With the efforts from both the low reduction potential of $Au(OH)_4^-$/Au and the strong reducing capability of AA under alkaline condition, the galvanic replacement between Au^{3+} and Ag was effectively suppressed, generating Ag@Au nanowires without any voids.

Figure 5.3a shows a representative TEM image of the resulting core-sheath nanowires, whose morphology appeared to be identical to that of the pristine Ag nanowires due to the involvement of an ultrathin Au coating. The thickness of the Au sheath could be easily manipulated by varying the amount of Au precursor titrated into the reaction solution, as implied by the increase of Au content in the final product measured by inductively coupled plasma mass spectrometry (ICP-MS). As shown in Table 5.1, the atomic percent of Au in the Ag@Au nanowires could be readily tuned from 5.1% to 10.8% by simply increasing the volume of $Au(OH)_4^-$ solution (0.1 mM) introduced into the reaction system from 0.5 to 2.0 mL. These Au contents corresponded to average coating thicknesses of 2 and 4 atomic layers (~1 nm), respectively, by assuming that the deposition of Au was conformal and uniform.

The optical properties of the nanowires were monitored using UV-vis spectroscopy during the synthesis, and the results are summarized in Figure 5.3b. Briefly, the presence of an ultrathin Au sheath on the Ag nanowires only brought some minor changes to their optical properties. Specifically, the Ag@Au nanowires with various Au contents all showed extinction spectra almost identical to that of the pristine Ag nanowires. A slight

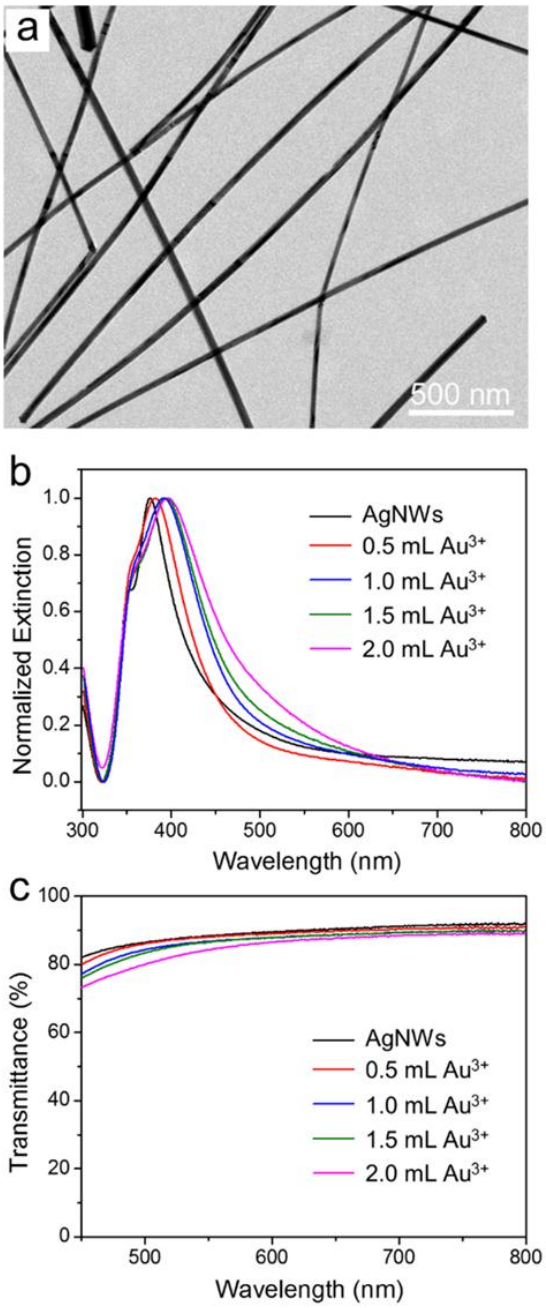

Figure 5.3. (a) TEM image of Ag@Au core-sheath nanowires, (b, c) UV-vis absorbance and transmittance spectra of pristine Ag nanowires and Ag@Au core-sheath nanowires prepared by adding different volumes of Au^{3+} solution (0.5, 1.0, 1.5 and 2.0 mL). Reprinted with permission from [27]. Copyright 2017 Royal Society of Chemistry.

Table 5.1 Gold contents in Ag@Au core-sheath nanowires prepared by adding different volumes of $Au(OH)_4^-$ solution (0.5, 1.0, 1.5 and 2.0 mL) as determined by ICP-MS.

Volume of 0.1 mM $Au(OH)_4^-$ solution added (mL)	% Au in Ag@Au core-sheath nanowires
0.5	5.1
1.0	6.6
1.5	7.6
2.0	10.8

red shift for the LSPR peak from 376 nm to 381 nm was observed after the initial addition of 0.5 mL Au^{3+} precursor solution, together with negligible broadening in peak width. Introducing more $Au(OH)_4^-$ solution would bring further red shifts to the LSPR peak, together with obvious broadening of the peak width, primarily due to the change in dielectric constant caused by the Au coating [20]. This observation was consistent with the experimental results reported for Ag@Au core-shell nanowires prepared by means of galvanic replacement [21]. Most importantly, the high transmittance of the pristine Ag nanowires was largely retained after Au deposition. As shown in Figure 5.3c, a minimum decrease in light transmittance was observed for the Ag@Au nanowires as compared to the pristine Ag nanowires. At a concentration of 70 μg/mL for Ag, the suspensions of both Ag and Ag@Au nanowires show high transmittance (>70%) in the visible region from 450 to 800 nm.

The morphology of the Ag@Au core-sheath nanowires was also examined by means of high-resolution TEM. As shown in Figure 5.4a, the original structure of the Ag nanowire was well-preserved after the deposition of Au with no observable voids, confirming the suppression of galvanic replacement under the reaction conditions. The deposited Au sheath could be readily resolved by the presence of a darker layer alongside the edge of the pristine nanowire. Different from the uniform coating of Au reported for Ag@Au nanocubes [17], the Au sheath was not evenly distributed across the surface of a Ag nanowire, with the presence of Au-rich and Au-deficient domains. Given the extremely high aspect ratio of the pristine Ag nanowires, it is not unreasonable to expect fluctuation for the sheath thickness because of the varied amounts of Au deposition at different sites along each nanowire. Besides, the presence of capping agents, such as Br^- ions and PVP, further contributed to the complexity of surface conditions on Ag nanowires, leading to Au coatings with variation in thicknesses.

To gain more information on the Au sheath, high-angle annular dark-field scanning TEM (HAADF-STEM) analysis was carried out. The image in Figure 5.4c shows a clear contrast between the sheath and the underlying nanowire due to the difference in atomic number between Au and Ag. The thickness of the Au sheath was observed to be 2−3 atomic layers, which was in reasonable agreement with the ICP-MS data. The formation of Ag@Au core-sheath structure was further confirmed by energy-disperse X-ray spectroscopy (EDS), as shown in Figure 5.4, d−g. The conformal sheath can be attributed to the use of an elevated reaction temperature (60 ^oC) and a slow injection rate for the Au^{3+} precursor, which facilitate the diffusion of Au atoms to reach the entire surface on a nanowire after their deposition. When the synthesis was conducted at room temperature (22 ^oC), nanowires with a rough surface were obtained (Figure 5.5a). After reacting with H_2O_2, such Ag@Au nanowires were partially dissolved, leaving behind multiple thinner nanowires (Figure 5.5b). These fine structures correspond well to the ridges of the penta-twinned Ag nanowires, suggesting that the deposition of Au was initiated from the side

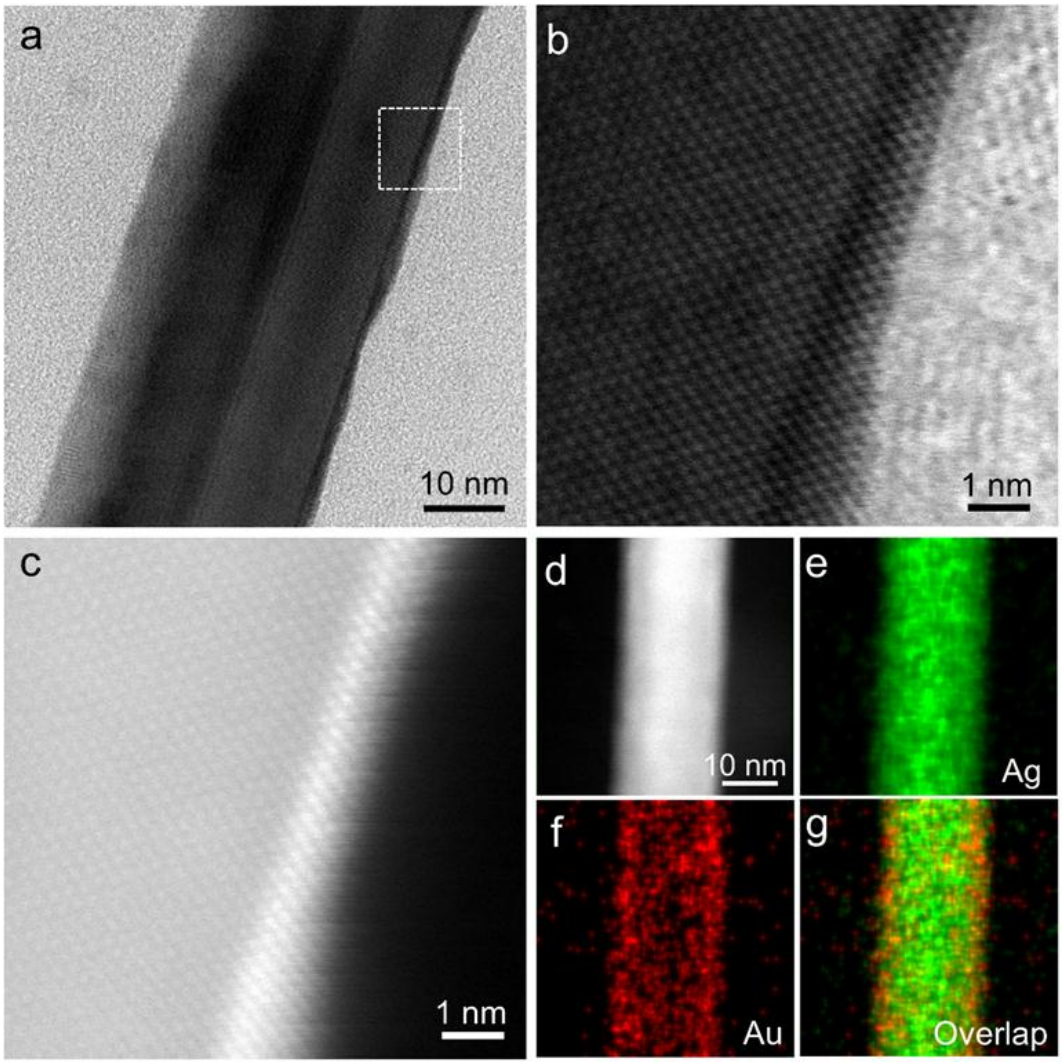

Figure 5.4. (a, b) High-resolution TEM and (c) HAADF-STEM images of a Ag@Au core-sheath nanowire taken from the sample shown in Figure 5.2a. (d−g) EDS elemental mapping of Ag and Au in a Ag@Au core-sheath nanowire. Reprinted with permission from [27]. Copyright 2017 Royal Society of Chemistry.

ridges on the Ag nanowire. The site-selected deposition of Au can be attributed to the presence of Br^- ions during the synthesis of Ag nanowires, which bind tightly to the side {100} facets on Ag nanowires [16]. As a result, the Au atoms could only nucleate and grow from ridges. Without sufficient diffusion, the Au atoms remained at their initial deposition sites, forming a rough surface and leaving the majority of the side surface uncovered by Au. The surface diffusion of Au atoms could be greatly accelerated by increasing the reaction temperature, making transportation possible for ridge-bound Au atoms to the {100} side faces, achieving a complete Au coating over the entire Ag nanowire. This observation agrees well with our previous report on the role of surface diffusion in the synthesis of core-shell nanocrystals [22].

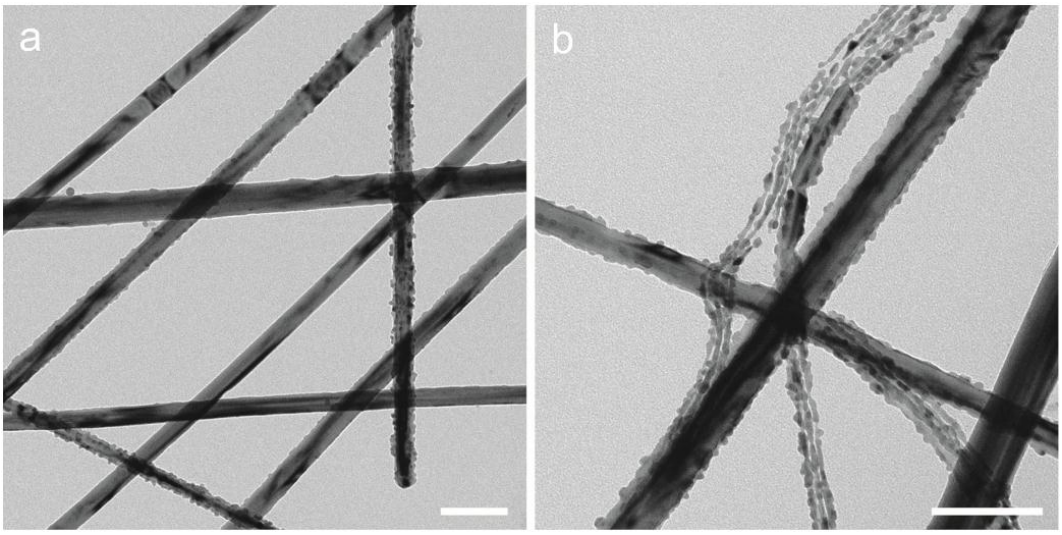

Figure 5.5. TEM images of the Ag@Au core-sheath nanowires synthesized at room temperature (a) before and (b) after H_2O_2 etching. The scale bars are 100 nm. Reprinted with permission from [27]. Copyright 2017 Royal Society of Chemistry.

To evaluate their stability against oxidation, three different types of oxidants, including O_2, H_2O_2, and $Fe(NO_3)_3$, were deliberately introduced into the suspensions of Ag nanowires and Ag@Au core-sheath nanowires. The degree of oxidation was derived from the UV-vis spectra and TEM images recorded before and after the treatment with each oxidant. Oxygen gas is the most commonly encountered oxidant in our life, which accounts for 21% (by volume) in air. I first tested the stability of Ag and Ag@Au nanowires in the presence of pure O_2 gas. In this case, pure O_2 was bubbled into a suspension of the nanowires for 1 h and the UV-vis spectrum was compared to the one taken before bubbling with O_2. As shown in Figure 5.6a, the LSPR peak intensity decreased by ca. 30% for pristine Ag nanowires during the treatment with O_2. Under the same experimental condition, the Ag@Au nanowires only showed 15% drop in intensity for the LSPR peak. The peak position and peak shape of both samples did not change during the treatment, suggesting that O_2 alone is not adequate to significantly etch the Ag or Ag@Au nanowires. Still, the decrease in peak intensity should not just be attributed to the oxidation of nanowires, as some of the nanowires could be lost during the bubbling process due to the nanowire absorption onto both the glass pipette (for the introduction of O_2) and the centrifuge tube.

Next, I turned to hydrogen peroxide (H_2O_2) to evaluate the stability of the Ag and Ag@Au nanowires. In previous reports, H_2O_2 was shown to effectively etch away Ag nanostructures even at a concentration level as low as 0.1% [23]. In the present study, 5% aqueous H_2O_2 solution (1.7 M) was used, which was far beyond the concentration commonly used for Ag etching. The H_2O_2 solution was mixed with the suspension of Ag@Au core-sheath nanowires in a 1:1 ratio (v/v, with a final H_2O_2 concentration of 2.5%, *i.e.*, 0.85 M in molar concentration), and the mixture was kept at room temperature for 1 h. In a control experiment, pristine Ag nanowires were used instead, with all other experimental conditions kept exactly the same. After incubation for 1 h, UV-vis spectra were taken from both two samples, and the results are summarized in Figure 5.6. As

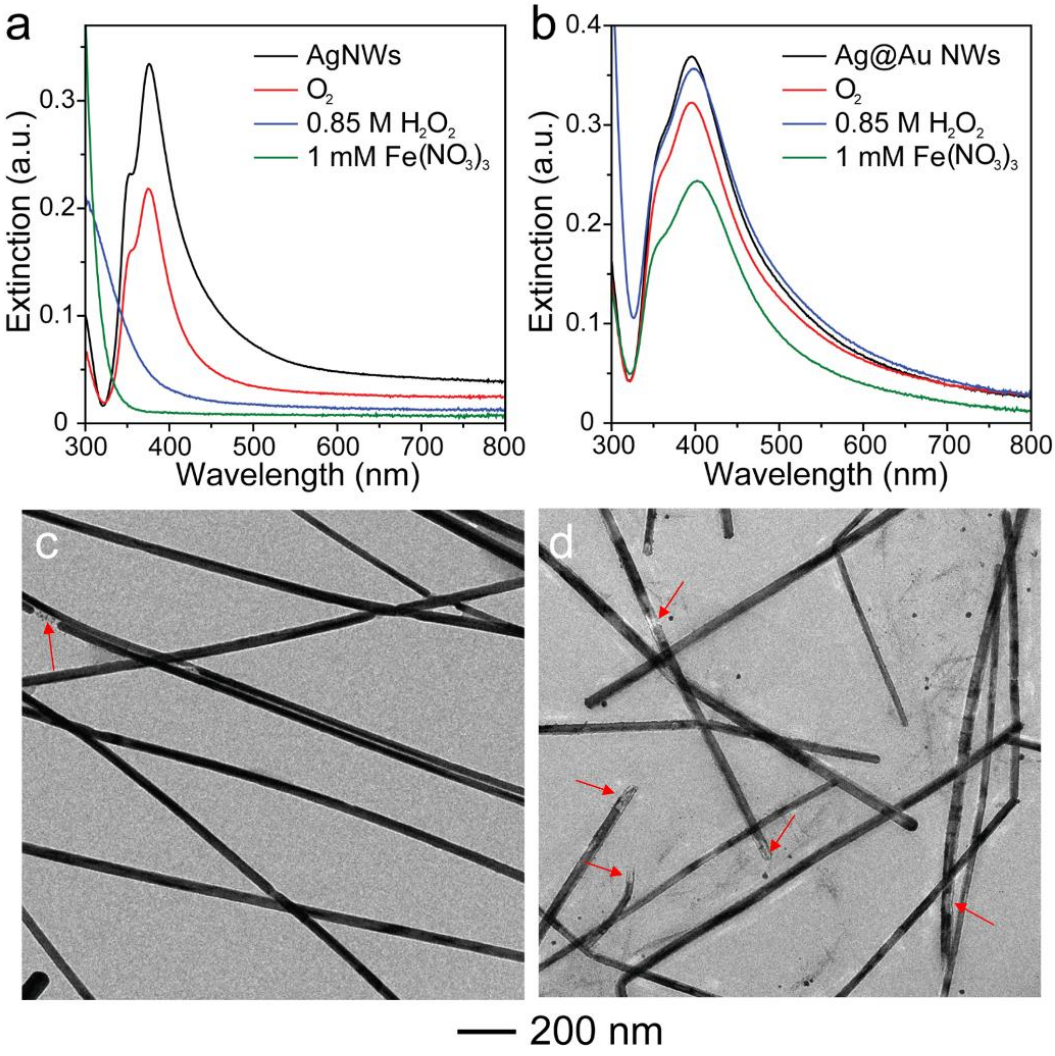

Figure 5.6. UV-vis spectra of (a) pristine Ag nanowires and (b) Ag@Au core-sheath nanowires before and after the etching with gaseous O_2, 0.85 M aqueous H_2O_2 solution, and 1 mM aqueous $Fe(NO_3)_3$ solution, and corresponding TEM images of Ag@Au core-sheath nanowires after etching with (c) H_2O_2 and (d) $Fe(NO_3)_3$. Red arrows indicate the locations that have been etched. Reprinted with permission from [27]. Copyright 2017 Royal Society of Chemistry.

expected, there were hardly any Ag nanowires remaining after H_2O_2 treatment because of the complete dissolution of Ag through oxidation, as indicated by a flat line in the extinction spectrum. With the presence of a Au sheath, a decreased change in the optical properties was observed, confirming its role in effectively protecting the underlying Ag. Specifically, for Ag@Au nanowires with 2−3 atomic layers of Au coating, I only observed ca. 3% reduction in LSPR peak intensity, indicating essentially no dissolution of Ag during the treatment. Figure 5.6c shows a typical TEM image of the Ag@Au core-sheath nanowires after H_2O_2 etching. It was clear that the majority of the nanowires kept their original concrete structure. Only a few voids were observed due to the dissolution of Ag at sites where Au coating was not complete. Compared to the same sample before etching (Figure 5.2), no obvious morphological difference was observed, confirming the effective protection of Ag nanowires by the Au sheath.

Ferric salts represent another class of commonly used oxidants for Ag, which also exist as ionic species in aqueous solutions. I also evaluated the stability of Ag and Ag@Au nanowires against ionic oxidants using aqueous $Fe(NO_3)_3$ as a model system. Briefly, to a suspension of Ag or Ag@Au nanowires, aqueous $Fe(NO_3)_3$ solution was added. The mixture was vortexed and kept at room temperature for 1 h. After that, the solid products were collected through centrifugation, and re-dispersed in water for UV-vis analysis. Compared to the original Ag@Au nanowires, the Fe^{3+}-treated sample was observed to have a decreased LSPR peak intensity (by ca. 33%), together with a slightly red-shift for the peak position (Figure 5.6b). These findings clearly indicate the etching of Ag@Au nanowires by Fe^{3+} ions. Again, the pristine Ag nanowires were complete dissolved when reacted with aqueous $Fe(NO_3)_3$, as indicated by the UV-vis spectrum shown in Figure 5.6a. A typical TEM image of the Fe^{3+}-treated Ag@Au nanowires was shown in Figure 5.6d, in which many hollow structures (as indicated by red arrows) were observed, in agreement with the spectroscopic results. Overall, the morphology of the Ag@Au nanowires did not change substantially, suggesting a reasonable stability for the core-sheath nanowires in the

presence of Fe^{3+} salts at low concentrations up to 1 mM. In addition, the Ag@Au nanowires also showed good chemical stability in aqueous NaHS (5 μM) and NaCl (100 mM) solutions, respectively (as shown in Figure 5.7)

Based on these experimental results, I could conclude that the presence of an ultrathin Au sheath was able to significantly improve the stability of Ag nanowires against oxidation. Specifically, the Ag@Au nanowires with a Au sheath of only 2-3 atomic layers exhibited excellent stability against oxidation caused by O_2 and H_2O_2, whereas somewhat reduced stability was observed for ionic oxidants such as Fe^{3+}. In comparison, pristine Ag nanowires only showed good stability against O_2, and they were completely dissolved when treated with the other two oxidants. The stability against O_2 for both Ag and Ag@Au nanowires may come from the limited solubility of O_2 gas in water at room temperature. Besides, the formation of AgOH precipitates through the oxidation of Ag may also contribute to the stability, in that they could passivate the surface of nanowires and slow down further oxidation [24]. When $Fe(NO_3)_3$ was used as an etchant, the corresponding oxidation product, $AgNO_3$, is soluble in water at room temperature, which ensures continuation of the etching process. Also, ferric salts have been reported to have the highest oxidation power among the three oxidants [23, 25], correlated well with the lowest amount required for an effective etching observed in this study. In the case of H_2O_2, Ag nanostructures have been reported to serve as a catalyst for its decomposition into O_2 or reactive oxygen species, such as HOO^-, $O_2^{\bullet -}$ and ·OH [26]. These decomposition products are credited for the effective etching of Ag nanomaterials due to their much stronger oxidation capability compared to the pristine H_2O_2 molecules. However, the Au sheath can serve as an insurmountable barrier for H_2O_2 molecules, minimizing their contact with the Ag surface and greatly slowing down the decomposition process, thus dramatically improving the stability of the core-sheath nanowires against H_2O_2.

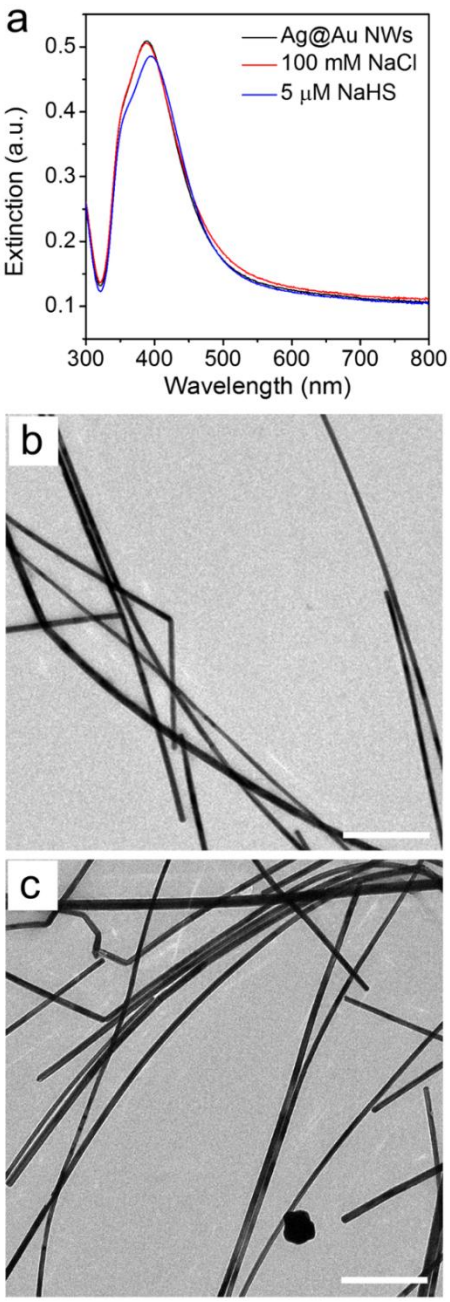

Figure 5.7. (a) UV-vis spectra of the Ag@Au core-sheath nanowires before and after incubation with two different aqueous solutions: 100 mM NaCl and 5 μM NaHS for 2 h, respectively. (b) TEM image of the Ag@Au core-sheath nanowires after incubation with 100 mM NaCl aqueous solution. (c) TEM image of the Ag@Au core-sheath nanowires after incubation with 5 μM NaHS aqueous solution. The scale bars are 500 nm. Reprinted with permission from [27]. Copyright 2017 Royal Society of Chemistry.

5.3 Conclusion

In summary, I have demonstrated the synthesis of Ag@Au core-sheath nanowires *via* the direct deposition of Au atoms onto the surface of pre-synthesized Ag nanowires. According to our experimental measurements, the Au-coated nanowires resembled those of the pristine Ag nanowires in terms of morphology and optical properties, with high transparency in the visible region. The thickness of the Au sheath could be readily tuned by varying the amount of Au^{3+} precursor added into the reaction. The as-prepared Ag@Au core-sheath nanowires exhibited greatly enhanced stability against the oxidation by various types of oxidants, including O_2, H_2O_2, and $Fe(NO_3)_3$. Taken together, the Ag@Au core-sheath nanowires are expected to find use as a potential replacement for the conventional Ag nanowires in the fabrication of flexible transparent conductors.

5.4 Experimental Section

Chemicals and Materials. *L*-ascorbic acid (>99.0%), sodium hydroxide (NaOH, >98%), poly(vinyl pyrrolidone) ($M_W \approx$ 1,300,000 and 55,000), gold(III) chloride trihydrate (>99.9%), iron(III) nitrate nonahydrate (>98%), and hydrogen peroxide solution (30% w/w in H_2O) were all obtained from Sigma-Aldrich (St. Louis, MO). Oxygen (O_2, ultra high purity) was purchased from Nexair (Memphis, TN). All chemicals were used as received. Deionized water with a resistivity of 18.2 MΩ·cm at room temperature was used throughout the experiments.

Synthesis of Ag Nanowires. The silver nanowires were synthesized by following a recently reported protocol with slight modifications. In a typical synthesis, two solutions of $AgNO_3$ (100 mM) and NaBr (250 mM) in ethylene glycol were prepared. At the same time, 250 mg PVP ($M_W \approx$ 1,300,000) was dissolved in 20 mL of EG in a 50 mL flask and heated in an oil bath at 170 ℃ for 60 min under magnetic stirring (320 rpm). After 60 min, 120 μL of the NaBr solution in EG was added into the flask. After another 5 min, 15 mL

of the $AgNO_3$ solution in EG was added using a syringe pump at an injection rate of 1.5 mL/min. The synthesis was quenched by immersing the flask in an ice water bath 35 min after the introduction of $AgNO_3$ solution. The solid products were crashed out with acetone, washed twice with water, and finally re-dispersed in 30 mL of water. The suspension was centrifuged at a speed of 800 rpm for 15 min to remove Ag nanoparticles larger than 100 nm in size. The supernatant containing Ag nanowires was collected while the precipitate (containing nanoparticles and some nanowires) was discarded. The washing procedure was repeated three additional times. Finally, the Ag nanowires were collected by centrifugation at 3,000 rpm for 10 min and re-suspended in 5 mL of water.

Preparation of $Au(OH)_4^-$ solution. An aqueous $Au(OH)_4^-$ solution was prepared by mixing aqueous solutions of $HAuCl_4$ and NaOH. Specifically, 0.1 mL of aqueous $HAuCl_4$ (20 mM), 2 mL of aqueous NaOH (200 mM), and 17.9 mL water were added into a 20 mL vial, and the mixture was incubated at room temperature (22 ^oC) on an orbital shaker for 1 h. This solution contained $Au(OH)_4^-$ at a concentration of 0.1 mM, together with NaOH at 20 mM.

Synthesis of Ag@Au core-sheath nanowires. In a typical synthesis, 1 mL of aqueous PVP ($M_W \approx 55{,}000$, 40 mg/mL) and 2 mL water were mixed in a 20 mL glass vial. The mixture was then heated to 60 ^oC under magnetic stirring at a speed of 400 rpm. After 2 min, 500 μL of aqueous AA (100 mM) and 500 μL of aqueous NaOH (200 mM) were added sequentially, followed by 70 μL of the aqueous suspension of Ag nanowires. The aqueous solution of $Au(OH)_4^-$ (0.1 mM) and NaOH (20 mM) was then titrated using a syringe pump at an injection rate of 0.02 mL/min. After a certain amount of the $Au(OH)_4^-$ solution had been added, the solid products were collected by centrifugation at 3,500 rpm for 10 min, washed twice with water, and finally re-dispersed in 0.5 mL of water.

Etching of Ag@Au core-sheath nanowires with O_2. To a 1.5 mL centrifuge tube, 0.5 mL of water was added, followed by 0.5 mL of the as-prepared suspension of Ag@Au

core-sheath nanowires. After mixing, O_2 gas was bubbled through the solution for 1 h. Finally, the remaining solid was collected for further characterization.

Etching of Ag@Au core-sheath nanowires with H_2O_2. To a 1.5 mL centrifuge tube, 0.5 mL of the as-obtained suspension of Ag@Au core-sheath nanowires was added, followed by 0.5 mL of 5% aqueous H_2O_2. The initial concentration of H_2O_2 in the final reaction mixture was 2.5% (*i.e.*, 0.85 M). The suspension was vortexed for 5 s to ensure thorough mixing and then kept at room temperature for 1 h. Afterwards, the mixture was centrifuged at 3,500 rpm for 10 min to separate the solid products. After removing the supernatant, the remaining Ag@Au core-sheath nanowires were collected and re-dispersed in 0.5 mL of water for further characterization.

Etching of Ag@Au core-sheath nanowires with aqueous $Fe(NO_3)_3$. The procedure was the same as what was used for H_2O_2 etching except that the H_2O_2 was replaced with 0.5 mL of aqueous $Fe(NO_3)_3$ (2 mM). The initial concentration of $Fe(NO_3)_3$ in the final reaction mixture was 1 mM.

Instrumentation and characterization. UV-vis spectra were collected on a Cary 60 spectrometer (Agilent Technologies), and the metal contents were quantified using inductively coupled plasma mass spectrometry (NexION 300Q, Perkin Elmer). TEM images were collected on a Hitachi HT7700 microscope operated at 120 kV by drop casting samples onto carbon-coated Cu TEM grids. High-resolution TEM imaging, high-angle annular dark-field imaging, and energy-disperse X-ray spectroscopy analysis were all performed on an aberration-corrected JEOL JEM 2200FS STEM/TEM microscope operated at 200 kV, equipped with a CEOS probe detector (Heidelberg, Germany) and a Bruker-AXS silicon drift detector.

5.5 Notes to Chapter 5

Part of this chapter is adapted from a paper entitled “Facile synthesis of Ag@Au core-sheath nanowires with greatly improved stability against oxidation”, which was co-autjored by me and published in *Chemical Communications* [27].

5.6 References

[1] Gordon, R. G. *MRS Bull.* **2000,** *25*, 52−57.

[2] Zhang, D.; Ryu, K.; Liu, X.; Polikarpov, E.; Ly, J.; Tompson, M. E.; Zhou, C. *Nano Lett.* **2006,** *6*, 1880−1886.

[3] Hecht, D. S.; Hu, L.; Irvin, G. *Adv. Mater.* **2011,** *23*, 1482−1513.

[4] Ye, S.; Rathmell, A. R.; Chen, Z.; Stewart, I. E.; Wiley, B. J. *Adv. Mater.* **2014,** *26*, 6670−6687.

[5] Na, S.-I.; Kim, S.-S.; Jo, J.; Kim, D.-Y. *Adv. Mater.* **2008,** *20*, 4061−4067.

[6] Wu, Z.; Chen, Z.; Du, X.; Logan, J. M.; Sippel, J.; Nikolou, M.; Kamaras, K.; Reynolds, J. R.; Tanner, D. B.; Hebard, A. F.; Rinzler, A. G. *Science* **2004,** *305*, 1273−1276.

[7] Bae, S.; Kim, H.; Lee, Y.; Xu, X.; Park, J.-S.; Zheng, Y.; Balakrishnan, J.; Lei, T.; Kim, H. R.; Song, Y. I.; Kim, Y.-J.; Kim, K. S.; Özyilmaz, B.; Ahn, J.-H.; Hong, B. H.; Iijima, S. *Nat. Nanotechnol.* **2010,** *5*, 574−578.

[8] Hu, L.; Kim, H. S.; Lee, J.-Y.; Peumans, P.; Cui, Y. *ACS Nano* **2010**, *4*, 2955−2963.

[9] Henglein, A. *Chem. Mater.* **1998,** *10*, 444−450.

[10] Han, Y.; Lupitskyy, R.; Chou, T.-M.; Stafford, C. M.; Du, H.; Sukhishvili, S. *Anal. Chem.* **2011,** *83*, 5873−5880.

[11] Liu, B.-T.; Huang, S.-X. *RSC Adv.* **2014,** *4*, 59226−59232.

[12] Bashouti, M. Y.; Resch, S.; Ristein, J.; Mačković, M.; Spiecker, E.; Waldvogel, S. R.; Christiansen, S. H. *ACS Appl. Mater. Interfaces* **2015,** *7*, 21657−21661.

[13] Chen, S.; Song, L.; Tao, Z.; Shao, X.; Huang, Y.; Cui, Q.; Guo, X. *Org. Electron.* **2014,** *15*, 3654−3659.

[14] Eom, H.; Lee, J.; Pichitpajongkit, A.; Amjadi, M.; Jeong, J.-H.; Lee, E.; Lee, J.-Y.; Park, I. *Small* **2014,** *10*, 4171−4181.

[15] Xia, X.; Wang, Y.; Rudiskiy, A.; Xia, Y. *Adv. Mater.* **2013,** *25*, 6313−6333.

[16] Silva, R. R.; Yang, M.; Choi, S.-I.; Chi, M.; Luo, M.; Zhang, C.; Li, Z.-Y.; Camargo, P. H. C.; Ribeiro, S. J. L.; Xia, Y. *ACS Nan*o **2016,** *10*, 7892−7900.

[17] Yang, Y.; Liu, J.; Fu, Z.-W.; Qin, D. *J. Am. Chem. Soc.* **2014,** *136*, 8153−8156.

[18] Yang, M.; Gilroy, K. D.; Xia, Y. *Part. Part. Syst. Charact.* **2017,** DOI: 10.1002/ppsc.201600279.

[19] Miranda, É. G. A.; Tofanello, A.; Brito, A. M. M.; Lopes, D. M.; Albuquerque, L. J. C.; de Castro, C. E.; Costa, F. N.; Giacomelli, F. C.; Ferreira, F. F.; Araújo-Chaves, J. C.; Nantes, I. L. *Front. Chem.* **2016,** *4*, 13.

[20] Wang, X.; Zhang, Z.; Hartland, G. V. *J. Phys. Chem. B* **2005,** *109*, 20324−20330.

[21] Kim, T.; Canlier, A.; Cho, C.; Rozyyev, V.; Lee, J.-Y.; Han, S. M. *ACS Appl. Mater. Interfaces* **2014,** *6*, 13527−13534.

[22] Xia, X.; Xie, S.; Liu, M.; Peng, H.-C.; Lu, N.; Wang, J.; Kim, M. J.; Xia, Y. *Proc. Natl. Acad. Sci. U.S.A.* **2013,** *110*, 6669−6673.

[23] Zhang, Q.; Cobley, C. M.; Zeng, J.; Wen, L.-P.; Chen, J.; Xia, Y. *J. Phys. Chem. C* **2010,** *114*, 6396−6400.

[24] Xia, Y.; Kim, E.; Whitesides, G. M. *J. Electrochem. Soc.* **1996,** *143*, 1070−1079.

[25] Cobley, C. M.; Rycenga, M.; Zhou, F.; Li, Z.-Y.; Xia, Y. *J. Phys. Chem. C* **2009,** *113*, 16975−16982.

[26] He, D.; Jones, A. M.; Garg, S.; Pham, A. N.; Waite, T. D. *J. Phys. Chem. C* **2011,** *115*, 5461−5469.

[27] Yang, M.; Hood, Z. H.; Yang, X.; Chi, M.; Xia, Y. *Chem. Commun.* **2017,** *53*, 1965−1968.

CHAPTER 6

CONCLUSIONS AND FUTURE DIRECTIONS

6.1 Conclusions

This dissertation showcases some recent developments with regard to the syntheses of Au hollow nanostructures for photonic and biomedical applications, with a focus on Au nanocages and their derivatives. I started with the synthesis of Cu-doped Au nanocages to demonstrate that new functionalities could be introduced to these nanomaterials by means of metal coating. The strategy was based on the co-reduction of Au(III) and Cu(II) precursors in the presence of pre-synthesized Au nanocages. The resulting Au-Cu alloy nanocages are similar to the pristine Au nanocages, in terms of morphology and optical properties. When $^{64}Cu^{2+}$ was used in combination with cold $^{63}Cu^{2+}$, I could easily obtain radioactive nanocages. The Cu content in the resultant nanocages could be readily adjusted by varying the thickness of the Au-Cu shells and/or altering the feeding ratio of Au to Cu precursors during a synthesis. According to ICP-MS measurements, the Cu component could contribute up to 9% of the total atoms included in a nanocage. When used as a PET tracer for cancer imaging, these nanocages exhibited effective accumulations in both 4T1 and PDX tumor models due to the EPR effect. Autoradiography analysis of the tumors also indicated a homogeneous intra tumoral distribution for the nanocages in both models.

During the synthesis of Cu-doped Au nanocages, I found that the Au and Cu atoms were not only deposited on the outer surface of a nanocage, as expected, but also on the inner surface. To understand how the experimental parameters affect the deposition behavior during the overgrowth of nanocage-based seeds, I quantitatively studied two different Pd(II) precursors: $PdCl_4^{2-}$ and $PdBr_4^{2-}$. The two precursors have entirely different reduction kinetics, and distinctive reduction pathways will be involved when they are used for seed-mediated growth. When $PdCl_4^{2-}$ was used, its fast reduction rate would ensure a

solution reduction for the precursor ions upon their introduction into the reaction mixture. As a result, Pd atoms were only deposited on the outer surface of the Au nanocage. On the other hand, when $PdBr_4^{2-}$ was used as a precursor while keeping all other experimental conditions the same, Pd atoms were deposited on both inner and outer surfaces of a Au nanocage, due to the slow reduction of $PdBr_4^{2-}$. In this case, the precursor ions were not directly reduced by the reductant in solution. Instead, they first adsorbed onto the surface of a seed, followed by a catalytic reduction involving the seed. The slow reduction of these precursor ions wins additional time for their inward diffusion, leading to deposition on both inner and outer surfaces.

In addition to the development of multi-functional Au nanocages, I have also tried to improve the current synthesis of Au nanocages. Previous research suggested that a small particle size should contribute to an improved bio-distribution of the nanomaterials after their systemic administration. By leveraging 5-nm Au spherical seeds, I prepared 13-nm Ag nanocubes, and transferred them into sub-15 nm Au nanorattles. Due to the poor physical robustness of the small particles, their original structure could not be maintained during a conventional galvanic reaction with $HAuCl_4$. To save the structure, I first coated a thin layer of Au on the surface of the Ag nanocubes, followed by the formation of hollow structure through the introduction of $HAuCl_4$. The resulting compact nanorattles demonstrated similar physicochemical properties as the commonly-used nanocages with edge length of around 50 nm. In a proof-of-concept trail, they were shown to be effective in killing the cancer cells through the photothermal effect.

The method to deposited ultrathin Au shell onto Ag nanocubes could be readily extend to other Ag nanomaterials. In one example, I coated Ag nanowires with Au sheaths to improve their stability against reactions with oxidants or sulfides. The coating of Au does not change the morphology of the pristine nanowires. Importantly, the optical properties of the Ag@Au core-sheath nanowires were almost identical to those of the pristine Ag nanowires, ensuring the transparency required for producing flexible electrodes.

My research has greatly advanced understanding of the shape-controlled synthesis of Au nanocages and related nanostructures, thus representing a major step forward towards the rational design and synthesis of colloidal noble-metal nanomaterials.

6.2 Future Directions

The understanding achieved in my dissertation work about the synthesis and development of Au nanocages and related nanostructures sheds light on the rational design and controlled synthesis of noble-metal nanocrystals with desired structures, morphologies, and properties, enabling their full potential for applications in photonics and biomedical research. To advance towards a fine control over the synthesis of these nanostructures, further development and extension of the current studied is necessary.

One of the major remaining challenges in the application of Au nanocages for cancer theranostics lies in the insufficient clearance of these nanomaterials by human body after their application. The chemical inertness of Au makes it impossible for Au nanocages to be digested by enzymes in the body, creating a barrier for the effective elimination of Au-based nanomaterials from the body. In general, Au nanocages can be removed from the body through two pathways, renal clearance by liver and biliary clearance by hepatic cells. The biliary clearance is complicated in mechanism and not as effective as renal clearance. For nanomaterials to be effectively eliminated through renal clearance, their size should be smaller than 6 nm, which still cannot be reached at the moment [1,2]. Future effort needs to be directed towards further reduction of the particle size of Au nanocages, as well as the rational design and synthesis of such nanomaterials so that they can fall apart to small pieces upon certain stimulation (light, pH, and temperature, among others.) *in vivo*.

The loading of cargos into hollow nanomaterials requires an extensive study to unveil how the cargos are loaded and the relationship between pore size and loading. In particular, the loading capability of Au nanocages is hard to track, and we can only access such information through indirect ways, such as monitoring the cargos released from the

capsules to check whether the loading was successful [3,4]; measuring the concentration of residual cargos after their loading and calculating the loading content by subtracting this amount from its original concentration [5]; and estimating the total amount of payloads after the removal of Au-based carriers [6]. These indirect methods tend to be less controlled, in that they fail to give solid evidence to support the loading of cargos into Au nanocages. Moreover, differentiation between the payloads inside a nanocage and those merely attached to the surface through physical or chemical absorption is not possible using the aforementioned methods. As a result, there is an urgent need for the development of new characterization approaches, which can be applied to analyze the loading of cargos directly, preferably by means of visualization. It can help us answer the long-existing question, "whether or not cargos could be loaded inside nanocages *via* the small pores present on the surfaces through diffusion."

Another area that deserves further exploration is the impact of the openings on the loading capability of Au nanocages. Currently, the same experimental procedure is used to load Au nanocages (or other hollow nanostructures) with various types of cargos, regardless of their distinctive porous structures. To gain a better understanding of the loading performance of such hollow nanomaterials, it is worthwhile to study the relationship between the opening on Au nanocages and the size of the cargos to be loaded. Currently, the synthetic approach used to generate Au nanocages involves a complex galvanic replacement between Ag templates and Au precursor, and a precise control over the pore size is hard to realize. Recently, I found that a fine tuning of the pore size is possible by depositing a thin layer of Au onto the pre-synthesized Au nanocages [7]. With this capability, it will be possible to study the loading capability of Au nanocages with different pore sizes, in the presence of various cargo models, such as small molecules, proteins, and nanoscale particles. This research could serve to provide information on the optimal structure of nanocages for different cargos, which may greatly push the real-world applications of these nanomaterials.

6.3 References

[1] Sun, T.; Zhang, Y. S.; Pang, B.; Hyun, D. C.; Yang, M.; Xia, Y. *Angew. Chem., Int. Ed.* **2014,** *53*, 12320–12364.

[2] Yang, X.; Yang, M.; Pang, B.; Vara, M.; Xia, Y. *Chem. Rev.* **2015,** *115*, 10410–10488.

[3] Yavuz, M. S.; Cheng, Y.; Chen, J.; Cobley, C. M.; Zhang, Q.; Recenga, M.; Xie, J.; Kim, C.; Song, K. H.; Schwartz, A. G.; Wang, L. V.; Xia, Y. *Nat. Mater.* **2009,** *8*, 935–939.

[4] Moon, G. D.; Choi, S.-W.; Cai, X.; Li, W.; Cho, E. C.; Jeong, U.; Wang, L. V.; Xia, Y. *J. Am. Chem. Soc.* **2011,** *133*, 4762–4765.

[5] Li, S.; Zhang, L.; Wang, T.; Li, L.; Wang, C.; Su, Z. *Chem. Commun.* **2015,** *51*, 14338–14341.

[6] Xia, X.; Yang, M.; Wang, Y.; Zheng, Y.; Li, Q.; Chen, J.; Xia, Y. *ACS Nano.* **2012,** *6*, 512–522.

[7] Yang, M.; Huo, D.; Gilroy, K. D.; Sun, X.; Sultan, D.; Luehmann, H.; Detering, L.; Li, S.; Qin, D.; Liu, Y.; Xia, Y. *ChemNanoMat* **2017,** *3*, 44–50.